

Copyright
by
Rambod Yousefzadeh Tabasi
2022

The Dissertation Committee for Rambod Yousefzadeh Tabasi
certifies that this is the approved version of the following dissertation:

Non-local Methods in Transport Phenomena

Committee:

John T. Foster, Supervisor

Chad M. Landis

Krishnaswamy Ravi-Chandar

Andre M. Hesse

Clinton N. Dawson

Non-local Methods in Transport Phenomena

by

Rambod Yousefzadeh Tabasi, B.S., M.S.

DISSERTATION

Presented to the Faculty of the Graduate School of
The University of Texas at Austin
in Partial Fulfillment
of the Requirements
for the Degree of

DOCTOR OF PHILOSOPHY

THE UNIVERSITY OF TEXAS AT AUSTIN

May 2022

To my mother, Manijeh, thank you for bringing joy and positivity to our family.

To my father, Esmaeil, thank you for teaching me the value of hard work and dedication.

To Helia, my soulmate and the love of my life. Thank you for your endless love, support and encouragement.

Acknowledgments

I would like to thank my wife Helia for her love and support. Her personal and professional growth inspires me to push myself harder. I could not have asked for a better partner to go through life with.

I would also like to thank my parents and my brothers Reza and Ramin for their continuous support throughout my life. They have always pushed me to grow and pursue my goals. I Thank Reza for paving the way and Ramin for being an amazing role model.

I feel lucky and honored for having great friends and family members in my life who offered me care and support throughout my PhD. The list would be too long to fit here. However, I would like to specifically thank Zahra Ziari, Bobak Saadat, Pedram Khosravian, Sheida Zarrinfam, Mitra Vasei and Meeko Tabasi. I hope I can be as good a friend for them as they have been for me.

I would also like to greatly thank Dr. Scott Evans, Nina Ho and Mitch Jacobson. Their support and mentorship allowed me to pursue my goals in the entrepreneurship world and learn skills that I would not have had the opportunity to learn otherwise.

I would like to thank my dissertation committee: Dr. Chad Landis, Dr. Krishnaswamy Ravi-Chandar, Dr. Marc Hesse and Dr. Clinton Dawson. Whether their help came through an elegantly taught course or from

conversations, their willingness to assist my growth is sincerely appreciated.

Finally, I would like to express my gratitude to Dr. John Foster for being an amazing advisor, mentor and friend. His insight and hard work have been a constant motivator.

Non-local Methods in Transport Phenomena

Publication No. _____

Rambod Yousefzadeh Tabasi, Ph.D.
The University of Texas at Austin, 2022

Supervisor: John T. Foster

Peridynamics is a well-established nonlocal method for modeling the deformation of solid bodies. The concepts introduced by the peridynamic (PD) theory have demonstrated special utility for problems in solid mechanics which include the evolution of spatial discontinuities, i.e. cracks. While the PD theory has been extensively studied on problems of solid mechanics, its capabilities as a multi-scale modeling theory also make it a candidate for modeling problems of heat and mass transport in fluids. Fluid mechanics has so far been an under-explored area of peridynamic research.

The aim of this dissertation is to lay the foundation for the use of peridynamics in fluid mechanics by presenting viable techniques for modeling heat and mass transport problems using peridynamic-based nonlocal models. This investigation starts with a nonlocal advection-diffusion model for immiscible two-phase flow in porous media. The proposed nonlocal formulation is shown

to be capable of naturally handling the sharp and irregular changes in the concentration at the interphase of the fluids. As a result, the proposed model can capture the formation and evolution of instabilities at the fluid interface.

An important feature of peridynamics models is an *influence function* which governs the strength of nonlocality and can be used as a tool for multiscale modeling. The local limit of a peridynamics model is independent of the choice of the peridynamic influence function; however, the correct non-local mechanics cannot be modeled unless a physically meaningful influence function is used. This dissertation presents a systematic approach for the calculation of a nonlocal kernel that has been homogenized from molecular dynamics (MD) calculations of heat transfer in nanofluids. The MD calculations fully resolve the individual constituents of the nanofluid. The peridynamic continuum model is then shown to be accurate in demonstrating the enhanced heat transfer properties of nanofluids on domains larger than what can be practically solved using MD.

Finally, a nonlocal extension of the Navier-Stokes equations is developed along with a penalty formulation for their numerical solution. Mathematical convergence is shown to recover the classical Navier-Stokes partial differential equations as limiting case. Computational simulation results are then presented for several test cases demonstrating that the formulation is stable and can recover important features of the classical theory for several test cases.

Table of Contents

Acknowledgments	v
Abstract	vii
List of Figures	xii
Chapter 1. Introduction	1
1.1 Motivation	1
1.2 Outline of The Dissertation	9
Chapter 2. Literature Review	11
2.1 peridynamic	12
2.1.1 Bond-based peridynamic	15
2.1.2 State-based peridynamic	17
2.2 The Mesh-free Methods	18
2.3 The Influence Function	20
2.4 Multi-scale Problems	21
2.5 Heat & Mass Transport Problems	23
Chapter 3. A nonlocal advection-diffusion model for two-phase miscible flow in porous media	28
3.1 Introduction	28
3.2 Nonlocal Model	33
3.2.1 Nonlocal Gradient	35
3.2.2 Nonlocal Laplacian	37
3.2.3 Influence Function	39
3.2.3.1 Constant	39
3.2.3.2 Linear	40
3.3 Discretization	40

3.4	Results and Discussion	43
3.4.0.1	Parametrization	44
3.4.0.2	Boundary Conditions	44
3.4.1	Case 1: Finite Differencing Scheme	45
3.4.1.1	Parametrization	45
3.4.1.2	Boundary Conditions	46
3.4.2	Case 1: Convergence Study	46
3.4.3	Case 2: Disturbed Interface	47
3.4.3.1	Parametrization	47
3.4.3.2	Boundary Conditions	50
3.4.3.3	Nonlocal Simulation Results	50
3.4.4	Dispersion vs. Mixing Degree	53
3.5	Conclusion	56

Chapter 4. Nonlocal Formulation for Heat Transfer in Nanofluids **57**

4.1	Introduction	57
4.2	Nonlocal Diffusion Model	62
4.3	Proposed Method for Kernel Extraction	65
4.4	Discretization	73
4.5	Results and Discussion	73
4.5.1	Steady-State Heat Transfer	76
4.5.1.1	Parameterization	76
4.5.1.2	Boundary Conditions	76
4.5.1.3	Choice of the Nonlocal Kernel	77
4.5.1.4	Nonlocal Simulation Results	78
4.5.2	Transient Heat transfer	78
4.5.2.1	Parameterization	79
4.5.2.2	Boundary conditions	80
4.5.2.3	Choice of the Nonlocal Kernel	80
4.5.2.4	Nonlocal Simulation Results	80
4.6	Conclusion	83

Chapter 5. A Multi-scale Nonlocal Approach for Turbulence Modeling	84
5.1 Introduction	84
5.2 Nonlocal Model	88
5.3 Discretization	95
5.4 Results and Discussion	96
5.4.1 Case 1: Flow with Restriction	97
5.4.1.1 Parametrization	97
5.4.1.2 Boundary Conditions	98
5.4.1.3 Convergence Study	98
5.4.1.4 Simulation Results	98
5.4.2 Case 2: Laminar Flow Between Two Infinitely Large Plates	99
5.4.2.1 Parametrization	100
5.4.2.2 Boundary Conditions	101
5.4.2.3 Convergence Study	101
5.4.2.4 Simulation Results	101
5.4.3 Case 3: Flow Over a Cylinder	102
5.4.3.1 Parametrization	104
5.4.3.2 Boundary Conditions	104
5.4.3.3 Convergence Study	105
5.4.3.4 Simulation Results	106
5.4.3.5 Parametrization	107
5.4.3.6 Simulation Results	109
5.5 Conclusion	109
Chapter 6. Summary	112
Bibliography	115

List of Figures

2.1	Point \mathbf{x} and its horizon shown in white. $\boldsymbol{\xi}$ is a vector connecting \mathbf{x} to other points in its neighborhood and ϵ is the radius of the horizon.	16
2.2	Fragmentation of a brittle target due to an impact with a rigid sphere [88]	19
2.3	Horizon of each point in the domain is split into up-wind and down-wind halves based on the local flow velocity [99]	25
2.4	Long range channels in a porous media can serve as direct connection between point \mathbf{x} and its nonlocal neighbor \mathbf{x}' [45]	26
3.1	Point \mathbf{x} and its horizon shown in white. $\boldsymbol{\xi}$ is a vector connecting \mathbf{x} to another point in the neighborhood and ϵ is the radius of the horizon.	34
3.2	Up-winding applied to the neighborhood of point \mathbf{x} . Here \mathcal{H}_ϵ is the horizon and \mathbf{v} shows the local wind direction	43
3.3	Illustration of how horizon of a point can be split at the edges of the domain	44
3.4	Convergence of concentration solution of the nonlocal model to the finite differencing solution drawn in black	48
3.5	Convergence of pressure solution of the nonlocal model to the finite differencing solution drawn in black	49
3.6	Above screen shots follow the evolution of fingers from the injection moment for 8 ms for a two phase flow with an initially disturbed interface.	51
3.7	Central injection was done under pressure difference $\Delta p = 1500$ Pa, $R = 3.0$, $\Delta t = 0.00625$ ms. Screen shots are taken at 3 ms intervals.	52
3.8	Comparison of the experimental results and the prediction of the proposed nonlocal model. Plots are showing the effect of increasing the viscosity ratios on the shape of and size of the fingers	54
3.9	Illustration of the mixing degree based on the calculation of the variance of the concentration field	55

4.1	Point \mathbf{x} and its horizon shown in white. $\boldsymbol{\xi}$ is the vector connecting \mathbf{x} to any other point in the horizon and ϵ is the radius of the horizon.	63
4.2	Domain was split into spherical shells to calculate the average forces experienced from each discretized ring. Here, larger blue dots represent the nanoparticles and small black dots are argon atoms.	67
4.3	As the number of slices is increased, the calculated LJ potential for pure argon is converging to the analytical LJ potential shown by the dashed line	68
4.4	The plots show the radial distribution of atoms about a central particle in both pure argon and 3.8% Cu-Ar nanofluid. Blue dashed lines represent the equilibrium distance for liquid argon. As expected, the introduction of nanoparticles has forced the argon atoms to rearrange into a new structure with larger spacings between atoms	69
4.5	Computationally up-scaled kernels for pure liquid argon and 3.8 % Cu-Ar nanofluid	71
4.6	Components of LJ potential from interactions between Cu and Ar particles	72
4.7	Comparison of thermal conductivity calculations between MD, NL and HC models. The results of the predictions from the proposed nonlocal model and the MD model are in close agreement. The continuum HC model under-predicts the thermal conductivity for all nanofluids	75
4.8	Illustration of how horizon of a point can be split at the edges of the domain	77
4.9	Results of simulations for a steady state problem using constant heat flux boundary conditions. Here, it is shown that the results of local and nonlocal models closely match. It is also shown that the choice of nonlocal kernel does not affect the result of the steady state problems	79
4.10	Results of the local and nonlocal transient simulations on a domain with constant temperature boundary conditions. The results are shown to converge for the case where $\epsilon \ll \Delta L$	81
4.11	Results of simulations for a transient problem. Here the size of the characteristic length scale, ϵ , is chosen to be close to the domain's length L . For this case, the choice of nonlocal kernel is shown to have a significant effect on the calculated temperature profile.	82

5.1	The convergence study done on the penalty parameter indicates that a λ larger than 100 would sufficiently enforce incompressibility.	99
5.2	A reduction of available cross-sectional area has resulted in an increase in the mean flow velocity over the rectangular restriction. The nonlocal model is also shown to have captured more complex features of this flow such as the formation of a vortex at the trailing edge of the rectangular object	100
5.3	As the number of nodes are increased, the profile calculated by the nonlocal model is shown to converge to the analytical solution. The anti-symmetry of the lines are due to the automatic placement of the nodes for the cases where the domain height is not divisible by the number of nodes. The anti-symmetry fades away as the number of nodes is increased	102
5.4	Formation and development of the boundary layer for flow between two parallel plates as simulated by the nonlocal model .	103
5.5	Illustration of the velocity variation along a vertical line passing through the center of the cylindrical object shows the convergence of the results of the proposed nonlocal model to the local solution calculated by ANSYS Fluent and local limit of the PDDO simulation presented by Nguyen et al. [60]	105
5.6	Illustration of the velocity variation along a horizontal line passing through the center of the cylindrical object shows the convergence of the results of the proposed nonlocal model to the local solution calculated by ANSYS Fluent and local limit of the PDDO simulation presented by Nguyen et al. [60]	106
5.7	Variation of x-component of velocity, u (m/s) as simulation by the proposed nonlocal model	108
5.8	Variation of y-component of velocity, v (m/s) as simulation by the proposed nonlocal model	108
5.9	As the Re is increased, the combination of counter-rotating vortices behind the cylindrical object result in the formation of the nonlinear oscillations known as the von Karman street	109
5.10	Variation of velocity magnitude on a vertical and a horizontal line passing through the center of the cylinder	110
5.11	Variation of the y component of the velocity clearly showing the separation of the counter-rotating vortices	110

Chapter 1

Introduction

1.1 Motivation

Over the past 20 years, *peridynamic* (PD) theory has become a well-established nonlocal method for simulating the deformation of solid bodies. The concepts introduced by the peridynamic theory have proven to be especially helpful for problems in solid mechanics, which include spatial discontinuities, e.g. cracks. The theory was originally developed by Silling [86] as a reformulation of the classical theory of solid mechanics. The main goal of this theory was to remove the dependence on the spatial derivatives of displacements. Silling achieved this goal by introducing pairwise forces that connect two material points over a finite distance. These interactions over finite distances make the peridynamic theory nonlocal by nature.

In addition to tackling problems in solid mechanics with spatial discontinuities, peridynamic theory is also proven to be a strong tool for multi-scale modeling [4, 101, 113]. Silling [87] demonstrated that in solid materials, nonlocality can be a direct result of the small-scale heterogeneities of the domain. These heterogeneities are often excluded through the implicit or explicit homogenization of the problem. Therefore, a physically meaningful peridynamic

model for a solid material *must* contain information about the microstructure of the material. This information in a peridynamic-based model is typically captured by the influence function, ω . Delgosaie et al. [24] explained the presence of anomalous diffusion in porous media by using the multi-scale connectivity of the natural pore networks. The authors presented a systematic method to use the pore network mesoscale computational models to extract the required peridynamic influence function. D’Elia et al. [27] focused on finding the diffusivity parameter for peridynamic and fractional models by using an optimal control technique. More recently, Xu et al. [112, 113] introduced a data-driven regression algorithm for the calculation of the influence function of a bond-based peridynamic model to describe the macro-scale deformation of linear elastic medium with periodic heterogeneity.

While the PD theory has been extensively studied using problems of solid mechanics, its capabilities as a multi-scale modeling tool also make it an ideal candidate for modeling problems of heat and mass transport in fluid mechanics. Fluid mechanics has so far been an under-explored area of peridynamic theory. The goal of this dissertation is to lay the foundation for the use of peridynamic theory in fluid mechanics by presenting viable continuum models and numerical techniques for modeling heat and mass transport problems using peridynamic-based nonlocal models.

Classical models of heat and mass transport use governing laws in which fluid flux is linearly related to a potential (e.g., Fick’s and Darcy’s laws). These models can be derived by statistical analysis that assumes the Brownian mo-

tion of diffusing particles. In such situations, the Markovian nature of the underlying statistics is the core assumption of the diffusion process. Nonetheless, this assumption is often not valid for heterogeneous domains where analysis of diffusing tracer particles leads to non-Gaussian distributions. These processes are termed *anomalous diffusion* and include sub- and super-diffusion as particular cases [57]. Examples of anomalous diffusion are seen in polymers [35,62], biomaterials [6] and in petroleum engineering in the studies of flow through porous media [39,82] and the formation of viscous fingers [19,42].

Viscous fingering is an interface instability that can occur between two or more phases in miscible multiphase fluid flow. It is characterized by a highly irregularly shaped interface, often with long “fingers” from the displacing phase propagating far into the phase(s) being displaced. Although many secondary effects may be involved, most researchers consider the principal controlling mechanism to be the viscosity ratio between phases. Spatial changes in pressure are lower in the phase with lower viscosity leading to higher pressure in the leading edge of the fingers. This higher pressure causes a force imbalance that assists in propagating the interface forward into the more viscous phase.

The most used experimental methods for modeling viscous fingering, employes Hele-Shaw cells to mimic two-dimensional creeping fluid flow in a porous media. The use of the Hele-Shaw cells offers a convenient way for the visual study of the viscous fingers. Since the introduction of this method by Saffman and Taylor [75], many have attempted to improve the setup to

model viscous fingering more accurately. But despite the improvements, the experimental work has not yet provided an accurate method for the characterization of the viscous fingering phenomena. Dispersion cannot be elucidated in Hele-Shaw cell experiments due to the underlying homogeneous medium; nevertheless, it can be significant in applications of miscible displacements such as secondary and tertiary oil recovery in the field of petroleum engineering [49].

More recently, numerical simulations using finite difference and finite element approaches have been used to model initiation and propagation of fingers [77,91]. While these numerical simulations can be tools for exploring many factors involved in viscous fingering, the underlying physical equations that they discretize are void of any dispersive effects [3,45] (i.e. any observed dispersion is numerical). Occasionally, the underlying partial-differential equations used to model subsurface fluid flow are parameterized with time-dependent diffusion coefficients to account for dispersion; however, the physical justification for this assumption is not well-established in many cases (i.e. when modeling Newtonian fluids). Dispersion is a spatial phenomenon in the subsurface caused by heterogeneities at length scales smaller than what are typically resolved in a fluid transport simulation.

Another common example of a problem where small-scale perturbations can result in macro-scale features in a flow is seen in the study of turbulence. Turbulence is widely known as one of the oldest unsolved problems in physics. It is characterized by the chaotic behavior of the fluid pressure and velocity fields at high Reynolds numbers. Although the effects of turbulence are ex-

perienced through the macroscopic features of a flow, its source lies in the interactions of the fluid particles at the micro-scale. Small perturbations in the flow, which are typically formed within a boundary layer or introduced at inlets, can be retarded by viscous forces. However, if the momentum effects are large enough, a laminar flow will quickly transition to an unsteady and disorganized turbulent flow. Examples of turbulent flows include blood flow inside arteries and flow through mechanisms such as pumps, turbines, and around aircraft wings.

Traditionally, automotive and aerospace industries have used experimental methods such as wind tunnels and scaled prototypes to visually study the behavior of flow as it passes over an object of interest. However, wind tunnels that are large enough to fit full-scale prototypes are rare and hard to maintain. Additionally, reproducing the exact conditions of real-world interest inside a tunnel is often hard to achieve. Given the challenges involved with experimental studies using wind tunnels, the computational methods for modeling turbulent flows have gained more popularity in the past few decades. Computational methods based on the classical continuum approach such as direct numerical simulation (DNS) can be used to accurately calculate shear stresses and pressure fields in all parts of the flow. These fields can then be used to calculate forces and momentum as well but only if a fine enough spatial and temporal discretization can be employed. An appropriate spatial discretization must be fine enough to capture the dissipative and viscous effects that occur at microscopic levels while covering a domain size, which is typically

many orders of magnitudes larger. This means that even with the widespread availability of high-performance computers, the computational time required is still the bottleneck of DNS modeling. Alternative computational methods, such as Reynold’s Averaged Navier-Stokes (RANS) modeling and Large Eddy Simulations (LES), offer their own advantages. As useful as LES is, it still requires significant computational power and lacks the ability to model small scale phenomena.

One of the main challenges with the study of turbulence is that the underlying assumptions of continuum mechanics break down at scales approaching the mean free path of particles. Typically, spatially nonlocal physics are analyzed with a fractional derivative approach [57] or with the use of integral equations [82]. The latter is more general and hence, is the method chosen for the current investigation. An example of an integral-type nonlocal model called peridynamic theory was introduced by Silling [86] to model elasticity and material failure in solid mechanics. Silling’s initial work was focused on the derivation of a set of integro-differential equations for conservation of momentum in solid structures. This work became the foundation of a theory that has turned into a promising modeling tool. While multiple studies have investigated the mathematical soundness of the peridynamic approach in fluid mechanics, little work has been done to study the effectiveness of this approach when it comes to modeling complex flow geometries including turbulence.

The use of integrals in the place of derivatives makes nonlocal models more effective in modeling spatial discontinuities. However, this enhancement

comes at a significant cost of much longer computational time. To remedy this, most nonlocal models are solved in parallel using a supercomputer. Another challenge involved with peridynamic-based nonlocal models is related to the extraction of the nonlocal kernel. The nonlocal kernel is a weight function that defines the strength of the bonds between different grid points in a nonlocal simulation. The selection of this nonlocal kernel has historically been made to reduce the inaccuracies of the integration process [79]. However, as this work will discuss in depth, a proper choice *must* also take into consideration the physics of the problem [80], either through numerical upscaling procedures [109, 114] or by theoretical homogenization of micro-structural heterogeneity [113].

Seleson and colleagues [81] argued that peridynamic and in general nonlocal models have similar computational structures to molecular dynamics (MD) models and showed the extent to which MD results can be recovered when NL models are used to perform the upscaling procedure. As a result, using MD can be thought of as a natural way to extract the nonlocal kernel of a domain.

As an example, in the numerical studies of nanofluids, the small scale of the problem makes it possible to use molecular dynamics to study the domain. For this specific problem, the continuum-based models fail to accurately simulate the nanofluid suspensions. The continuum formulations simply ignore the

changes to the atomic structure of the suspension when nano-sized ¹ particles are added to the base fluid. Classical models also consider the suspensions to be static, composite structures, an assumption which many believe adds to the inaccuracy of the calculations done using continuum models [76].

Recent work has shown that MD approaches can offer an accurate and easily reproducible method for the study of nanofluids [50, 52]. These models typically calculate the thermal conductivity using the Green-Kubo method. Apart from being able to investigate particle size and volumetric fraction, MD models have the capability to explore more complex aspects of a suspension, which includes the fluid layering [50, 52, 97] and the changes in the movement of base fluid after the introduction of particles [76]. Despite their strength, it's important to note that MD models are extremely computationally expensive. As a result, they are typically only run on domains that include a small number of particles.

The small domains used in the MD models are certainly not appropriate for modeling engineering problems. The MD models can, however, be used to study the strength of the interactions between the particles in the domain. Careful characterization of these interactions can then be used to extract an appropriate kernel to be used in a nonlocal model to run the analysis on much larger domains.

¹Average particle diameter of $10e - 9$

1.2 Outline of The Dissertation

In the following chapters, the capabilities of peridynamic-based models in modeling mass and heat transport problems will be explored. This investigation will start with a nonlocal advection diffusion model for two-phase flow in porous media. The proposed nonlocal formulation is naturally capable of handling the sharp changes in the concentration at the interphase of the fluids. As a result, the proposed model can capture the formation and development of instabilities at the fluid interface. As time passes, these instabilities are shown to develop into long fingers of the less viscous fluid also known as viscous fingers.

Chapter 4 focuses on the transfer of heat in nanofluids. This is a scenario in which macro-scale changes in the conductivity of the fluid can only be understood through the accurate modeling of the interactions at the atomic layer. In this chapter, an MD model is used to introduce a systematic approach for the calculation of the nonlocal kernel also referred to as the influence function. This influence function is then used to estimate the thermal conductivity of a wide range of Ar-Cu nanofluids with different copper loadings.

Finally, Chapter 5 builds on the other chapters of this project and presents a nonlocal model as an alternative to the penalty formulation of the Navier-Stokes equations for a two-dimensional incompressible flow. In this chapter, the nonlocal model is used to model more complex flow problems such as the von Karman Street problem. This chapter demonstrates the capabilities

of the proposed nonlocal model for modeling multi-scale phenomena such as vortex shedding.

Chapter 2

Literature Review

This chapter offers an overall review of the literature written on *peridynamic* theory. The following sections cover the relevant developments of the peridynamic theory in the field of fluid mechanics. Each subsequent chapter of this dissertation focuses on a specific problem in fluid dynamics and heat transfer. The chapters each propose a peridynamic-based solution as an alternative nonlocal modeling technique to counter the shortcomings of the available local models.

Each chapter also includes a literature review section. These sections offer a more in depth look at the specific problem they are examining and review the more relevant literature from the field of peridynamics. For example, chapter 3 studies the problem of two-phase miscible flow in porous media. This chapter covers the peridynamic-based models of advection-diffusion and the advancements of the peridynamic field in mathematical and numerical aspects with regard to advection-diffusion modeling.

2.1 peridynamic

Continuum mechanics (CM) was first developed by Cauchy in the 19th century as a branch of mechanics that analyzes objects and systems as continuous media rather than discrete particles. From the perspective of continuum mechanics, particles are only allowed to interact at zero distances, deformations are twice differentiable and the conservation laws of mechanics apply.

In the past few decades, CM based numerical methods such as the finite element method (FEM) have contributed to significant advancements in modeling engineering and scientific problems. However, CM based methods including FEM suffer from mesh dependency related difficulties. Mesh-dependency of FEM limits the use of this method in problems with large deformations such as ductile failure and problems that include spatial discontinuities such as cracks. Linear elastic fracture mechanics (LEFM) introduced the concepts of stress intensity factor and kinetic relations to attempt to model the progression of crack tips. However, as the name suggests, LEFM use is limited to the linear and elastic deformations. In quasi-brittle materials, large, inelastic deformations experienced at the crack tip break the underlying assumptions of LEFM.

For such problems, one of the most robust continuum-based methods available is the cohesive zone model (CZM) [8]. The cohesive zone refers to the zone of micro-cracks surrounding the crack tip. Here, the crack path is determined by the interconnection of the micro-cracks. This method offers a

solution to capture the organic growth of the crack tip. Nonetheless, CZM still suffers from mesh-dependency issues as it only allows for the formation and growth of the crack in the pre-defined zone with cohesive elements [102].

Another typical approach for tackling domains with discontinuities is the extended finite element method (XFEM) approach [58]. In the original implementation of the XFEM, standard polynomial basis functions for the nodes that are in contact with a crack are coupled with discontinuous basis functions to provide a method for solution dependent crack growth [23, 95]. However, the XFEM approach requires external input to govern the orientation of the crack tip propagation and as a result adds more complexity to the system.

Another shortcoming of CM is experienced when studying domains where the domain size is comparable to the characteristic length scale of the problem. For such problems, Molecular Dynamics (MD) might be used as the appropriate tool for the analysis. In the MD view, discretized particles are allowed to interact via long range Van der Waals forces. However, the use of the MD approach is currently restricted to the domains that include a small number of particles. The long simulation times and massive computational powers that are needed limit the ability to use MD models for the analysis of engineering problems at larger scales.

Peridynamic (PD) was originally introduced by Silling [86] as a way

to develop a theory that unifies the mechanics involved in continuous media, discrete particles, and media with evolving discontinuities. Silling arrived at a theory that is nonlocal by nature by avoiding the assumption that internal forces are contact forces and allowing the material particles to interact at finite distances. This goal is mathematically achieved using integro-differential operators instead of the differential operators used in classical formulations. In the classical continuum theory, the conservation of linear momentum is given as:

$$\rho_0 \ddot{\mathbf{u}}(\mathbf{X}, t) = \nabla \cdot \mathbf{P}(\mathbf{X}, t) + \rho_0 \mathbf{b}(\mathbf{X}, t), \quad \forall \mathbf{X} \in \mathcal{R}, \quad t \geq 0$$

Here, \mathbf{X} is the position vector of each material point in a material region \mathcal{R} . ρ_0 is the density field, \mathbf{u} is the displacement field, \mathbf{b} is the external body force density field and t stands for time. This local formulation of the linear momentum conservation is built based on the divergence of stress. The presence of spatial derivatives makes local formulations based on the local momentum formulation unable to deal with spatial discontinuities in the displacement field.

Alternatively, the formulation of the conservation of the linear momentum used by the peridynamic theory takes the following integro-differential form:

$$\rho_0 \ddot{\mathbf{u}}(\mathbf{X}, t) = \int_{\mathcal{H}(\mathbf{X})} \mathbf{f}(\mathbf{X} + \boldsymbol{\xi}, \mathbf{X}, t) d\xi + \rho_0 \mathbf{b}(\mathbf{X}, t), \quad \forall \mathbf{X} \in \mathcal{R}, \quad t \geq 0$$

Here, the function $\mathbf{f}(\mathbf{X} + \boldsymbol{\xi}, \mathbf{X}, t)$ is the pairwise force density function and \mathcal{H} is the neighborhood or *horizon* of \mathbf{X} . Any material point inside \mathcal{H} is allowed

to directly interact with the point \mathbf{X} . ϵ refers to the radius of this horizon which is conceptually equivalent to the cut off radius used in the MD models. In this formulation the term “bond” is used to refer to the pairwise interaction between a material point \mathbf{X} and any of its neighbors \mathbf{X}' . In this formulation, ξ is the peridynamic bond defined in the reference state. The peridynamic formulation is typically solved in its discretized format. This formulation can be written as:

$$\rho_0 \ddot{\mathbf{u}}(\mathbf{X}_i, t^n) = \sum_{\mathbf{X}_j \in \mathcal{H}_i} \mathbf{f}(\mathbf{X}_j, \mathbf{X}_i, t^n) \Delta V_j + \rho_0 \mathbf{b}(\mathbf{X}_i, t^n), \quad \forall \mathbf{X}_i \in \tilde{\mathcal{R}}, \quad t^n \geq 0$$

where $\tilde{\mathcal{R}}$ is the discretized body, n is the time step, and letter i and j refer to points \mathbf{X}_i and its neighbors \mathbf{X}_j . Here, ΔV_j stands for the volume of the horizon. The pairwise force density vectors between material points as defined in the peridynamic formulation need not be equal in magnitude. Nonetheless, if the force density vectors exerted by material points on each other are equal in magnitude and parallel to the relative position vector in the deformed state, then the peridynamic formulation is referred to as the bond-based formulation.

2.1.1 Bond-based peridynamic

The earliest and the simplest form of peridynamics, the bond-based peridynamic, was introduced in the original work of Silling [86]. In this formulation, the force density function that the two material points exert on each other are assumed to be equal in magnitude and parallel to the position vector

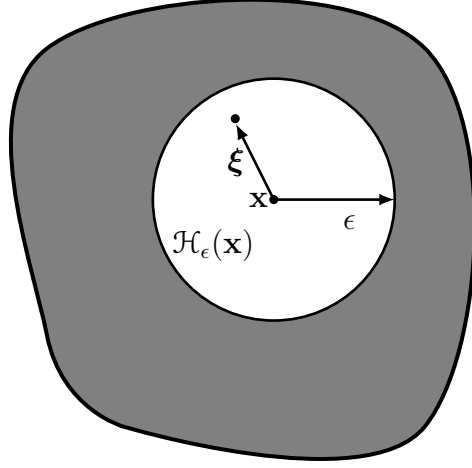


Figure 2.1: Point \mathbf{x} and its horizon shown in white. $\boldsymbol{\xi}$ is a vector connecting \mathbf{x} to other points in its neighborhood and ϵ is the radius of the horizon.

in the deformed state. Before providing the mathematical representation of the aforementioned property of the bond-based peridynamic formulation, let us introduce

$$\boldsymbol{\eta} = \mathbf{u}[\mathbf{X}', t] - \mathbf{u}[\mathbf{X}, t]$$

and as before

$$\boldsymbol{\xi} = \mathbf{X}' - \mathbf{X} \quad \forall \mathbf{X} \in \mathcal{R}.$$

As stated above, the force density function, \mathbf{f} must satisfy

$$\mathbf{f}(-\boldsymbol{\eta}, -\boldsymbol{\xi}) = -\mathbf{f}(\boldsymbol{\eta}, \boldsymbol{\xi}) \quad \forall \boldsymbol{\xi} \in \mathcal{H}_{\mathbf{x}}, \quad t \geq 0.$$

and, for conservation of momentum to hold

$$(\boldsymbol{\eta} + \boldsymbol{\xi}) \times \mathbf{f}(\boldsymbol{\eta}, \boldsymbol{\xi}) = 0 \quad \forall \boldsymbol{\xi} \in \mathcal{H}_{\mathbf{x}} \quad t \geq 0.$$

Here, \mathbf{f} contains all the constitutive properties of the material and its independence from all other local conditions limits the ability of this formulation to freely define a Poisson's ratio. In fact, the bond-based peridynamic formulation automatically specifies this value as 0.33 for the two-dimensional case and 0.25 for the three-dimensional problems.

2.1.2 State-based peridynamic

The state-based peridynamic theory was introduced by Silling in 2007 to address the aforementioned issues of the bond-based peridynamic formulation, which is its inability to define an arbitrary Poisson's ratio. In the state-based formulation, the force density vector is defined as:

$$\mathbf{f}(\mathbf{X}', \mathbf{X}, t) = \underline{\mathbf{T}}(\mathbf{X}, t)\langle \boldsymbol{\xi} \rangle - \underline{\mathbf{T}}(\mathbf{X}', t)\langle -\boldsymbol{\xi} \rangle, \forall \mathbf{X} \in \mathcal{R}, \boldsymbol{\xi} \in \mathcal{H}(\mathbf{X}) \quad t \geq 0.$$

Here, $\underline{\mathbf{T}}$ is called the *force vector state* that operates on $\boldsymbol{\xi}$ and maps the deformation vector state into a force vector state for all the points in horizon, $\mathcal{H}(\mathbf{X})$. This is conceptually similar to the operation of second order tensors in the sense that both operators map a vector into another vector. Using the definition of the peridynamic force vector state, the state-based peridynamic linear momentum equation can be written as

$$\rho_0 \ddot{\mathbf{u}}(\mathbf{X}, t) = \int_{\mathcal{H}(\mathbf{X})} [\underline{\mathbf{T}}(\mathbf{X}, t)\langle \boldsymbol{\xi} \rangle - \underline{\mathbf{T}}(\mathbf{X}', t)\langle \boldsymbol{\xi} \rangle] d\boldsymbol{\xi} + \rho_0 \mathbf{b}(\mathbf{X}, t) \forall \mathbf{X} \in \mathcal{R}, \quad t \geq 0.$$

In this equation, regardless of the chosen $\underline{\mathbf{T}}$, the linear admissibility condition is automatically satisfied although, the balance of angular momentum is no

longer fulfilled a priori. In this case, it is explicitly required that

$$\int_{\mathcal{H}_{\mathbf{x}}} \underline{\mathbf{y}}(\mathbf{X}, t) \langle \boldsymbol{\xi} \rangle \times \underline{\mathbf{T}}(\mathbf{X}, t) \langle \langle \boldsymbol{\xi} \rangle \rangle d\boldsymbol{\xi} = 0, \forall \mathbf{X} \in \mathcal{R}, t \geq 0. \quad (2.1)$$

Here, $\underline{\mathbf{y}}$ is the deformation vector state that maps a bond to its deformed shape. Equation (2.1) can be used to further split peridynamic materials into two subcategories. If for a peridynamic material the force state is parallel to the deformed bond, then this equality is automatically satisfied, and the material is known as the ordinary state-based material. Otherwise, the formulation is referred to as non-ordinary state-based peridynamics.

2.2 The Mesh-free Methods

The typical mesh-based approaches used in techniques such as FEM cannot be used with 3 dimensional domains with complex geometries. A distorted mesh can result in unacceptably large numerical errors. The mesh based approaches also fail to accurately model domains with discontinuities and transient fluid flow in porous media [63]. Silling et al. [88] introduced the mesh-free discretization for the strong form of the peridynamic equations. Their proposed method divides the domain into nodes from a grid each with a known volume in the reference configuration. This method is referred to as mesh-free as it does not use elements to connect the nodes. The authors demonstrated the capabilities of their proposed mesh-free method by modeling the interaction and propagation of cracks during an impact between a rigid sphere and a brittle target. Figure 2.2 shows the result of this simulation.

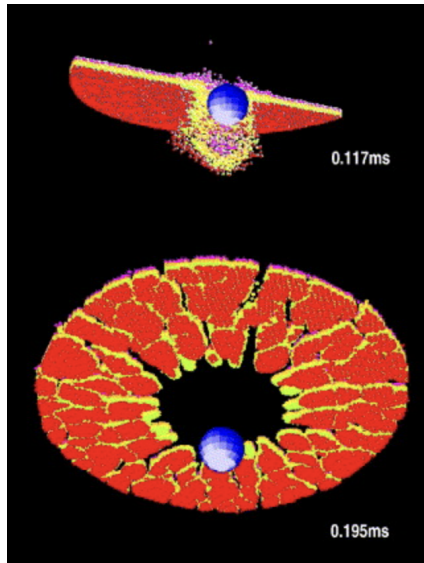


Figure 2.2: Fragmentation of a brittle target due to an impact with a rigid sphere [88]

The mesh-free method is simple to implement and computationally inexpensive. It can, however, result in inaccuracy and convergence issues. In peridynamics, spatial derivatives are replaced with integrals. Thus, the numerical implementation of the peridynamic models greatly depend on the accuracy of the discretization of the integrals. One of the main sources of inaccuracy in this proposed mesh-free method is the estimation of the intersecting areas between the neighborhood of a point and its neighboring cells. Seleson [78] addressed this issue by classifying these intersecting regions for square lattices and presented analytical derivations for the calculation of their areas.

2.3 The Influence Function

In both the state and bond-based formulations, the force density function, \mathbf{f} can take the form

$$\mathbf{f}(\boldsymbol{\eta}, \boldsymbol{\xi}) = \omega(\xi) s \left(\frac{\boldsymbol{\xi}}{|\boldsymbol{\xi}|} \right)$$

where s , the bond stretch is defined as:

$$s = \frac{|\boldsymbol{\xi} + \boldsymbol{\eta}|}{|\boldsymbol{\xi}|}.$$

In some cases, the influence function, ω , can be selected arbitrarily [85]; or to address the inaccuracies in numerical integration [79]. However, it is clear that a proper choice *must* also take into consideration the physics of the problem [80], either through numerical upscaling procedures [109, 114] or by theoretical homogenization of microstructural heterogeneity [113]. Although this fact is well established, there is still no general procedure for the systematic computations of the influence function for a material or a given domain. In recent years, a few works have attempted to offer a general approach for the calculation of a physically meaningful influence function for a given domain. Delgossaie et al. [24] presented a numerical procedure for upscaling pore-network models into a continuum nonlocal formulation for single phase flow in porous media. The authors showed that the multi-scale connectivity of the pore networks can be used to extract the required influence function for the domain. D’Elia et al. [27] focused on finding the diffusivity parameter for peridynamic and fractional models by using an optimal control technique. You et

al. [114] looked at the problem of wave propagation through a one-dimensional heterogeneous bar. The authors offered a solution to find the optimal influence function through the use of a nonlocal-equation-constrained optimization algorithm. More recently, Xu et al. [112] introduced a data-driven regression algorithm for the calculation of the influence function. In this work a bond-based peridynamic model is used to simulate the macro-scale deformation of linear elastic medium with periodic heterogeneity.

In the following chapters the importance of the peridynamic influence function is explored in more depth. In chapter 4 a systematic approach for the calculation of a nonlocal influence function based on upscaling of an MD model of a Cu-Ar nanofluid will be presented.

2.4 Multi-scale Problems

Since its introduction the peridynamic theory has proven to be a powerful tool for multi-scale material modeling [4, 101]. Turbulence is an example of a problem in which large-scale phenomena are caused by small scale interactions. Turbulence, widely considered the oldest unsolved problem in physics, refers to the chaotic behavior of the pressure and velocity fields. Although the effects of turbulence can be experienced through the macroscopic features of a flow, its source lies in the interactions of the fluid particles at the microscopic scale. Small perturbations in the flow, whether formed within the boundary layer or introduced by the incoming flow field can be retarded by viscous forces. However, if the viscous forces are not able to dampen these perturbations, a

laminar flow can quickly transition to an unsteady and chaotic turbulent flow.

After many years of slow progress in turbulence modeling, fractional models have recently shown the advantages of a nonlocal approach. The “log law” approach traditionally offered a solution restricted to the interior region of the domain. However, a recent work by Song et al. [94] proposed a nonlocal fractional model capable of calculating the entire velocity profile from the wall to the centerline for channel, Couette and pipe flows. Equation 2.3 presents this fractional model.

$$\nu_0 \frac{\partial^2 U}{\partial y^2} + \nu(y) D_y^{\alpha(y)} U = f, \forall y \in \Lambda = (0, 1] \quad (2.2)$$

Here D_y^α is the Caputo fractional derivative, $f = \frac{\partial P}{\partial x} = 1$ is the dimensionless pressure gradient, $U(y)$ is the mean velocity and ν_0 is the kinematic viscosity.

The Caputo derivative is defined as

$$D_y^\alpha U(y) = \frac{1}{\Lambda(1-\alpha)} \int_0^y (y-\tau)^{-\alpha} U'(\tau) d\tau, \quad (2.3)$$

The Caputo derivative here is identical to the Reimann-Liouville left-sided derivative as $U(0) = 0$. In fractional models, the fractional order, $\alpha(y)$ can be thought of as a weight function that links the entire domain. This method can be used to prove the effectiveness of a nonlocal approach when simulating problems where the locality assumption does not hold. However, the fact that the entire domain is linked results in very high computational times. A peridynamic based nonlocal model can recover the fractional models with an

appropriate choice of the influence function [25, 26]. Therefore, the fractional calculus approach can be thought of as a special case of a larger family of peridynamic-based nonlocal models. Peridynamic-based models do not suffer from the shortcomings of fractional models caused by the fractional order. Here, the horizons typically cover an area much smaller than the full domain which results in lower computational times.

One of the early applications of peridynamic-based models for multi-scale modeling was presented by Bobaru et al. [13]. The authors showed that the peridynamic' horizon δ can be thought of as a length-scale. One of the main challenges of the multi-scale modeling approach is the appropriate modeling of the transitions from micro to macro scale. To address this problem, multiple works developed multi-scale numerical models to couple molecular dynamics (MD) and PD [69, 101].

2.5 Heat & Mass Transport Problems

Bobaru and Duangpanya [11, 12] used ideas from peridynamic mechanics to model isotropic transient heat conduction. They developed a non-local model capable of analyzing the physics of dynamic fractures in the presence of thermal gradient. Recent experiments on brittle polymers [73] have shown that upon rapid loading, the crack tip temperature can experience a significant drop. This change in the temperature can result in the transition from trans-granular to inter-granular fracture [41]. Furthermore, depending on the setup of the problem, this temperature change may also be important in the

ductile-to-brittle transition [21]. As a result, it is important to be able to include the thermal effects in modeling crack tip thermodynamics.

Du et al. [25,26] extended [12] to include advection-diffusion problems. The authors exploited nonlocal vector calculus to provide variational analysis of nonlocal diffusion problems. Using nonlocal vector calculus, their work also drew striking analogies between nonlocal models and classical models for diffusion, including the concept of nonlocal flux. In particular, the authors showed that fractional Laplacian and derivative models of anomalous diffusion can be considered as special cases of the peridynamic based nonlocal models.

Typically, when solving hyperbolic partial differential equations, up-winding scheme is used to resolve the instability issues experienced in the flow field. Applying up-winding in a finite differencing setting is a standard procedure. However, applying up-winding in a nonlocal setting requires special attention. Tian et al [99] expanded on [25,26] and presented a mathematically sound procedure for applying up-winding in a nonlocal setting. In summary, This method splits the horizon of a point into two semi-circles, centered at \mathbf{x} in upstream and downstream directions. All the calculations are then only based on the contributions of the neighbors in the upstream direction. Figure 2.3 depicts this concept.

Katyar et al. [45] used the aforementioned ideas and focused on modeling convective transport in anisotropic porous media. The classical theories of transport use constitutive equations for diffusion based on the assumption that the fluid flux is proportional to the gradient of a potential. However,

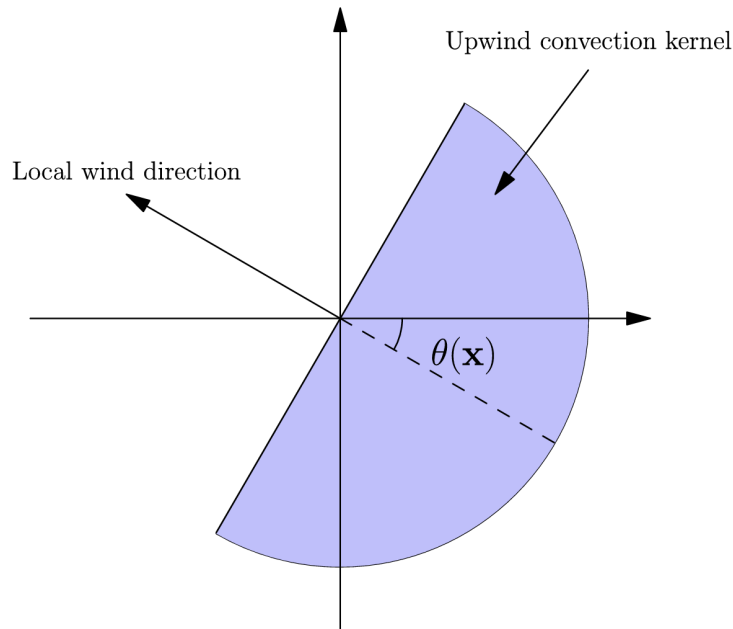


Figure 2.3: Horizon of each point in the domain is split into up-wind and down-wind halves based on the local flow velocity [99]

many scientific fields must solve problems in which the presence of anomalous diffusion breaks this underlying assumption. Examples of anomalous diffusion can be seen in studies of biomaterials [7] and polymers [35]. Anomalous diffusion is also experienced in the diffusion process through porous media. Here, the presence of long range channels means that the diffusion process does not follow Gaussian statistics. Figure 2.4 demonstrates how these long range channels in a porous media can link material points that are physically separated. In such domains, the flux at point \mathbf{x} is not only dictated by the local flux at \mathbf{x} but also by a function of the flux at point \mathbf{x}' . As a result, here a nonlocal model is a more appropriate tool for the analysis compared to its

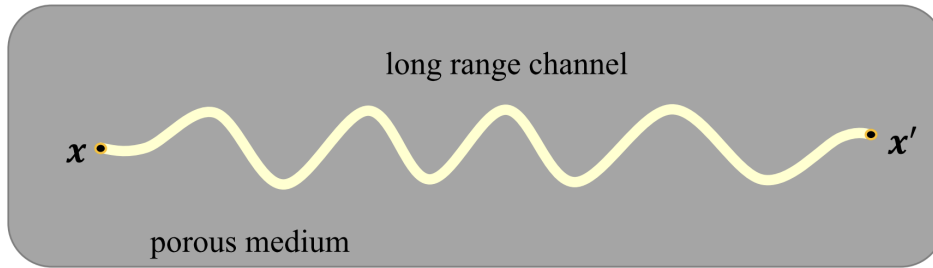


Figure 2.4: Long range channels in a porous media can serve as direct connection between point \mathbf{x} and its nonlocal neighbor \mathbf{x}' [45]

local counterparts. This work also introduced a mesh-free numerical technique that is can analyze heterogeneities, including highly irregular bodies with applications in tight pinch-outlets [71].

Sen et al. [82] also studied flow in porous media and proposed their nonlocal model as a method to deal with the multiscale pathways of a porous media. In their non-local model, the flow rate at each node is calculated based on the sum of the pressure differential between that node and every other node in the domain. In this formulation, each interaction is given a strength level. The authors used a conductivity kernel to define the strength of these connections and showed that their formulation would recover Darcy’s law as a special local case. Delgosaie et al. [24] expanded on [82] and provided an example for a systematic approach for the calculation of the conductivity kernel. In their work, the authors used a high-resolution pore network of a natural porous media in order to extract a physically meaningful conductivity

kernel and also demonstrated the convergence of their results to Darcy's law.

Jabakhanji et al. [39] used a peridynamic-based approach to arrive at a nonlocal model for transient flow in unsaturated, heterogenous and anisotropic soil. This model is an alternative for the classic Richard's equation. In this alternative approach, the absence of spatial derivatives allows the spurious formation of cracks, which would result in singularities in the parameter of hydraulic potential fields. Delgosaie et al. [24] presented a non-local approach to model flow in porous media. The authors also used the multi-scale pore-network connections to extract a physically meaningful influence function for their peridynamic based model.

Madenci et al. [53, 54] introduced peridynamic differential operators, PDDO, as a mathematical technique to represent spatial derivatives of classical models in nonlocal form. More recently, Nguyen [60] used the PDDO to model Eulerian incompressible fluid flow. The authors demonstrated the capabilities of the PDDO method for tackling multi-scale problems by modeling the vortex shedding in a 2-dimensional problem of flow over a cylinder.

Chapter 3

A nonlocal advection-diffusion model for two-phase miscible flow in porous media

3.1 Introduction

Viscous fingering is an interface instability that can occur between two or more phases in miscible multiphase fluid flow. It is characterized by a highly irregularly shaped interface, often with long “fingers” of the displacing phase propagating far into the phase(s) being displaced. Although many secondary effects may be responsible for the onset and propagation of viscous fingers, most researchers consider the principle controlling mechanism to be the viscosity ratio between phases. Spatial changes in pressure are lower in the phase with lower viscosity leading to higher pressure in the leading edge of the fingers. This causes a force imbalance that assists in propagating the interface rapidly forward into the more viscous phase. Other characteristic features of the fingers often include splitting of fingers into multiple smaller fingers or shielding of some fingers by a rapidly growing finger that is spatially placed ahead in the velocity field.

As the formation and propagation of fingers occur, a competition between two main features of the flow is apparent. In one case, the increased

contact area of the phases will drive a higher mixing rate. In the other, the isolation of large parts of the displaced fluid between fingers results in lower mixing. Previously, experimental and numerical approaches have provided results that have shed light on the general behavior of the fingers in a laboratory and/or idealized settings. However, an unexplored aspect that is highly influential in large-scale subsurface applications is the effect of dispersion on the onset and propagation of viscous fingers and how it contributes to the overall phase mixing. This chapter aims to investigate the effect of fluid dispersion on miscible mixing and the formation, size, shape, and trajectory of viscous fingers in the context of subsurface engineering applications.

Saffman and Taylor [75] were among the first to explore viscous fingering using Hele-Shaw cells to mimic two-dimensional creeping fluid flow in a porous media. In their study the authors described a mathematical model that could explain viscous fingering for a two-phase immiscible flow given that the displaced fluid would form a film layer of constant thickness between the plates of Hele-Shaw apparatus. Later works by Park and Homsy [65] and Reinelt [70] expanded this model to allow the study of two phase flow where displacing fluid can potentially wet the surface and thus provided a “fix” for the boundary condition assumptions of the Saffman and Taylor model. These models were further enhanced by the contributions of Wilson [111] and Paterson [66] that explored the instability of radial flows from a central point source. The studies mentioned here and other research during 1980s and 90s added to the validation of this experimental approach. However, dispersion

cannot be elucidated in Hele-Shaw cell experiments due to the underlying homogeneous medium; nevertheless, it can be significant in applications of miscible displacements such as secondary and tertiary oil recovery in the field of petroleum engineering [49].

More recently, numerical simulations using finite difference and finite element approaches have been used to model initiation and propagation of fingers [77,91]. While these numerical simulations can be tools for exploring many factors involved in viscous fingering, the underlying physical equations that they discretize are void of any dispersive effects [3,45], i.e. any observed dispersion is numerical. Occasionally, the underlying partial-differential equations used to model subsurface fluid flow are parameterized with time-dependent diffusion coefficients to account for dispersion; however, the physical justification for this assumption is not well established in many cases (e.g. when modeling Newtonian fluids). Dispersion is a spatial phenomenon in the subsurface caused by heterogeneities at length scales smaller than what are typically resolved in a fluid transport simulation.

Classical models used in simulation of transport phenomena use governing laws in which fluid flux is linearly related to a potential, e.g. Fick's and Darcy's laws. These models can be derived by statistical analyses assuming the Brownian motion of diffusing particles. The core assumptions of a diffusion process, the Markovian nature of the underlying statistics, is often not valid for heterogeneous domains where analysis of diffusing tracer particles lead to non-Gaussian, e.g. heavy-tailed, spatial distributions. These processes are

termed *anomalous diffusion* and include sub- and super-diffusion as particular cases [57]. Examples of anomalous diffusion are seen in polymers [35, 62], biomaterials [6] and even in the field of biology when looking at the foraging habits of animals [47].

In the case of porous media, small-scale heterogeneities result in sudden changes in permeability which are then responsible for fluctuations in diffusion particles velocity. The transport characteristics of a domain with such heterogeneities, can be modeled with equations that allow for the fluid velocity at a point \mathbf{x} to depend not only on the local properties (i.e. permeability, viscosity, concentration, etc.) but also at points \mathbf{x}' separated from \mathbf{x} by a finite distance. These models are called *nonlocal models* and can be rigorously derived by considering non-Gaussian statistics such as Levy flights.

Typically, spatially nonlocal physics are analyzed with a fractional derivative approach [57] or with the use of integral equations [82]. The latter is more general and the method chosen for the current investigation of viscous fingering in dispersive media. An example of an integral-type nonlocal model called *peridynamics* theory was introduced by Silling [86] to model elasticity and material failure in solid mechanics. Silling's initial work was focused on the derivation of a set of integral-differential equations for conservation of momentum in solid structures. This work became the foundation of a theory that has turned into a promising modeling tool. Bobaru and Duangpanya [11,12] used ideas from peridynamic mechanics to model isotropic transient heat conduction. This work was extended to advection-diffusion problems by

Gunzburger et al. [25, 26]. Katyar et al. [45] focused on anisotropic porous media and discussed the case of a transient fluid flow in fractured media. The current study, to the extent of our knowledge, is the first nonlocal model for advection-diffusion processes in two-phase miscible flow. The proposed model is developed to simulate complex two-phase fluid flow in a dispersive porous media and shows the advantages of the integral-type formulation, both in accurately capturing the physics of the problem and its versatility in dealing with the discontinuities at the interface of the phases.

This chapter starts by introducing a nonlocal advection-diffusion model for two-phase flow in porous media. We will specifically explore the fluid interaction as the viscosity ratio between the displaced and displacing phases is varied and show results of the viscous fingering simulations for one and two dimensional cases. We also show the convergence of the introduced nonlocal model to both the mathematical (local) continuum model and the computed solutions of its finite differencing discretization for both pressure and concentration as the local limit is approached.

In this work we have assumed the relationship between kinematic viscosity and phase concentration to have an exponential form. Additionally, it is assumed that the flow is a Darcy type flow and both phases are incompressible, first contact miscible, and diffusivity coefficient is constant. With these assumptions, the local form of the model reduces to an advection-diffusion

system of equations similar to those presented in [42], i.e.

$$0 = \frac{\partial c}{\partial t} - \frac{1}{\mu(c)} \nabla p \nabla c - \frac{1}{Pe} \Delta c, \quad (3.1a)$$

$$0 = R \nabla c \nabla p + \Delta p, \quad (3.1b)$$

where, c is the concentration, t is time, μ is kinematic viscosity, p is pressure, Pe is the Peclet number and R is defined as $\frac{\mu_2}{\mu_1}|_{t=0}$ where the subscripts 1 and 2 refer to the phases. ∇ and $\Delta = \nabla \cdot \nabla$ are the spatial gradient and Laplacian operators, respectively. In this model the (3.1a) is a form of an advection-diffusion equation (ADE) and the (3.1b) describes both the viscosity-concentration relation and the incompressibility assumption.

The remainder of this chapter is organized as follows: Section 2 presents the mathematical structure of the nonlocal model and provides convergence proofs that the model reduces to (3.1) in the limit of vanishing nonlocality. Section 3 describes the discretization of the nonlocal model. Section 4 presents numerical verification simulations as well as several qualitative case studies along with respective discussion. Section 5 presents conclusions and recommendations for future work.

3.2 Nonlocal Model

To introduce the proposed nonlocal model, we adopt the notation and terminology from peridynamic mechanics. Namely, we assume that a point \mathbf{x} interacts with all points $\mathbf{x} + \boldsymbol{\xi}$ within a finite distance parameterized by ϵ called the *horizon*. The set of all points $\mathbf{x} + \boldsymbol{\xi}$ is called the *neighborhood* of

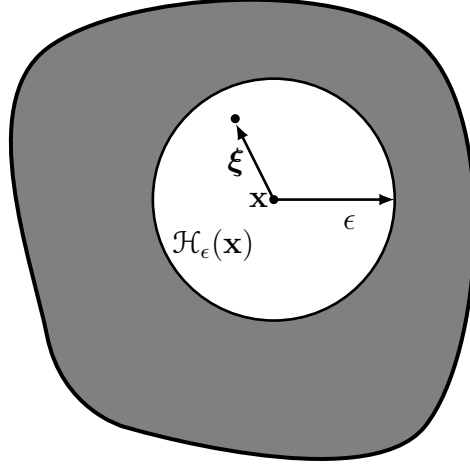


Figure 3.1: Point \mathbf{x} and its horizon shown in white. $\boldsymbol{\xi}$ is a vector connecting \mathbf{x} to another point in the neighborhood and ϵ is the radius of the horizon.

\mathbf{x} , and is labeled $\mathcal{H}_\epsilon(\mathbf{x})$. We will assume a spherical neighborhood in three dimensions and circular in two-dimensions (therefore ϵ is a radius), but other choices are available. An illustration of these concepts is shown in fig. 4.1.

The proposed nonlocal model is then given by (3.2)

$$0 = \frac{\partial c}{\partial t} - \frac{1}{\mu(c)} \int_{\mathcal{H}_\epsilon} \gamma \omega(|\boldsymbol{\xi}|) (p(\mathbf{x} + \boldsymbol{\xi}) - p(\mathbf{x})) \frac{\xi_i}{|\boldsymbol{\xi}|^2} d\boldsymbol{\xi} \times \quad (3.2a)$$

$$\int_{\mathcal{H}_\epsilon} \gamma \omega(|\boldsymbol{\xi}|) (c(\mathbf{x} + \boldsymbol{\xi}) - c(\mathbf{x})) \frac{\xi_i}{|\boldsymbol{\xi}|^2} d\boldsymbol{\xi} - \frac{2}{Pe} \int_{\mathcal{H}_\epsilon} \gamma \frac{\omega(|\boldsymbol{\xi}|)}{|\boldsymbol{\xi}|^2} (c(\mathbf{x} + \boldsymbol{\xi}) - c(\mathbf{x})) d\boldsymbol{\xi},$$

$$0 = R \int_{\mathcal{H}_\epsilon} \gamma \omega(|\boldsymbol{\xi}|) (p(\mathbf{x} + \boldsymbol{\xi}) - p(\mathbf{x})) \frac{\xi_i}{|\boldsymbol{\xi}|^2} d\boldsymbol{\xi} \int_{\mathcal{H}_\epsilon} \gamma \omega(|\boldsymbol{\xi}|) (c(\mathbf{x} + \boldsymbol{\xi}) - c(\mathbf{x})) \frac{\xi_i}{|\boldsymbol{\xi}|^2} d\boldsymbol{\xi}$$

$$+ \int_{\mathcal{H}_\epsilon} 2\gamma \frac{\omega(|\boldsymbol{\xi}|)}{|\boldsymbol{\xi}|^2} (p(\mathbf{x} + \boldsymbol{\xi}) - p(\mathbf{x})) d\boldsymbol{\xi}, \quad (3.2b)$$

where c, t, μ, p, R, Pe all have the same meaning as in (3.1). We've dropped the functional dependence of c and p on t , but it is implied. ω is called the

influence function and controls the strength of interactions among the points in the neighborhood. The choice of influence function will be discussed in more detail in the sequel. Finally, γ is a scaling function whose choice is discussed in the following sections.

A requirement for the validity of the nonlocal model is that it should converge to (3.1) as $\epsilon \rightarrow 0$. The proof of this is somewhat tedious and would yield unwieldy derivations if addressing the entire system of equations (3.2) at once. To avoid this, we will break the equations down term-by-term to demonstrate the convergence of the integral operators to their local derivative operator counterparts in the limit of vanishing horizon.

3.2.1 Nonlocal Gradient

Inspecting the first integral in (3.2a) we can show that it will converge to the local gradient operator. First, we assume the pressure field is continuous such that the Taylor expansion about $\boldsymbol{\xi} = \mathbf{0}$ exists

$$p(\mathbf{x} + \boldsymbol{\xi}) = p(\mathbf{x}) + \frac{\partial p}{\partial x_j}(\mathbf{x})\xi_j + \mathcal{O}(|\boldsymbol{\xi}|^2). \quad (3.3)$$

Substituting (5.7) into the first integral in (3.2a) and taking the limit as $\epsilon \rightarrow 0$

$$\begin{aligned}
& \lim_{\epsilon \rightarrow 0} \int_{\mathcal{H}_\epsilon} \gamma \omega(|\boldsymbol{\xi}|) (p(\mathbf{x} + \boldsymbol{\xi}) - p(\mathbf{x})) \frac{\xi_i}{|\boldsymbol{\xi}|^2} d\boldsymbol{\xi} \\
&= \lim_{\epsilon \rightarrow 0} \gamma \int_{\mathcal{H}_\epsilon} \frac{\omega(|\boldsymbol{\xi}|)}{|\boldsymbol{\xi}|^2} (p(\mathbf{x})\xi_i + \frac{\partial p}{\partial x_j}(\mathbf{x})\xi_i\xi_j - p(\mathbf{x})\xi_i) + \mathcal{O}(|\boldsymbol{\xi}|^2) d\boldsymbol{\xi}, \\
&= \lim_{\epsilon \rightarrow 0} \frac{\partial p}{\partial x_j}(\mathbf{x}) \gamma \int_{\mathcal{H}_\epsilon} \omega(|\boldsymbol{\xi}|) \frac{\xi_j \xi_i}{|\boldsymbol{\xi}|^2} + \mathcal{O}(|\boldsymbol{\xi}|^2) d\boldsymbol{\xi}, \\
&= \lim_{\epsilon \rightarrow 0} \frac{\partial p}{\partial x_j}(\mathbf{x}) \delta_{ji} + \mathcal{O}(\epsilon), \\
&= \lim_{\epsilon \rightarrow 0} \frac{\partial p}{\partial x_i}(\mathbf{x}) + \mathcal{O}(\epsilon), \\
&= \nabla p.
\end{aligned}$$

Note, as shown below, there is an ϵ^2 term in the denominator of γ which explains the $\mathcal{O}(\epsilon)$ after integration. Here $\omega(|\boldsymbol{\xi}|) = \omega_s(|\boldsymbol{\xi}|)$ is assumed to be spherically symmetric which implies that

$$\begin{aligned}
\int_{\mathcal{H}_\epsilon} \omega_s(|\boldsymbol{\xi}|) \frac{\xi_k \xi_j}{|\boldsymbol{\xi}|^2} d\boldsymbol{\xi} &= \delta_{kj} \int_{\mathcal{H}_\epsilon} \omega_s(|\boldsymbol{\xi}|) \frac{\xi_1^2}{|\boldsymbol{\xi}|^2} d\boldsymbol{\xi}, \\
&= \delta_{kj} \int_0^{2\pi} \int_0^\pi \int_0^\epsilon \omega_s(|\boldsymbol{\xi}|) \frac{\xi_1^2}{|\boldsymbol{\xi}|^2} |\boldsymbol{\xi}|^2 \sin \theta d\xi d\theta d\phi, \\
&= \delta_{kj} \frac{m_1}{3},
\end{aligned}$$

where

$$m_1 = \int_{\mathcal{H}_\epsilon} \omega_s(|\boldsymbol{\xi}|) d\boldsymbol{\xi},$$

and we have used the spherical coordinates, $\xi_1 = |\boldsymbol{\xi}| \sin \theta \cos \phi$, $\xi_2 = |\boldsymbol{\xi}| \sin \theta \sin \phi$, and $\xi_3 = |\boldsymbol{\xi}| \cos \theta$ to evaluate the integral. Therefore, in order for the first in-

tegral in (3.2a) to converge to ∇p in the limit of vanishing horizon, we require

$$\gamma = \frac{3}{m_1}.$$

Using an identical procedure, we can show that the second integral in (3.2a) will reduce to the spatial gradient of concentration as the horizon vanishes, i.e.

$$\lim_{\epsilon \rightarrow 0} \int_{\mathcal{H}_\epsilon} \gamma \omega(|\boldsymbol{\xi}|) (c(\mathbf{x} + \boldsymbol{\xi}) - c(\mathbf{x})) \frac{\xi_i}{|\boldsymbol{\xi}|^2} d\boldsymbol{\xi} = \nabla c(\mathbf{x}).$$

3.2.2 Nonlocal Laplacian

Now we address the last term in (3.2a) and demonstrate that it converges to the Laplacian operator shown in (3.1a) as $\epsilon \rightarrow 0$. Following a similar procedure as the last section, this time we start with Taylor expansion of

$c(\mathbf{x} + \boldsymbol{\xi})$ about $\boldsymbol{\xi} = \mathbf{0}$ with a truncation error of $\mathcal{O}(|\boldsymbol{\xi}|^3)$

$$\begin{aligned}
& \lim_{\epsilon \rightarrow 0} \frac{2}{Pe} \int_{\mathcal{H}_\epsilon} \gamma \frac{\omega(|\boldsymbol{\xi}|)}{|\boldsymbol{\xi}|^2} (c(\mathbf{x} + \boldsymbol{\xi}) - c(\mathbf{x})) d\boldsymbol{\xi} = \\
&= \lim_{\epsilon \rightarrow 0} \frac{2}{Pe} \gamma \int_{\mathcal{H}_\epsilon} \frac{\omega(|\boldsymbol{\xi}|)}{|\boldsymbol{\xi}|^2} (c(\mathbf{x} + \boldsymbol{\xi}) - c(\mathbf{x})) d\boldsymbol{\xi}, \\
&= \lim_{\epsilon \rightarrow 0} \frac{2}{Pe} \gamma \int_{\mathcal{H}_\epsilon} \frac{\omega(|\boldsymbol{\xi}|)}{|\boldsymbol{\xi}|^2} \left(\frac{\partial c}{\partial x_i} \xi_i + \frac{1}{2} \frac{\partial^2 c}{\partial x_i \partial x_j} \xi_i \xi_j + \mathcal{O}(|\boldsymbol{\xi}|^3) \right) d\boldsymbol{\xi}, \\
&= \lim_{\epsilon \rightarrow 0} \frac{2}{Pe} \gamma \int_{\mathcal{H}_\epsilon} \frac{\omega(|\boldsymbol{\xi}|)}{|\boldsymbol{\xi}|^2} \left(\frac{1}{2} \frac{\partial^2 c}{\partial x_i \partial x_j} \xi_i \xi_j + \mathcal{O}(|\boldsymbol{\xi}|) \right) d\boldsymbol{\xi}, \\
&= \lim_{\epsilon \rightarrow 0} \frac{2}{Pe} \gamma \int_{\mathcal{H}_\epsilon} \frac{\omega(|\boldsymbol{\xi}|)}{|\boldsymbol{\xi}|^2} \left(\frac{1}{2} \frac{\partial^2 c}{\partial x_i \partial x_j} \xi_i \xi_j \right) d\boldsymbol{\xi} + \mathcal{O}(\epsilon), \\
&= \lim_{\epsilon \rightarrow 0} \frac{2}{Pe} \gamma \frac{1}{2} \frac{\partial^2 c}{\partial x_i \partial x_j} \int_{\mathcal{H}_\epsilon} \frac{\omega(|\boldsymbol{\xi}|)}{|\boldsymbol{\xi}|^2} (\xi_i \xi_j) d\boldsymbol{\xi} + \mathcal{O}(\epsilon), \\
&= \lim_{\epsilon \rightarrow 0} \frac{1}{Pe} \frac{\partial^2 c}{\partial x_i \partial x_j} \delta_{ij} + \mathcal{O}(\epsilon), \\
&= \lim_{\epsilon \rightarrow 0} \frac{1}{Pe} \frac{\partial^2 c}{\partial x_i \partial x_i} + \mathcal{O}(\epsilon), \\
&= \frac{1}{Pe} \Delta c,
\end{aligned}$$

where γ and m_1 have the definitions as in §3.2.1.

Similarly, it can be shown that the last term in (3.2b) converges to the pressure Laplacian in (3.1b), i.e.

$$\lim_{\epsilon \rightarrow 0} \int_{\mathcal{H}_\epsilon} 2\gamma \frac{\omega(|\boldsymbol{\xi}|)}{|\boldsymbol{\xi}|^2} (p(\mathbf{x} + \boldsymbol{\xi}) - p(\mathbf{x})) d\boldsymbol{\xi} = \Delta p.$$

We've now addressed the convergence of all terms in (3.2) and can confirm that (3.2) \rightarrow (3.1) as $\epsilon \rightarrow 0$.

3.2.3 Influence Function

There are infinite choices for the influence function ω , and under some circumstances the choice can be arbitrary [85]; however, the choice is usually made to address inaccuracies in numerical integration [79]. A proper choice *must* take into consideration the physics of the problem [80], either through numerical upscaling procedures [109,114] or by theoretical homogenization of microstructural heterogeneity [113]. Delgosaie et al. [24] presented a numerical procedure for upscaling pore-network models into a continuum nonlocal formulation for single phase flow in porous media. The correct choice for the physical setting where viscous fingering occurs will be the subject of future work. When investigating the convergence to the local limit of the nonlocal model, all admissible choices will result in a convergence to the local equations. Solely for demonstrating this point we will show the closed form integration of m_1 with a few common functional forms of the influence function.

3.2.3.1 Constant

Choosing a constant value such as unity for the influence function means that the same weight is given to all neighbors. For the one dimensional case, we have

$$m_1 = 2 \times \int_{\mathcal{H}_\epsilon} \xi d\xi = 2 \times \left[\frac{\xi^2}{2} \right]_0^{+\epsilon} = \epsilon^2.$$

3.2.3.2 Linear

Choosing a linear decaying profile for ω is a popular choice that can improve the accuracy of the numerical integration within the neighborhood.

We chose $\omega(|\xi|) = 1 - \frac{|\xi|}{\epsilon}$. As before, for the one dimensional case

$$m_1 = 2 \times \int_0^\epsilon \left(1 - \frac{\xi}{\epsilon}\right) \xi d\xi = 2 \times \left[\frac{\xi^2}{2} - \frac{\xi^3}{3\epsilon} \right]_0^\epsilon = \frac{\epsilon^2}{3}.$$

For the case of two dimensional domain, horizon takes the form of a circle with radius ϵ . In this case $\gamma = 2/m$

$$\begin{aligned} m &= \int_0^{2\pi} \int_0^\epsilon \omega(\xi) \xi d\theta d\xi = \int_0^{2\pi} \int_0^\epsilon \left(1 - \frac{\xi}{\epsilon}\right) \xi d\theta d\xi = \left[\frac{\xi^2}{2} - \frac{\xi^3}{3\epsilon} \right]_0^\epsilon, \\ &= \frac{\epsilon^2 \pi}{3}. \end{aligned}$$

3.3 Discretization

For the nonlocal simulations, we have chosen equally spaced nodes with a typical horizon size of 4.5 node spacings. For the presented results, the Peclet number and R were respectively chosen to be 10000 and 3.0. Discretization of the domain into finite number of nodes also results in the conversion of the integral equations to finite sums. Equation (4.4) states the equations solved for the nonlocal simulations. NOX package from Trilinos was used to tackle these non-linear equations. All simulations were solved using a massively parallel python code ran on STAMPEDE super computer at the University of Texas at Austin. The discretized form of the nonlocal model is presented by (4.4)

$$\begin{aligned}
0 &= \frac{c^{n+1}(\mathbf{x}_i) - c^n(\mathbf{x}_i)}{\Delta t} - \frac{1}{\mu(c)} \sum_j \gamma \omega(|\boldsymbol{\xi}|) (p^{n+1}(\mathbf{x}_j) - p^{n+1}(\mathbf{x}_i)) \frac{\xi_\alpha}{|\boldsymbol{\xi}|^2} A_j \\
&\quad \times \sum_j \gamma \omega(|\boldsymbol{\xi}|) (c^{n+1}(\mathbf{x}_j) - c^{n+1}(\mathbf{x}_i)) \frac{\xi_\alpha}{|\boldsymbol{\xi}|^2} A_j \\
&\quad - \frac{2}{Pe} \sum_j \gamma \frac{\omega(|\boldsymbol{\xi}|)}{|\boldsymbol{\xi}|^2} (c^{n+1}(\mathbf{x}_j) - c^{n+1}(\mathbf{x}_i)) A_j, \tag{3.4a}
\end{aligned}$$

$$\begin{aligned}
0 &= R \sum_j \gamma \omega(|\boldsymbol{\xi}|) (p^{n+1}(\mathbf{x}_j) - p^{n+1}(\mathbf{x}_i)) \frac{\xi_\alpha}{|\boldsymbol{\xi}|^2} A_j \\
&\quad \times \sum_j \gamma \omega(|\boldsymbol{\xi}|) (c(\mathbf{x}_j) - c(\mathbf{x}_i)) \frac{\xi_\alpha}{|\boldsymbol{\xi}|^2} A_j \\
&\quad + \sum_j 2\gamma \frac{\omega(|\boldsymbol{\xi}|)}{|\boldsymbol{\xi}|^2} (p^{n+1}(\mathbf{x}_j) - p^{n+1}(\mathbf{x}_i)) A_j. \tag{3.4b}
\end{aligned}$$

Above A_j can be thought of as Δx^2 for 2-D case and as Δx for the 1-D case. α subscript represents x and y directions. Here $\mathbf{x}_j := \mathbf{x}_i + \boldsymbol{\xi}$ where j stands for a neighboring node and x_i is the spatial position of the node of interest.

The inherent non-linear nature of the ADE makes the simulations unstable. This is especially important for the concentration solution. A common procedure to avoid this unstable behavior is up-winding. This procedure was used both for the finite differencing solution and the nonlocal simulations. The up-winding procedure for finite differencing solution is a standard procedure and does not require further explanation. However, applying the up-winding procedure in a nonlocal setting requires some attention. Tian et al [99] have presented a mathematically sound procedure for applying up-winding in a non-local setting. In summary, This method splits the horizon of a point into two semi-circles, centered at \mathbf{x} in upstream and downstream directions. All the

calculations are then done only based on the contributions of the neighbors in the upstream semi-circle.

In order to implement this method, the code calculates the velocity field, \mathbf{v} for every node \mathbf{x} in the domain. The dot product between the velocity field and the array holding all position vectors, $\boldsymbol{\xi}$, is then calculated for the neighbors of \mathbf{x} . The resultant array will have negative values for all the nodes upstream of \mathbf{x} and positive values for all the neighbors that are downstream of \mathbf{x} . Applying the Sign function, $Sgn(\mathbf{v} \cdot \boldsymbol{\xi})$ and replacing all 1 with 0 and -1 with 1, brings us to the final step of the calculation. In this final step, the inner product of the calculated vector with the concentration terms of equation 3.2 is calculated. This will exclude the contribution from all the neighbors downstream of \mathbf{x} . This procedure is repeated for every iteration of the solver. Figure 3.2 shows this procedure applied to point \mathbf{x} . The green semi-circle includes all the neighbors of point \mathbf{x} that are located upstream of the this point and contribute to the concentration calculation.

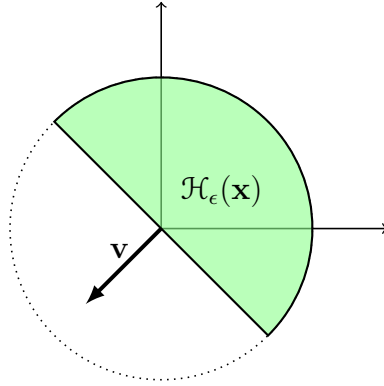


Figure 3.2: Up-winding applied to the neighborhood of point \mathbf{x} . Here \mathcal{H}_ϵ is the horizon and \mathbf{v} shows the local wind direction

3.4 Results and Discussion

We have formally derived a nonlocal set of equations capable of modeling two-phase miscible flow in porous media. The convergence of the model to the classical results as ξ approaches zero was mathematically proven. In what follows, the convergence of the numerical method using a 2-D, two-phase miscible flow case with a flat interface is shown. Disturbance is then introduced at the phase interface in order to study the two dimensional linear and radial flow cases and show the capabilities of the proposed method in modeling the formation and propagation of fingers while capturing the effects of dispersion. Here, periodic boundary condition is used for the top and bottom edges. Figure 3.3 demonstrates this concept by showing the horizon for 3 randomly chosen nodes in the domain. In this setup, a node placed at the bottom edge (here shown in blue) has half of its neighbors on the top boundary of the domain and half at the bottom edge.

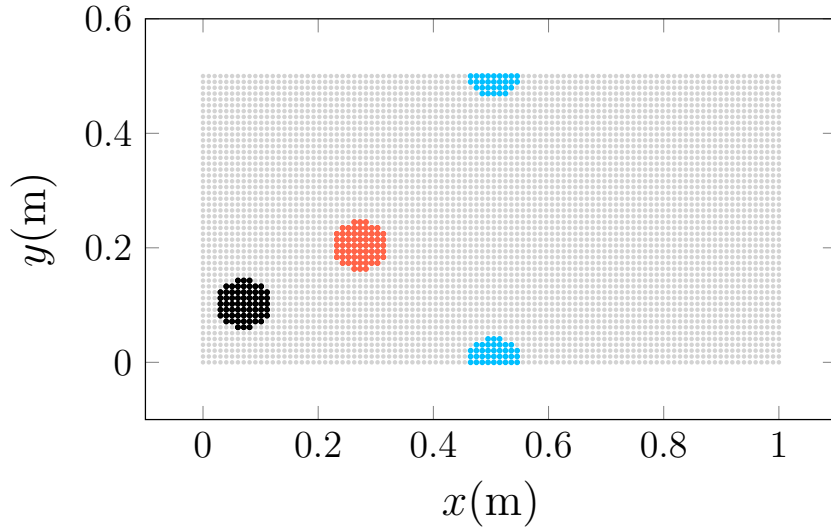


Figure 3.3: Illustration of how horizon of a point can be split at the edges of the domain

3.4.0.1 Parametrization

We have solved the proposed flat interface problem with the following parameters. The domain length, $L = 1$ m, domain height, $h = 0.5$ m, $\mu_1 = 1.0$ and $R = 1.0$. $Pe = 10^4$ and the pressure difference between the right and left edges is set to 1 kPa.

3.4.0.2 Boundary Conditions

Imposing the Dirichlet boundary conditions for the nonlocal model can be done by setting the value of all nodes within a horizon distance from the left and right boundaries equal to the desired value. Imposing the periodic

boundary condition can be done by linking the top and bottom nodes together. In this condition, all the nodes within one horizon from the top and bottom edges will have at least one neighbor on the opposite side.

3.4.1 Case 1: Finite Differencing Scheme

A backward in time, central differencing method was used to calculate and solve the pressure field. However, the non-linearity in the advection diffusion equation makes this method unstable when solving for concentration. Up-winding was used to stabilize the concentration solution. This method is explicit in both pressure and concentration. The set of equations used are direct translations of (3.1) with the addition of up-winding to the gradient term of the concentration. It is clear that a two dimensional problem with a flat interface between the two phases can be modeled as a one dimensional problem. Therefore to save computational time, the equivalent 1D problem was solved. The nonlocal model was however solved both in one and two dimensions to make sure that the results do in fact match.

3.4.1.1 Parametrization

The finite differencing problem has been solved with the following parameters. The domain length, $L = 1$ m, domain height, $h = 0.5$ m, $\mu_1 = 1.0$ and $R = 1.0$. $Pe = 10^4$ and the pressure difference across the right and left edges was set at 1 kPa.

3.4.1.2 Boundary Conditions

To be consistent with the nonlocal solution, the Dirichlet boundary condition was imposed on left and right boundaries. The top and bottom boundaries were also linked to achieve the periodic boundary condition.

3.4.2 Case 1: Convergence Study

The exact nonlocal solution can only be calculated as m , the number of nodes that radially fit into the horizon, approaches infinity. Although a supercomputer and in some cases up to 256 computational nodes were used to solve the non-linear model, the simulations were still limited by the available computation hours on the supercomputer. Thus, a typical convergence test for nonlocal models called m -convergence was performed to understand the required node density for a satisfactory result. The m -convergence study revealed that for a constant horizon size, an m value between 4 and 6 will result in an acceptable solution. This finding is in close agreement with the study of Katiyar et al. [45].

Running the m -convergence test helps us study the convergence of the model to the exact nonlocal solution. This exact nonlocal solution, however, is not the same as the local solution achieved through finite differencing. Getting to the local solution is only possible when the discretization is refined at a higher rate as the rate at which m is increased [12, 14]. Following figures show the convergence of the nonlocal model to the solution of the finite differencing

scheme of section 3.4.1 for both pressure and concentration. Figure 3.4 shows the convergence of the nonlocal model to the solution of the one-dimensional advection diffusion problem for concentration, while the same result for pressure is presented on figure 3.5.

3.4.3 Case 2: Disturbed Interface

In their 1958 paper, Saffman and Taylor [75] introduces the idea of Saffman-Taylor instability which is now widely know as viscous fingering. The initiation of this phenomena is naturally triggered by the heterogeneities of a physical domain. However, capturing this event in a numerical study requires an initially disturbed interface. As it happens, placing a disturbance in the interface is all that is needed to capture this instability using the advection diffusion equations. In what follows, we present the results of flow simulations with a disturbed interface for the nonlocal model and show that the proposed model also captures this phenomena without the need for any further modification.

3.4.3.1 Parametrization

For the first study, disturbance is added to the flat interface of case 1. For the specific results presented, $m = 4.5$ and $\Delta x = L/1600$. Peclet number is set at 10000 and $R = 3.0$.

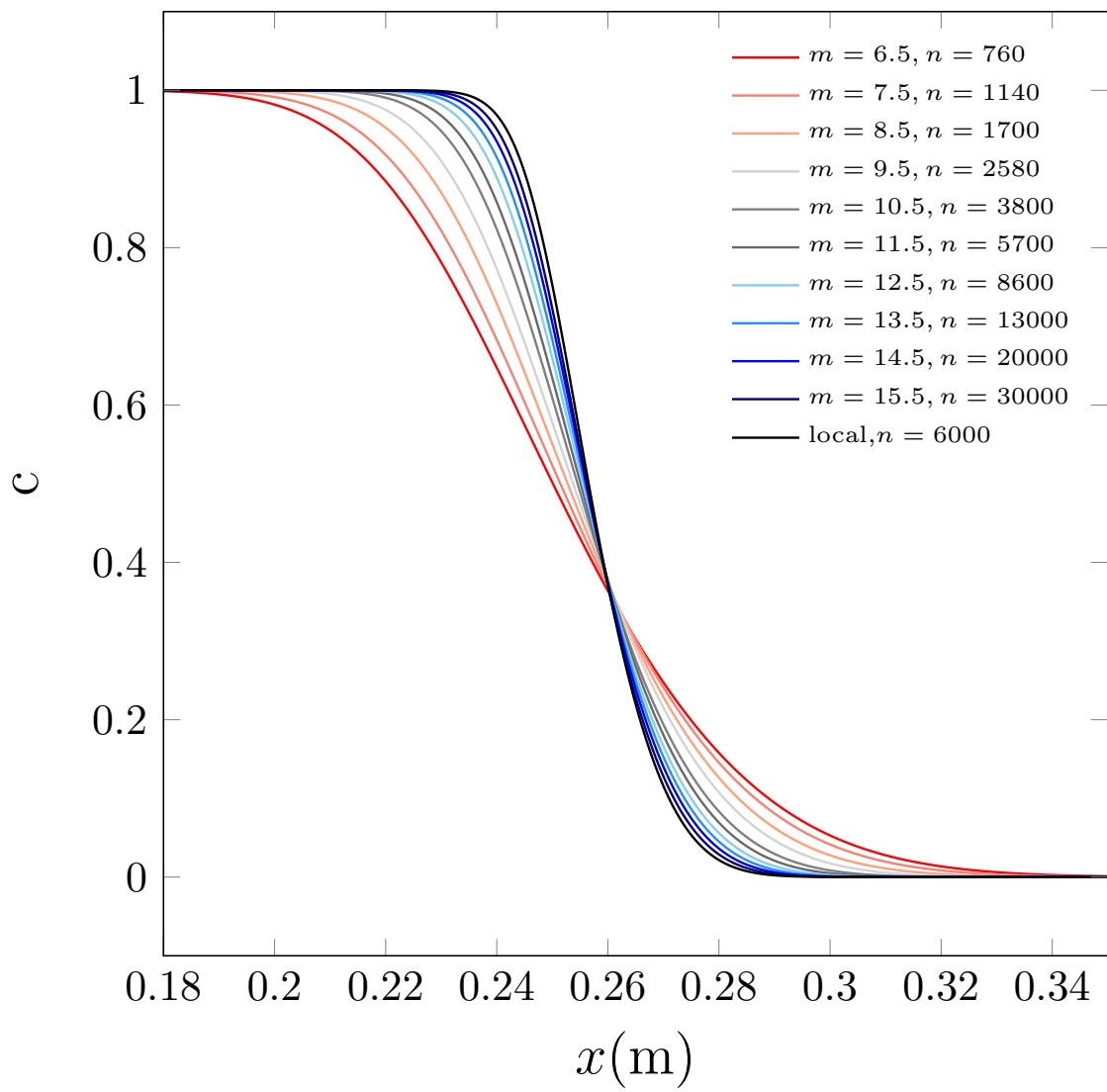


Figure 3.4: Convergence of concentration solution of the nonlocal model to the finite differencing solution drawn in black

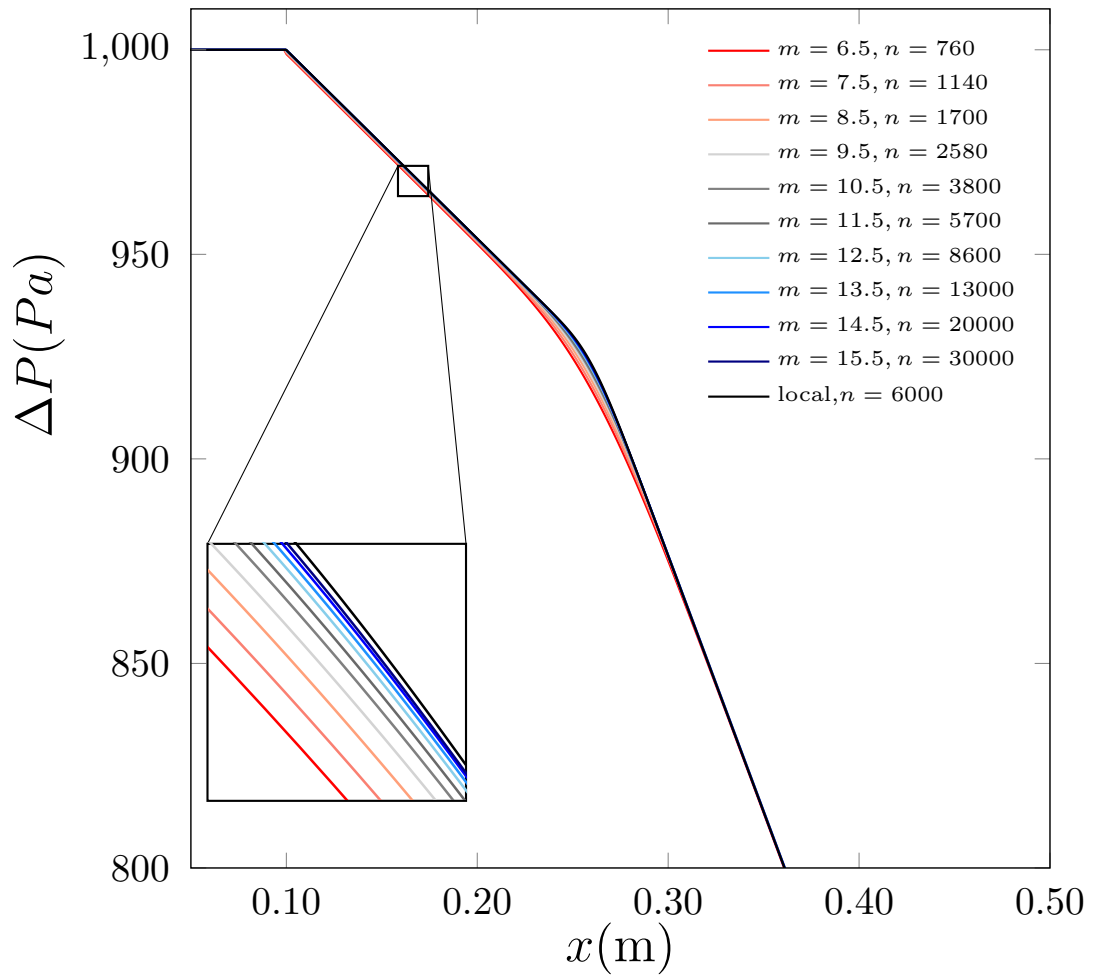


Figure 3.5: Convergence of pressure solution of the nonlocal model to the finite differencing solution drawn in black

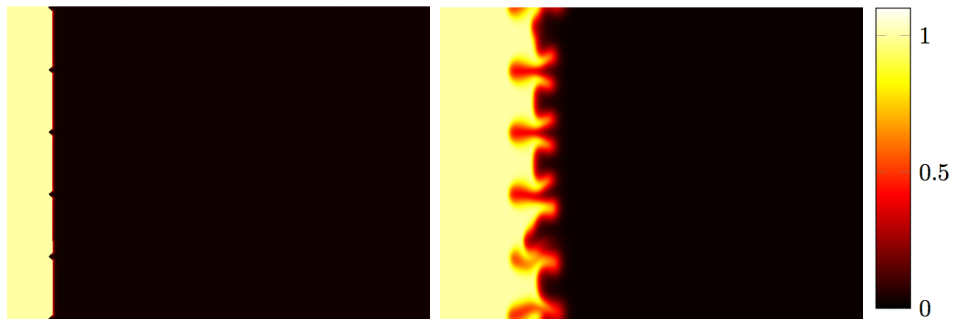
3.4.3.2 Boundary Conditions

This simulation also has Dirichlet boundaries for left and right edges and periodic boundary conditions for the top and bottom edges. In this case, the disturbance is added to the interface at time zero and it is held long enough for the fingers to form.

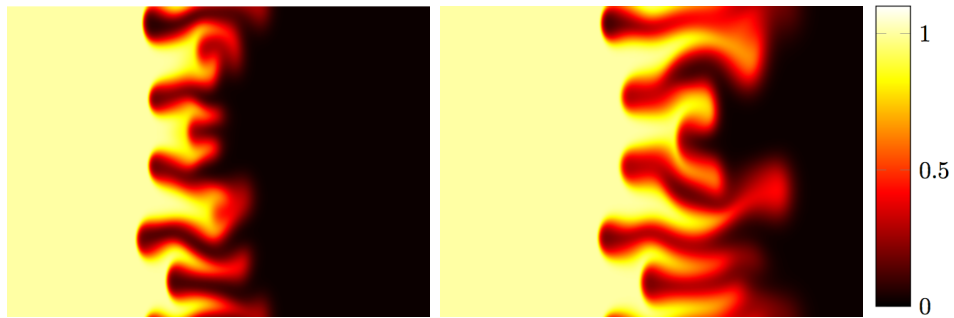
3.4.3.3 Nonlocal Simulation Results

As expected, the nonlocal model was able to capture the viscous fingering phenomena without requiring any adjustment. Initial disturbance of the interface grows upon injection and quickly forms fingers that open up channels through the second phase. For this simulation, we have chosen the following parameters. $\Delta t = 0.03125$ ms, $\Delta p = 1000$ Pa , $R = 3.0$, $\epsilon = 3.5$ grid spacings. We are also using a linear weight function as presented in section 3.2.3.2.

The simulation results from the left-injection simulation and the ones provided below from a central injection clearly show the three well known characteristics of viscous fingering. These characteristic are know as shielding, splitting and spreading and are typically used even by experimental works to qualitatively discuss viscous fingering [38].

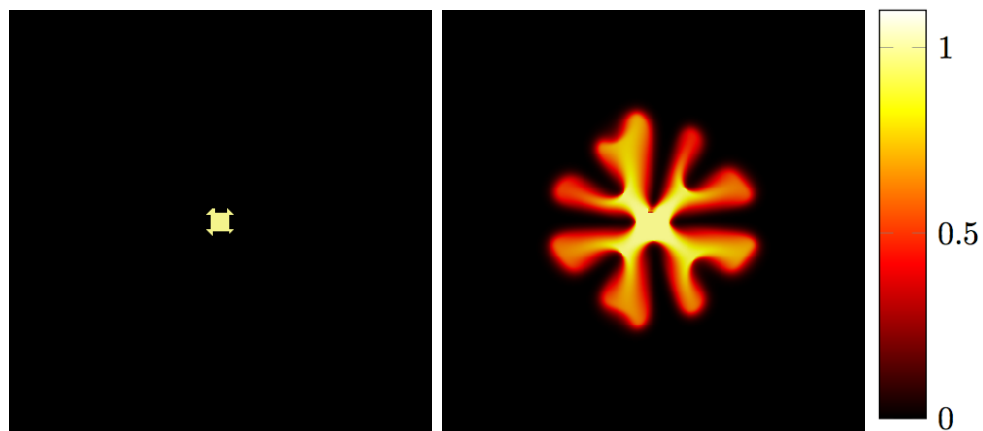


(a) Screen shot taken at time=0 (b) After only 3 ms the formation to show the initial disturbance of the fingers have already taken place at the interface in order to shape. The interactions between adjacent fingers is promoting further disorder

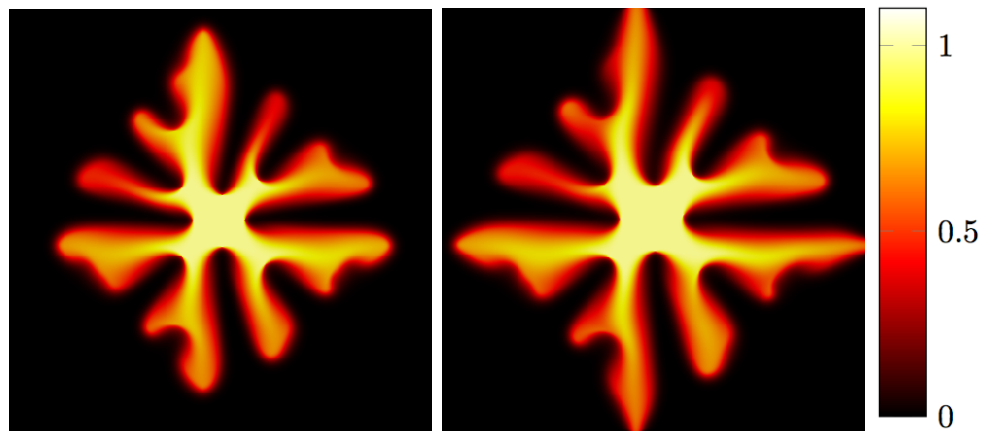


(c) 6.3 ms into the injection and (d) At 8 ms, the splitting and the pressure build up at the finger merging of fingers can be clearly seen the tips is causing the elongation of the fingers

Figure 3.6: Above screen shots follow the evolution of fingers from the injection moment for 8 ms for a two phase flow with an initially disturbed interface.



(a) Initial snapshot shows the injection point which is placed at the mid point of the domain
 (b) Formation of viscous fingers is clearly apparent in the snapshots taken at initial stages of injection



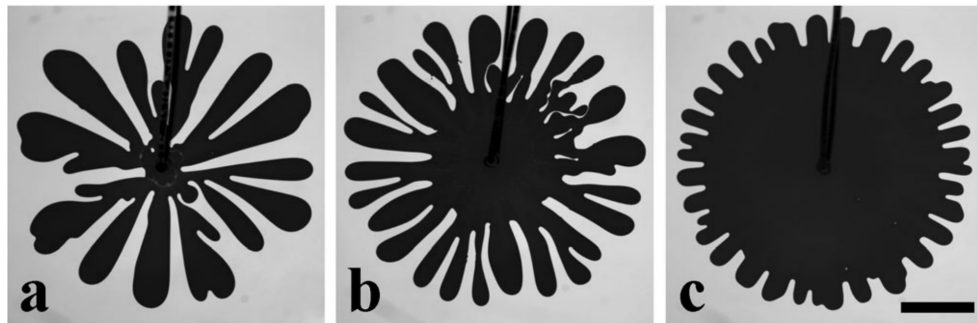
(c) Note the simultaneous growth of the central inclusion
 (d) Symmetry of the domain has stopped tangential interaction of fingers

Figure 3.7: Central injection was done under pressure difference $\Delta p = 1500$ Pa, $R = 3.0$, $\Delta t = 0.00625$ ms. Screen shots are taken at 3 ms intervals.

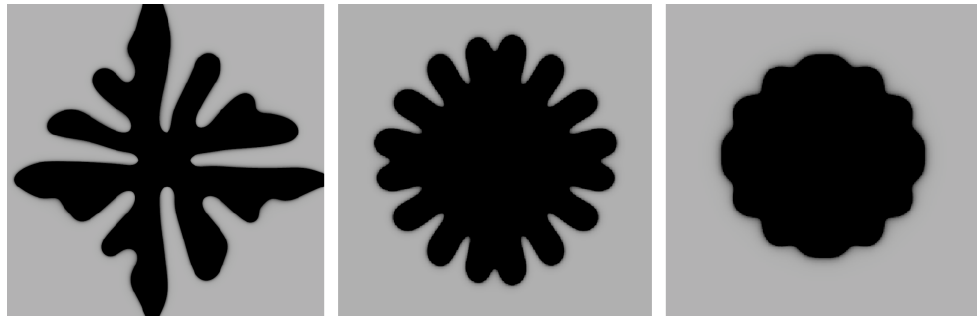
An interesting feature of experimental results are the sharpening of finger tips as the viscosity ratio is increased. The proposed model has proven to be capable of capturing this phenomena. This result has been reproduced in the proposed model by increasing the R value from a moderate 2 to a high value of 7. Provided experimental results are for central injection of glycerol-water mixture into silicone oil. The numerical results are not done at local or nonlocal limit and so the results should only be compared qualitatively. The experiments are done with different pressure difference and viscosity ratios but both results show two uniquely similar characteristics for the fingers. Firstly, as mentioned, the increase in viscosity ratio has resulted in sharper and longer fingers. Secondly, as the viscosity ratio is increased, the central injection area of the displacing fluid finds it increasingly harder to grow. Instead, the fingers now carry all the displacing fluid inside the domain. This characteristic can significantly reduce the ability of the displacing phase to move the more viscous fluid out of the domain.

3.4.4 Dispersion vs. Mixing Degree

For a given numerical discretization, one would expect to see more dispersion as the horizon size is increased. This is due to the nature of a nonlocal model and the fact that with a larger horizon the particles are allowed to have direct contact over a wider area. Therefore, the mixing interface should get wider as m is increased. To capture this idea mathematically, we have decided to calculate the mixing degree of the two phase flow based on the model



(a) Experimental results as presented by [10]



(b) Predictions of the proposed nonlocal model

Figure 3.8: Comparison of the experimental results and the prediction of the proposed nonlocal model. Plots are showing the effect of increasing the viscosity ratios on the shape of and size of the fingers

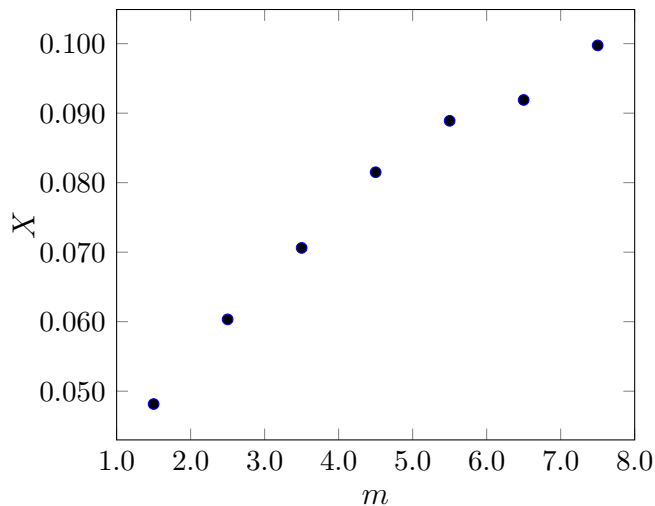


Figure 3.9: Illustration of the mixing degree based on the calculation of the variance of the concentration field

presented by [42]. The mixing degree X is given by $X(t) = 1 - \sigma^2(t)/\sigma_{max}^2$. Where σ is the variance of the concentration field and σ_{max} is the maximum value achieved during the simulation. Figure 3.9 shows the increase in the degree of mixing as the nonlocality is increased. This is a significant result and as far as we know, the first numerical attempt to include the direct effect of dispersion in a viscous fingering simulation.

In the current study, we have presented a nonlocal model capable of studying the effect of dispersion on the characteristics of viscous fingers in two phase miscible flow. We have shown that dispersion can be controlled through the size of horizon chosen for the domain. We, however, skipped over the importance of the nonlocal weight function, ω . ω is in fact a physical representation of the nature of the porous media. Together with the chosen horizon size, it can significantly adjust the dispersion level inside a domain. As a result,

we have chosen to dedicate the next chapter to present a standard procedure to extract the correct shape for ω in a domain. Having said that, it is also important to mention that ω only affects the result at the nonlocal limit and does not change the final result when the local limit is considered.

3.5 Conclusion

In this chapter, a nonlocal advection-diffusion model for 2-phase miscible flow in porous media was introduced. The convergence of this model to the classical advection-diffusion result was proven for the case of a vanishing horizon and the capabilities of the model in capturing the effect of dispersion was explored. Here, the discussion about the appropriate size and shape for the nonlocal weight function, ω , was left untouched. The different choices of ω will not affect the local limit but could be a significant factor if the nonlocal limit is being studied. This point will be investigated in more detail in the upcoming chapters.

Chapter 4

Nonlocal Formulation for Heat Transfer in Nanofluids

4.1 Introduction

Nanofluids are suspensions made up of nano-sized¹ fibers or particles in a fluid. In most nanofluids, the particles take up less than 5% of the volume of the suspension. Yet, studies suggest that the addition of nanoparticles can result in a significant improvement in the thermal properties of the suspension [29, 59]. In some cases, nanofluids have been reported to reach up to 3 times higher conductivities compared to their base fluid [17].

Maxwell [56] is known as the first scientist to study the thermal properties of suspensions. Maxwell's work suggests a direct relationship between thermal conductivity of suspensions and the volumetric fraction of particles, also known as particle loading. His work, however, focused only on suspensions made up of spherical particles. To address this shortcoming, Hamilton and Crosser (HC) [37] presented a modified model to predict the heat transfer coefficients of suspensions with nonspherical particles. Both models can offer a close estimate for the heat transfer enhancements of suspensions with

¹i.e., characteristic length on the order of 10^{-9} m

mili- and micro-sized particles. However, they fail to predict the anomalous enhancement of nanofluids [106]. These continuum formulations consider the particle size and loading while ignoring any changes to the atomic structure of the base fluid. They also consider the suspensions to be static, composite structures, an assumption which many believe adds to the inaccuracy of the calculations that use continuum models [76].

Since Maxwell's pioneering work, numerous theoretical and experimental research has been conducted on nanofluids. The study by Choi and Eastman [17] found a strong dependence between the thermal conductivity of a suspension and its particles' shape and percentage loading. The authors reported an enhancement of 200% when copper nanoparticles were added to water, forming a suspension with 20% copper loading. The result of this study sparked interest across multiple scientific fields. Wang et al. provide a thorough review of some of the main experimental work done on nanofluids [100, 106]. A majority of the literature reports an increase in the thermal conductivity for nanofluids with increased particle loading and increased average diameter. Nevertheless, the results are not always in agreement. As an example, the following studies were all conducted using a suspension of alumina and water. Masuda et al. [55] reported a 33% enhancement for a suspension with average particle diameter of 13 nm and volumetric fraction of 4.3%. A later study by Timofeeva et al. [100] used a suspension with an average particle diameter of 11 nm and particle loading of 5%. However, they reported a much more moderate 7% enhancement. Wang et al. [107] also used

a suspension with 5% particle loading but contained larger particles with an average diameter of 28 nm. They reported an enhancement of 15%. Eastman et al. used even larger alumina particles with an average diameter of 33 nm. They report the thermal conductivity enhancement to be closer to 25%. Experimental work on nanofluids often fails to reproduce previously reported results due to the complexities involved in testing. Furthermore, nanoparticles' average diameter can vary from batch-to-batch, and nanofluid suspensions are typically far from stable (i.e. the suspension's thermal conductivity can drastically change due to particle aggregation and sedimentation; therefore special effort is needed to stop such phenomena from happening).

More recently, molecular dynamics (MD) approaches have offered an easily reproducible method for the study of nanofluids. These models typically calculate the thermal conductivity using the Green-Kubo method. Apart from being able to investigate particle size and volumetric fraction, MD models have the capability to explore more complex aspects of a suspension including the fluid layering [50, 52, 97] and the changes in the movement of base fluid after the introduction of particles [76]. It's important to note that while MD models are good modeling tools, they are typically only accurate when used to model suspensions of particles or fibers in a base liquid with a simple atomic structure. Liquid argon is an example of a base fluid commonly used in MD studies. As a result, MD models are typically viewed as strong qualitative tools for the study of nanofluids. Sarkar et al. [76] used an equilibrium MD model to study the effect of copper loading using liquid argon as the base fluid. They report

a 20% enhancement in thermal conductivity when 1% volumetric fraction of copper was added to the base fluid. Their model shows a continued growth in conductivity to a significant 52% enhancement for 8% Cu loading. This is almost double the prediction of HC formulation for the same particle loading of Cu-Ar nanofluids. The authors attribute most of this enhancement to the increased movement of liquid atoms in the presence of nanoparticles. However, this study did not explore the effect of fluid layering around nanoparticles. In another study on Cu-Ar done by Ling [50] the researchers used the density measurements of the base fluid to show that a dense layer of argon atoms form around copper nanoparticles. Additionally, they showed that the same argon atoms remained near the copper nanoparticles throughout the simulation. This study reports 21% enhancement for 2% Cu loading. Which is almost 10% lower than the estimate of [76]. Ling attributed the improved conductivity seen in their model to the layering of Ar around Cu particles and, as a result, concluded that conductivity must be dependent on the size of the particles as a larger particle can house more Ar atoms on its surface. Additional studies have so far investigated the effect of other factors such as particles' shape and size [22] and aggregation and clustering of nanoparticles [43]. Jabbari et al. [40] provide a thorough review of the most recent MD studies on nanofluids.

MD studies of nanofluids are typically in better agreement to observations than other numerical and theoretical methods used. However, running MD models is a computationally expensive task. As a result, MD studies are usually done on domains that only include a single nanofluid and its sur-

rounding base fluid atoms. Such a domain can be a great tool for studying the interaction between nanoparticles and the base fluids. However, this small domain limits the ability to study the more complex features of a suspensions, including the interaction of the particles with each other and with the boundaries of the domain. Nonlocal (NL) models such as peridynamic [86] theory can be thought of as a natural up-scaling solution for MD models [81]. NL models could be used to potentially reduce the computational expense while providing a consistent homogenized model of the suspensions. In a similar fashion to MD models, nonlocal models evaluate the overall force balance on each particle through the summation of the interactions from every other particle in a nonlocal subdomain of interest. Peridynamics was first introduced and used by Silling to model elasticity and material failure in solid mechanics. Bobaru et al. extended this work to the study of transient heat conduction [11]. Seleson and colleagues [81] argued that peridynamic and in general nonlocal models have similar computational structures to MD models and showed the extent to which MD results can be recovered when NL models are used to perform the upscaling procedure.

This chapter introduces a NL model for simulating heat conduction in nanofluids. Here, we specifically focus on the computation of the nonlocal kernel and demonstrate a systematic method for this calculation using an Cu-Ar nanofluid.

4.2 Nonlocal Diffusion Model

MD models are typically run on small domains with periodic boundary conditions. It is reasonable to assume that central heating problems in such domains do not generate significant convective flows. Therefore, diffusive heat transfer can be taken as the dominating heat transfer mechanism in MD simulations. With this assumption, and inspired by the works of Bobaru et al. [12], let us represent the proposed nonlocal model for diffusive heat transfer as given by (4.1).

$$0 = \rho c \frac{\partial T}{\partial t} - 2k \int_{\mathcal{H}_\epsilon} \gamma \omega(\|\boldsymbol{\xi}\|) (T(\mathbf{x} + \boldsymbol{\xi}) - T(\mathbf{x})) \frac{1}{\|\boldsymbol{\xi}\|^2} d\boldsymbol{\xi} \quad (4.1)$$

In this equation, ρ is density, c is the heat capacity at constant pressure, T is temperature, t is time, and k is the thermal conductivity. \mathcal{H}_ϵ is the nonlocal horizon, which dictates the radius ϵ of interaction for every point \mathbf{x} in the domain. $\boldsymbol{\xi}$ is the position vector of another point within \mathbf{x} 's horizon as shown in figure 4.1. Finally, ω is the nonlocal kernel or weight function. The nonlocal kernel used here determines the influence of all the particles in the horizon on \mathbf{x} . The nature of the nonlocal kernel will be discussed in detail in this chapter. γ is an appropriate scaling function for the nonlocal model and its relation to other parameters including ω will also be discussed.

Nonlocal models are enhanced with mathematical properties to model the physical nature of a given domain more generally than their classical counterparts. They can recover the classical solution through the δ -convergence

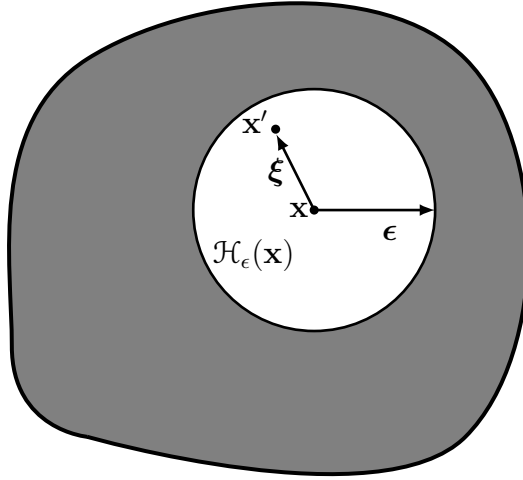


Figure 4.1: Point \mathbf{x} and its horizon shown in white. $\boldsymbol{\xi}$ is the vector connecting \mathbf{x} to any other point in the horizon and ϵ is the radius of the horizon.

method. In this convergence, the size of the horizon is reduced while more nodes are introduced into the domain at a faster rate and until convergence is observed. This convergence can be proven by using a Taylor expansion of the temperature about $\boldsymbol{\xi} = \mathbf{0}$,

$$T(\mathbf{x} + \boldsymbol{\xi}) = T(\mathbf{x}) + \frac{\partial T}{\partial x_j}(\mathbf{x})\xi_j + \mathcal{O}(|\boldsymbol{\xi}|^2). \quad (4.2)$$

Plugging 4.2 back into 4.1, we have

$$\begin{aligned}
& \lim_{\epsilon \rightarrow 0} 2k \int_{\mathcal{H}_\epsilon} \gamma \frac{\omega(\|\boldsymbol{\xi}\|)}{\|\boldsymbol{\xi}\|^2} (T(\mathbf{x} + \boldsymbol{\xi}) - T(\mathbf{x})) d\boldsymbol{\xi} = \\
&= \lim_{\epsilon \rightarrow 0} 2k\gamma \int_{\mathcal{H}_\epsilon} \frac{\omega(\|\boldsymbol{\xi}\|)}{\|\boldsymbol{\xi}\|^2} (T(\mathbf{x} + \boldsymbol{\xi}) - T(\mathbf{x})) d\boldsymbol{\xi}, \\
&= \lim_{\epsilon \rightarrow 0} 2k\gamma \int_{\mathcal{H}_\epsilon} \frac{\omega(\|\boldsymbol{\xi}\|)}{\|\boldsymbol{\xi}\|^2} \left(\frac{\partial T}{\partial x_i} \xi_i + \frac{1}{2} \frac{\partial^2 T}{\partial x_i \partial x_j} \xi_i \xi_j + \mathcal{O}(\|\boldsymbol{\xi}^3\|) \right) d\boldsymbol{\xi}, \\
&= \lim_{\epsilon \rightarrow 0} 2k\gamma \int_{\mathcal{H}_\epsilon} \frac{\omega(\|\boldsymbol{\xi}\|)}{\|\boldsymbol{\xi}\|^2} \left(\frac{1}{2} \frac{\partial^2 T}{\partial x_i \partial x_j} \xi_i \xi_j + \mathcal{O}(\|\boldsymbol{\xi}^3\|) \right) d\boldsymbol{\xi}, \\
&= \lim_{\epsilon \rightarrow 0} 2k\gamma \int_{\mathcal{H}_\epsilon} \frac{\omega(\|\boldsymbol{\xi}\|)}{\|\boldsymbol{\xi}\|^2} \left(\frac{1}{2} \frac{\partial^2 T}{\partial x_i \partial x_j} \xi_i \xi_j \right) d\boldsymbol{\xi} + \mathcal{O}(\epsilon), \\
&= \lim_{\epsilon \rightarrow 0} 2k\gamma \frac{1}{2} \frac{\partial^2 T}{\partial x_i \partial x_j} \int_{\mathcal{H}} \frac{\omega(\|\boldsymbol{\xi}\|)}{\|\boldsymbol{\xi}\|^2} (\xi_i \xi_j) d\boldsymbol{\xi} + \mathcal{O}(\epsilon), \\
&= \lim_{\epsilon \rightarrow 0} k \frac{\partial^2 T}{\partial x_i \partial x_j} \delta_{ij} + \mathcal{O}(\epsilon), \\
&= \lim_{\epsilon \rightarrow 0} k \frac{\partial^2 T}{\partial x_i \partial x_i} + \mathcal{O}(\epsilon), \\
&= k \nabla^2 T.
\end{aligned}$$

Therefore taking the limit on all the terms in equation (4.1) results in

$$0 = \rho c \frac{\partial T}{\partial t} - k \nabla^2 T. \quad (4.3)$$

Here $\omega = \omega(\|\boldsymbol{\xi}\|) = \omega_s(\|\boldsymbol{\xi}\|)$ is assumed to be spherically symmetrical, which implies that

$$\begin{aligned}
\int_{\mathcal{H}} \omega_s(\|\boldsymbol{\xi}\|) \frac{\xi_k \xi_j}{\|\boldsymbol{\xi}\|^2} dV_{\boldsymbol{\xi}} &= \delta_{kj} \int_{\mathcal{H}} \omega_s(\|\boldsymbol{\xi}\|) \frac{\xi_1^2}{\|\boldsymbol{\xi}\|^2} d\boldsymbol{\xi}, \\
&= \delta_{kj} \int_0^{2\pi} \int_0^\pi \int_0^\epsilon \omega_s(\|\boldsymbol{\xi}\|) \frac{\xi_1^2}{\xi^2} \xi^2 \sin\theta d\xi d\theta d\phi, \\
&= \delta_{kj} \frac{m_1}{3},
\end{aligned}$$

with

$$m_1 = \int_{\mathcal{H}} \frac{\omega(\|\boldsymbol{\xi}\|)}{\|\boldsymbol{\xi}\|^2} \xi_k \xi_j d\boldsymbol{\xi},$$

with the spherical coordinates, $\xi_1 = |\boldsymbol{\xi}| \sin\theta \cos\phi$, $\xi_2 = |\boldsymbol{\xi}| \sin\theta \sin\phi$, and $\xi_3 = |\boldsymbol{\xi}| \cos\theta$ and

$$\gamma = \frac{3}{m_1}.$$

4.3 Proposed Method for Kernel Extraction

The kernel of a nonlocal model is widely understood as the representation of the average interaction between material points or particles inside the domain. For the current investigation, of interest are the interactions that take part in the diffusion heat transfer processes. Interatomic forces are the bridges used for the transfer of kinetic energy between the particles. A physically meaningful choice for the nonlocal kernel in heat transfer problems, must be calculated based on the van der Waals forces between the constituent atoms. In this study, an MD model has been used to calculate the average force exerted on a randomly chosen particle in the domain. More specifically, one area of investigation is how this force changes with radius. The dependence of force as a function of radius is what will be used to calculate the appropriate kernel for the chosen domain.

The MD model used in this analysis is run using LAMMPS [98] and is setup to use a 6-12 Lennard-Jones (LJ) potential for argon and copper.

Lennard-Jones potential is an empirical model that was originally proposed by Jones in 1925 to model the cohesive energy of crystals of noble gases [108]. The 6-12 LJ potential is one of the most widely used intermolecular potentials where

$$\nu_{LJ}(r) = 4\epsilon \left(\left[\frac{\sigma}{r} \right]^6 - \left[\frac{\sigma}{r} \right]^{12} \right).$$

Here ϵ stands for the depth of the attractive well, r is the interatomic separation and σ is the interparticle distance where the potential changes sign. σ is also often understood as the radius of one of the atoms. The LJ parameters used for Ar and Cu are $\sigma_{Cu} = 2.3377e - 10$ m, $\epsilon_{Cu} = 65.625e - 21$ J, $\sigma_{Ar} = 3.405e - 10$ m and $\epsilon_{Ar} = 1.67e - 21$ J. The domain used for the simulations is a box region with ΔL and $\Delta H = 5.2e - 7$ m. Depending on the problem, a heat source is added to a chosen section of this domain, and the response of the system is monitored. Using this domain, the MD simulations are run on both pure argon and 0.9-7.5% Cu-Ar nanofluid with time step of 1 femtosecond and for 2 million time steps. The proposed method for kernel calculation requires the position file output of the LAMMPS simulation. The position of individual particles is recorded in this file at every 1000 time steps. Using the position output files, the following steps are taken to calculate the force vs radius values.

First, the domain is split into spherical shells around a chosen particle. Iterating over neighboring particles, the LJ potential exerted on the central particle from every shell is calculated. Figure 4.2 shows how the domain is split into shells around a randomly selected particle. This calculation is repeated

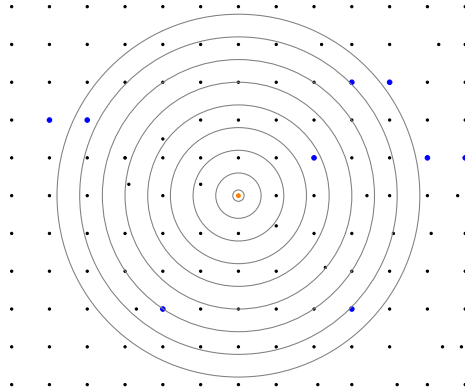


Figure 4.2: Domain was split into spherical shells to calculate the average forces experienced from each discretized ring. Here, larger blue dots represent the nanoparticles and small black dots are argon atoms.

for every single particle inside the domain and the results of all LJ potential calculations are averaged to give the final plot of the averaged LJ potential for every recorded time step. Apart from averaging the results on all particles, the LJ-potential over time for the 2 million time steps taken during this simulation has been averaged. To ensure the accuracy of this method, the thickness of the shells is reduced in increments and the calculation is repeated on thinner shells. By doing so, the calculated potential is shown to converge to a curve that closely follows the analytical LJ potential for pure argon. The results of this convergence study are shown on figure 4.3.

The analytical LJ-potential curve is based a continuum idealization. However, in reality, the atoms are most likely to arrange into an ordered lattice structure. In this lattice, the probability of finding atoms in a shell significantly drops the further away the shells are from the equilibrium distance for constitutive atoms. Figure 4.4 clearly demonstrates the drop in atomic dis-

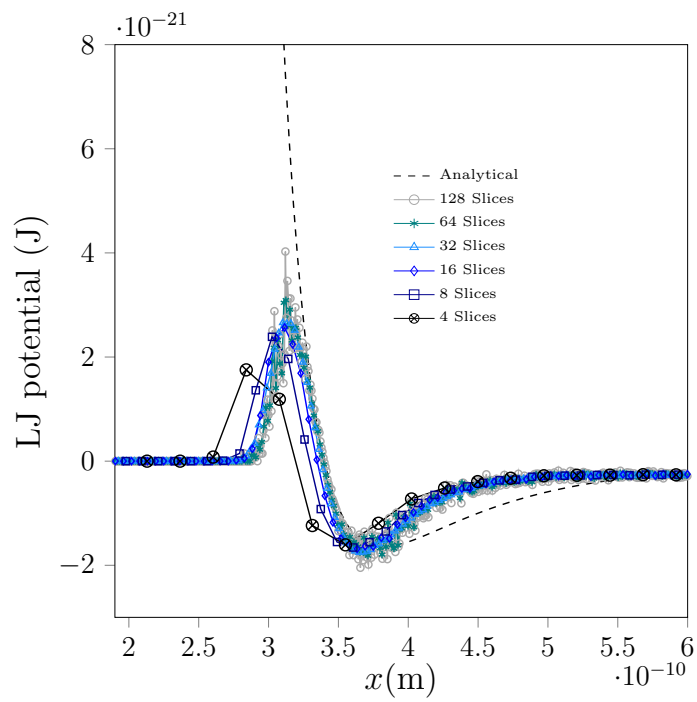


Figure 4.3: As the number of slices is increased, the calculated LJ potential for pure argon is converging to the analytical LJ potential shown by the dashed line

tribution density before and after the equilibrium distance. This non-uniform atomic distribution density is the main reason for the deviation between the analytical and the calculated LJ potentials. The analytical LJ potential curve also predicts that the potential must grow large as the particles pack closer together than the equilibrium distance, r . In reality however, the inner shells always stay empty as this large force stops any atoms from entering the most central shells. This fact is captured by the calculated LJ potential and the force from the nearest shells are calculated to be zero.

Using the above procedure, the Leonard-Jones potentials were calculated for pure liquid argon and Cu-Ar nanofluids with nanoparticle loading

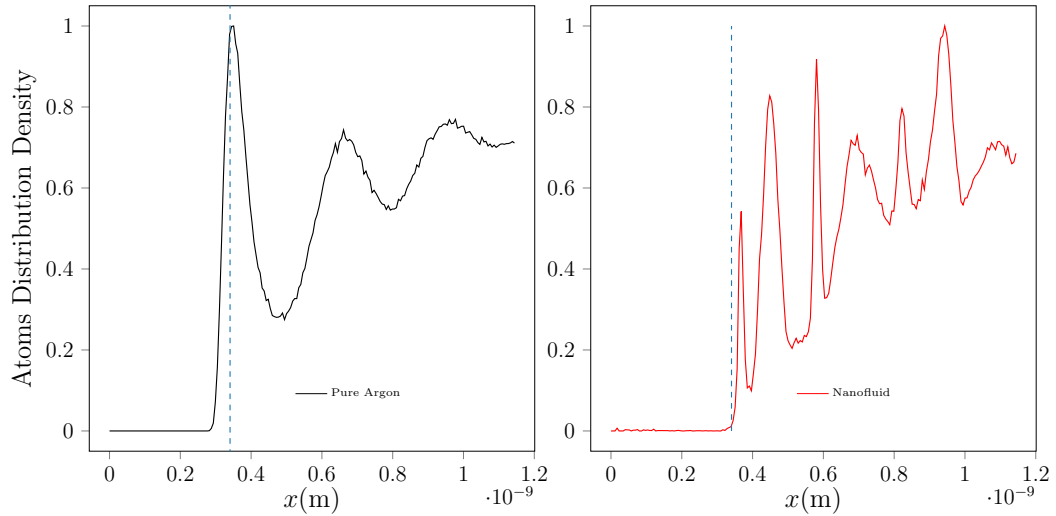


Figure 4.4: The plots show the radial distribution of atoms about a central particle in both pure argon and 3.8% Cu-Ar nanofluid. Blue dashed lines represent the equilibrium distance for liquid argon. As expected, the introduction of nanoparticles has forced the argon atoms to rearrange into a new structure with larger spacings between atoms

between 0.9 and 7.5%. The calculated potentials were then differentiated over distance to get the force as a function of radius. This force, whether attractive or repulsive, transfers kinetic energy between particles. Thus, the shape of the nonlocal kernel should directly match the absolute of the calculated force vs radius curve. The extracted shape of the nonlocal kernel for both pure argon and a Cu-Ar nanofluid with 3.8% Cu loading is shown in figure 4.5. If we assume that the time averaged velocity of every particle in the domain is equal, then the proposed method can be closely linked to the infamous Green-Kubo method [46] which has been widely used in previous heat conductivity calculations of nanofluids.

Currently, the theory proposed by Keblinski et al. [46] is known to offer the best summary about the known aspects of the nature of heat transfer in nano-fluids. The authors proposed, the ballistic nature of heat transfer in nanoparticles, ordered layering of fluid atoms around nano particles, thermal energy transfer due to Brownian motion of nanoparticles, and the clustering of highly conductive nanoparticles as the potential mechanisms responsible for the increased heat conductivity of nanofluids. The last three points of the proposed theory are related to the motion of particles. These mechanisms are automatically captured in the proposed method for kernel calculation. The first point regarding the ballistic nature of heat transfer through nano particles cannot be understood based on the position of particles alone. What this mechanism essentially means is that the bottleneck of the heat transfer mechanism in nanofluids is the rate of heat transfer through the base fluid

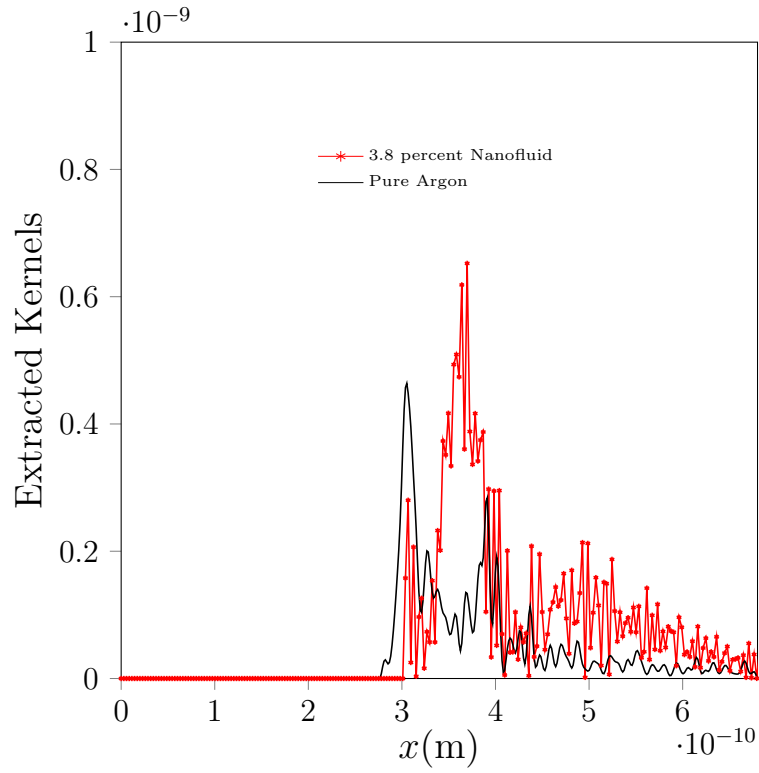


Figure 4.5: Computationally up-scaled kernels for pure liquid argon and 3.8 % Cu-Ar nanofluid

and rate of heat transfer from the base fluid to the nanoparticles and their surrounding solid-like structure. Figure 4.6 shows the calculated components of LJ potential for Ar-Ar, Cu-Ar and Cu-Cu interactions.

In order to stay consistent with Keblinski's viewpoint, argon atoms must be 100% involved in the heat transfer process and the contributions from the copper atoms can be completely ignored (0% weight) without any loss of information. By applying this weight, any resistance to heat transfer from copper particles will be eliminated as the heat is assumed to instantaneously

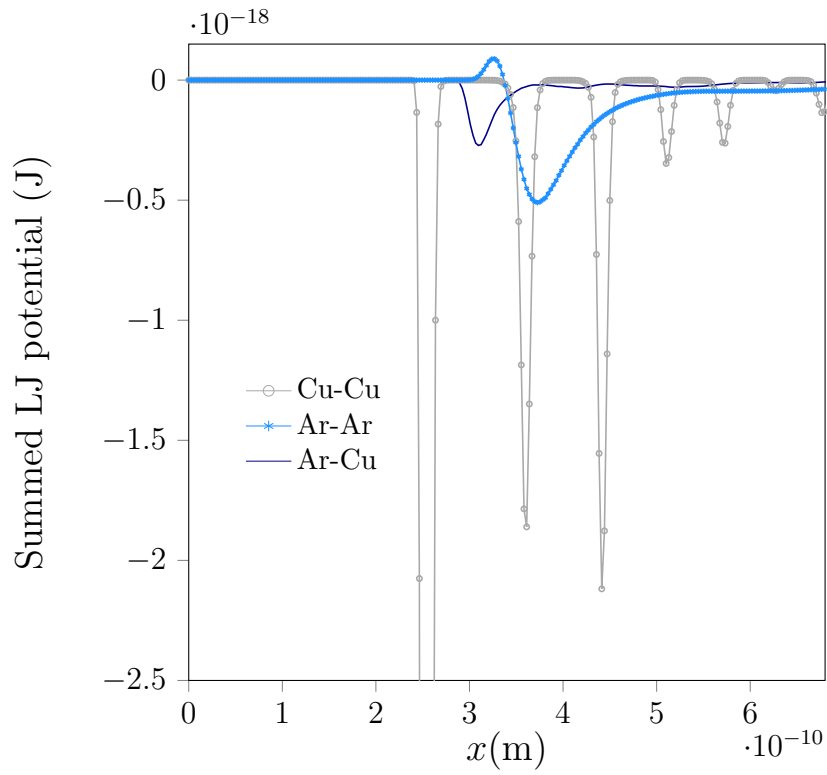


Figure 4.6: Components of LJ potential from interactions between Cu and Ar particles

travel through the copper nanoparticles. Following the same logic, the Cu-Ar interactions should be given a 50% weight. As will be discussed in the following chapters, the above weights have been found to be sufficiently accurate as the calculated conductivities are shown to closely match the literature. However, future work must take a closer look at the Cu-Ar interactions in order to confirm the validity of the chosen weight.

4.4 Discretization

To solve this nonlocal model, the domain has been split into equally spaced nodes with spacing of Δx . The discretized version of this model is presented here.

$$0 = \rho c \frac{T^{n+1}(\mathbf{x}_i) - T^n(\mathbf{x}_i)}{\Delta t} - 2k \sum_j \gamma \frac{\omega(\|\boldsymbol{\xi}\|)}{\|\boldsymbol{\xi}\|^2} (T^{n+1}(\mathbf{x}_j) - T^{n+1}(\mathbf{x}_i)) A_j \quad (4.4)$$

Above A_j can be thought of as Δx^2 for 2-dimensional case. Here $\mathbf{x}_j := \mathbf{x}_i + \boldsymbol{\xi}$ where j stands for a neighboring node and x_i is the spatial position of the node of interest. In this discretized model, the local limit, which recovers the solution for classical equations of diffusive heat transfer, is achieved by increasing the number of neighbors while increasing the total number of nodes at a faster rate. This ensures that the overall horizon size approaches zero. Another point of convergence of a nonlocal model is the nonlocal limit. This limit is achieved by holding the horizon size constant while increasing the number of nodes in steps. Given the correct choice of kernel, the nonlocal model is expected to more accurately simulate the domains that have features ignored by the assumptions made in the classical continuum models.

4.5 Results and Discussion

To confirm the validity of the method, the thermal conductivity calculation for nanofluids was carried out with volumetric nanoparticle loading between 0.9 and 7.5%. Regardless of the choice of the nonlocal kernel, the integral of the kernel must be equal to the average thermal conductivity of

the fluid. The proposed method for kernel extraction will compute the correct shape of the kernel, which affects dynamic problems. It can also find the ratio between the thermal conductivity of two fluids based on the two calculated kernels. However, to find the absolute value of the thermal conductivity of the system, we have to first calibrate the extracted kernel for the base fluid and one nanofluid suspension in isolation. Therefore, before using the upscaled kernel to calculate thermal conductivities of nanofluid mixtures, the kernel was calibrated using an established solution [76]. For this calibration, the integral of the kernel for pure argon was constrained to $0.127 \text{ Wm}^{-1}\text{K}^{-1}$ and the integral of the kernel for 1.8% nanoparticle to $0.163 \text{ Wm}^{-1}\text{K}^{-1}$. This nonlocal model was then used to predict the conductivity of all other nanofluids up to a copper loading of 7.5%. These predictions are presented in figure 4.7. The predictions of the nonlocal model are in close agreement with those of an MD model using the Green-Kubo method [76]. The gray line shows the prediction of Hamilton-Crosser model. This continuum model significantly under-predicts all nanofluid thermal conductivities compared to both the MD and the NL model using the computationally up-scaled kernel

Thus far, we have shown that the proposed method for kernel extraction can be used to predict the average conductivity of nanofluids, and the predictions closely match that of an equilibrium MD model using the Green-Kubo method. In the following sections, the upscaled kernel in the nonlocal model will be used to solve problems with much larger domains than are tractable with MD methods. Here, we will use a highly refined solution of (4.4) as the

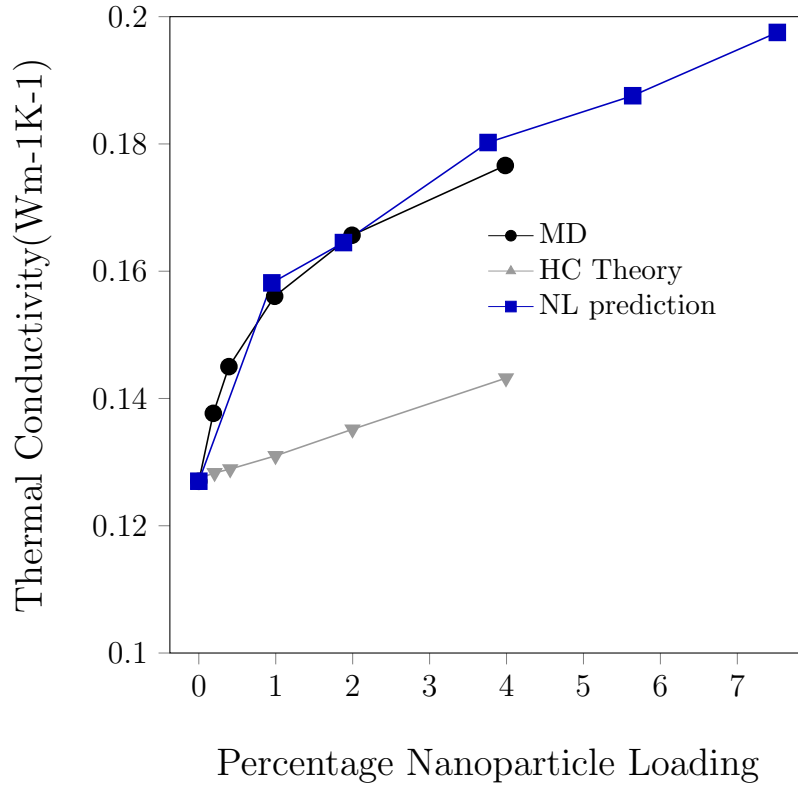


Figure 4.7: Comparison of thermal conductivity calculations between MD, NL and HC models. The results of the predictions from the proposed nonlocal model and the MD model are in close agreement. The continuum HC model under-predicts the thermal conductivity for all nanofluids

reference nonlocal solution. The solution of a finite difference discretization will also be used as the reference local solution and a comparison between the local and nonlocal models will be provided. For the following nonlocal models, the horizon is truncated at a distance where the extracted values for the upscaled kernel are zero. This will ensure unnecessary calculations are not conducted over neighboring particles that do not influence the heat transfer and therefore results in the fastest simulation time.

4.5.1 Steady-State Heat Transfer

The steady-state condition can be modeled both using the steady-state equations (4.5) or by allowing the transient solution (4.1) to reach equilibrium at long times. Following the derivation presented for (4.1), the discretized form of the proposed NL steady state diffusion can be written as

$$q = -k \sum_j \gamma \omega(\|\boldsymbol{\xi}\|) (T(\mathbf{x}_j) - T(\mathbf{x}_i)) \frac{\xi_j}{\|\boldsymbol{\xi}\|^2} A_j. \quad (4.5)$$

4.5.1.1 Parameterization

The following simulations are run on a box region, with $\Delta L = \Delta H = 5.2e - 7$ m where L and H are the length and the height of the domain respectively. The nanoparticle loading is 3.8%, and the thermal conductivity, $k = 0.180$ Wm⁻¹K⁻¹. The time step chosen for these simulations is $\Delta t = 1e - 12$ s.

4.5.1.2 Boundary Conditions

Periodic boundary conditions are used for all four edges of the domain. A constant heat flux source and a sink are added 1/3 of the way from the left and right boundaries respectively. In an NL model, the constant heat flux boundary condition can be applied by enforcing the equivalent temperature gradient on all nodes through the boundary layer thickness of one horizon. The periodic boundary condition is enforced using the technique explained in 3.4. In a periodic boundary the flow exiting the top or the bottom edge must

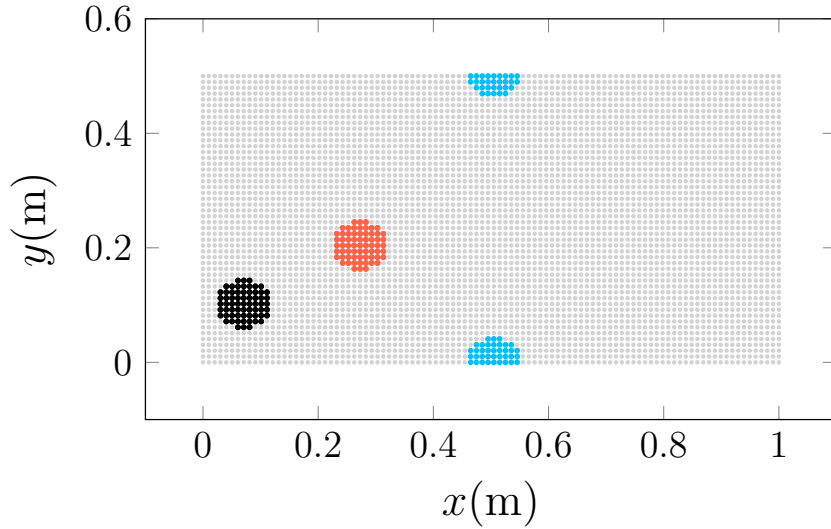


Figure 4.8: Illustration of how horizon of a point can be split at the edges of the domain

re-enter the domain through the opposite edge. To allow for this to happen, the nodes that are placed within a distance ϵ from the upper or lower edge must at least share a neighbor on the opposite edge of the domain. Figure 4.8 demonstrates this concept by showing the horizon for 3 randomly chosen nodes in the domain. In this setup, a node placed at the bottom edge (here shown in blue) has half of its neighbors on the top boundary of the domain and half at the bottom edge.

4.5.1.3 Choice of the Nonlocal Kernel

There is an analytical solution for the aforementioned domain with a constant flux boundary condition. For this problem, the temperature profile

will take a linear shape with maximum temperature occurring at the heat source and the minimum temperatures at the sink. This is a simple solution that allows the effect of kernel's shape on the final result to be investigated. Two different kernels have been chosen to run the NL simulations. The first kernel is the computationally upscaled kernel for 3.8% Cu-Ar nanofluid given by fig.4.5. The other kernel used is a constant, $y = \frac{k_{3.8}}{\epsilon}$. Here, $k_{3.8}$ is the thermal conductivity of the 3.8% Cu-Ar suspension and ϵ is the problem's characteristic length scale and the size chosen for the horizon.

4.5.1.4 Nonlocal Simulation Results

The result of the nonlocal simulations are presented in figure 4.9. It is shown that as the nonlocal limit is approached, NL models using both kernels, approach the same result. This is an important finding that indicates that for steady-state heat conduction problems, the shape and size of the nonlocal kernel do not affect the result of the simulation. In such cases, simple kernel shapes such as triangular kernels are recommended as they typically reduce the convergence time [11] due to reduced numerical integration inaccuracies.

4.5.2 Transient Heat transfer

Next, the effect of kernel selection on the outcome of a transient heat transfer simulation will be explored. For this case, the domain is initially at a constant temperature of 90C. The temperature of a vertical strip in the middle of the domain is set to 120C at time, $t = 0$ and the temperature profile

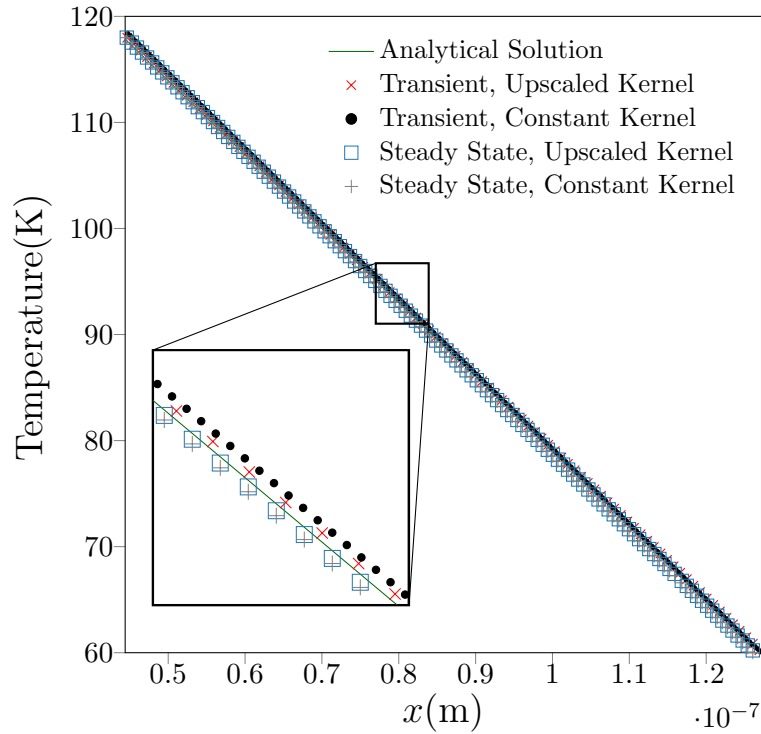


Figure 4.9: Results of simulations for a steady state problem using constant heat flux boundary conditions. Here, it is shown that the results of local and nonlocal models closely match. It is also shown that the choice of nonlocal kernel does not affect the result of the steady state problems

is calculated using both a finite differenced local model and the nonlocal model presented by (4.4).

4.5.2.1 Parameterization

The following simulations are run on two box regions, the first with ΔL and $\Delta H = 1.5e - 8\text{m}$, and the second with ΔL and $\Delta H = 2.86e - 6\text{m}$. The nanoparticle loading is 3.8% and the thermal conductivity, $k = 0.180 \text{ Wm}^{-1}\text{K}^{-1}$. The time step chosen for this part is $\Delta t = 1e - 12\text{s}$, and the simulations

are run for 10,000 time steps.

4.5.2.2 Boundary conditions

Periodic boundary condition is used for all edges. The initial temperature condition chosen for the entire domain is 90C. The temperature for all the nodes in a vertical strip in the middle of the domain and with thickness, 2ϵ is set to 120C at $t = 0$.

4.5.2.3 Choice of the Nonlocal Kernel

For this section, three different kernels have been chosen for the NL simulations. As before, the first kernel is the computationally up-scaled kernel for 3.8% Cu-Ar nanofluid given by fig.4.5. The other two kernels used have the shape of a horizontal line, $y = \frac{k_{3.8}}{\epsilon}$. Here, $k_{3.8}$ is the thermal conductivity of the 3.8% Cu-Ar suspension, and ϵ is the horizon size. For the second kernel, also referred to as the *small kernel*, the horizon size $\epsilon = 6.5e - 10\text{m}$ and for the final or the *large kernel*, $\epsilon = 2e - 9\text{m}$.

4.5.2.4 Nonlocal Simulation Results

Looking at the results of the simulation for the larger domain, the length of the domain is chosen such that the characteristic length scale, $\epsilon \ll \Delta L$. The result of the simulations run on this large domain is shown in figure 4.10. Similar to the steady state problem, all simulations converge to the same nonlocal limit, which closely matches the result from the finite differenced

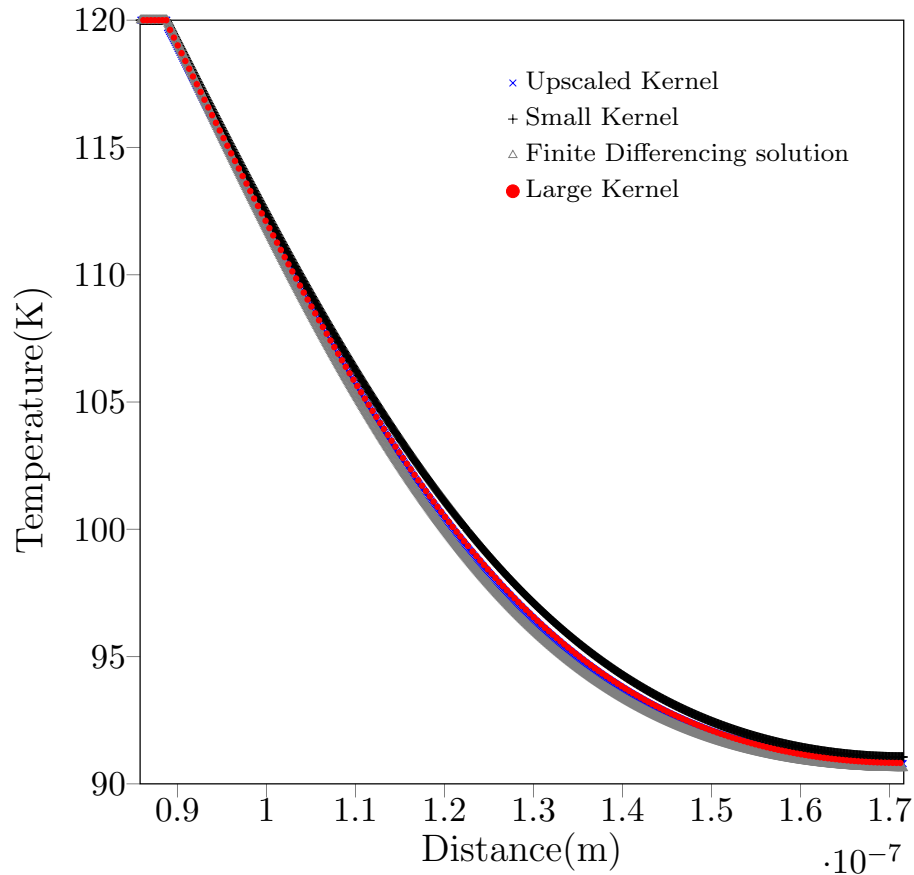


Figure 4.10: Results of the local and nonlocal transient simulations on a domain with constant temperature boundary conditions. The results are shown to converge for the case where $\epsilon \ll \Delta L$

local simulation. This is an expected result. ϵ represents the average size of heterogeneities of the domain and therefore a domain with $\epsilon \ll \Delta L$ can be modeled as a homogenous one. For a homogenous domain, the nonlocal and local solutions should agree. Next, the second domain size chosen for the transient heat diffusion problem above will be investigated. Here, the domain size is much closer to the size of ϵ , and as a result, the homogeneous assumption

for the domain is no longer valid. The result of simulations run on this domain are given by figure 4.11. Contrary to the results from the previous sections, in this case the horizon's size is shown to have a measurable effect on the calculated temperature profile. Here, the size of the kernel is shown to have a more significant effect on the calculated profile compared to its shape. The results also show a deviation between the prediction of the nonlocal solution and the result from the finite differencing model.

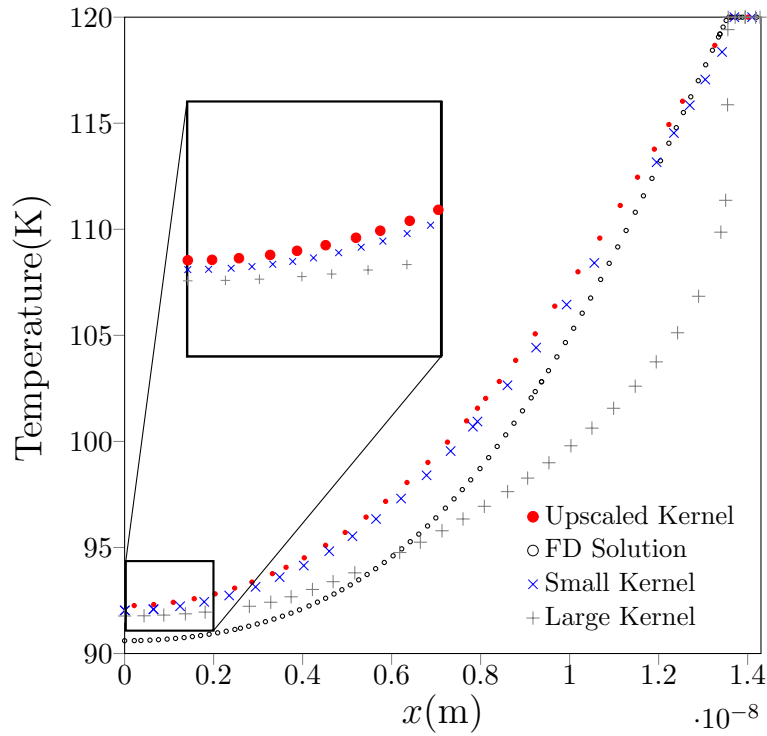


Figure 4.11: Results of simulations for a transient problem. Here the size of the characteristic length scale, ϵ , is chosen to be close to the domain's length L . For this case, the choice of nonlocal kernel is shown to have a significant effect on the calculated temperature profile.

4.6 Conclusion

Nanofluids are suspensions of nano-sized particles in a base fluid. The potential advantages of nanofluids in heat transfer applications have been known for most of the past century. The attempts to model nano-fluids using continuum formulations often fail as a continuous idealization cannot capture the inter-atomic interactions that result in the anomalously high conductivity in nanofluids. Experimental work on nanofluids have also faced challenges due to the complex manufacturing and testing techniques used. More recently, MD models have proven to be the more appropriate tool for modeling nanofluids. However, MD models are computationally expensive to run. Typical domains used in MD models include a single nanoparticle and its surrounding liquid atoms. In this chapter, we proposed a nonlocal model as an upscaled MD formulation. We provided a systematic method for extracting the appropriate nonlocal kernel and investigated the effect of kernel's size and shape on the solution of nonlocal model.

Chapter 5

A Multi-scale Nonlocal Approach for Turbulence Modeling

5.1 Introduction

Turbulence is widely known as one of the oldest unsolved problems in physics. It is characterized by the chaotic behavior of the fluid pressure and velocity fields at high Reynolds numbers. It is also one of the most studied macroscopic features of fluid flows across multiple scientific and engineering disciplines. Blood flow inside arteries, flow through pumps, turbines and around commercial aircraft wing tips are only a few examples of turbulent flows. The widespread presence of such flows in our everyday lives has been fueling the need for the comprehensive understanding of turbulence for most of the past century. Although the effects of turbulence can be experienced through the macroscopic features of a flow, its source lies in the interactions of the fluid particles at the microscopic scale. Small perturbations in the flow, whether formed within the boundary layer or introduced at the inlet, can typically be dampened and completely eliminated by viscous forces. However, if the excess momentum is large enough to overwhelm the viscous forces, a laminar flow will quickly start its transition to an unsteady and disorganized turbulent flow. The chaotic nature of turbulence means that a small change in the ini-

tial conditions can result in a significantly different pressure and velocity fields.

Traditionally, automotive and aerospace industries have used experimental methods such as wind tunnels and scaled down prototypes to visually study the flow behavior as it passes over an object of interest. However, wind tunnels that are large enough to fit real size prototypes are rare to find and hard to maintain. Furthermore, reproducing the exact test conditions inside a tunnel is often hard to achieve. This is especially true if scaled down prototypes are used or a careful study of the interactions with the environment such as the surface of the road is needed. Given the challenges involved with the experimental methods and the rapidly increasing computational power available to researchers, the computational methods have over the years turned into the main tool for the studying turbulence.

Computational methods based on the classical continuum approach such as direct numerical simulation (DNS) can be used to accurately calculate shear stresses and pressure field in all parts of the flow. These fields can in turn be used to calculate force and momentum everywhere. That is given that a fine enough spatial and temporal grid can be employed. An appropriate spatial grid must be fine enough to capture the dissipative and viscous effects that occur at microscopic levels while covering a domain size which is typically many orders of magnitude larger. This simple fact means that even with the wide spread availability of super computers, the computational time required

is still the bottle neck of DNS.

Alternative computational methods such as Reynolds Average Navier-Stokes (RANS) modeling and Large Eddy Simulations (LES) offer their own advantages. In the RANS method, Reynolds decomposition procedure is used to split the flow variables into the mean and the fluctuating parts. The computational requirements for solving RANS equations are typically an order of magnitude less than what is needed to solve the original Navier-Stokes (NS) equations. LES approach also attempts to reduce the computational time needed to solve the original set of NS equations. Here, this task is achieved by ignoring the smallest and yet computationally expensive length scales. But as it is often the case, the more accurate approach for transient modeling, LES, requires significantly higher computational power while still lacking the ability to model small scale phenomena.

More recently, nonlocal models based on fractional calculus have proven to be powerful tools for the study of turbulence [32,72]. Pioneers of the study of turbulence such as Prandtl [68] and Richardson [72] built their work based on the assumption of locality in turbulence interactions. This assumption limits the generalization of the proposed correlations. The underlying assumptions here would only be true if the scale of heterogeneities in the mean flow field is much larger than the mixing length. Fractional models offer a tool to simulate problems with nonlocalities and non-Gaussian statistics. By replacing

the Maxwell-Boltzmann distribution with a general Levy α -stable distribution Epps et al. [32] rigorously derived their fractional Navier-Stokes equations. While the aforementioned model is only valid for open domains, the more recent work by Song and Karniadakis [94] proposed a variable-order fractional differential equation for modeling the Reynolds stresses in wall-bounded domains. The variable fractional differential used in the fractional models offers a solution for modeling nonlocality of the domain. However, it also comes at the cost of significant added computational time. As it was discussed in section 2, a nonlocal model based on the peridynamic formulation can recover the equivalent fractional model with the appropriate choice of kernel. Thus, fractional models can be thought of as a special case for peridynamic based nonlocal models [26]. Such nonlocal models can also recover the local solution. Recent work by [33] have used peridynamic differential operator (PDDO) to simulate fluid flow problems. In this method, the field variables and their spatial derivatives are represented in a nonlocal form. Nguyen et al. [60] used PDDO to simulate flow over a cylindrical object. Their results closely match the results of local simulations run on Ansys Fluent [2]. In this work, a peridynamic based nonlocal model will be introduced which will recover the penalty formulation of the Navier-Stokes equations for an incompressible flow at its local limit. The two-dimensional penalty formulation of Navier-Stokes is given

by the following equations:

$$\begin{aligned}\frac{\partial u}{\partial t} + u \frac{\partial u}{\partial x} + v \frac{\partial u}{\partial y} &= -\frac{1}{\rho_0} \frac{\partial P}{\partial x} + \nu \left[\frac{\partial^2 u}{\partial x^2} + \frac{\partial^2 u}{\partial y^2} \right] + B_x \\ \frac{\partial v}{\partial t} + u \frac{\partial v}{\partial x} + v \frac{\partial v}{\partial y} &= -\frac{1}{\rho_0} \frac{\partial P}{\partial y} + \nu \left[\frac{\partial^2 v}{\partial x^2} + \frac{\partial^2 v}{\partial y^2} \right] + B_y\end{aligned}\quad (5.1)$$

Here, incompressibility is enforced through the penalty parameter, λ by the pseudo-constitutive relation

$$p = -\lambda \left[\frac{\partial u}{\partial x} + \frac{\partial v}{\partial y} \right]. \quad (5.2)$$

Equations 5.1 and 5.2 can be combined to give the following set of equations for the two-dimensional, penalty formulation of Navier Stokes Equations.

$$\frac{\partial u}{\partial t} + u \frac{\partial u}{\partial x} + v \frac{\partial u}{\partial y} = \frac{\lambda}{\rho_0} \left[\frac{\partial^2 u}{\partial x^2} + \frac{\partial^2 v}{\partial x \partial y} \right] + \nu \left[\frac{\partial^2 u}{\partial x^2} + \frac{\partial^2 u}{\partial y^2} \right] \quad (5.3)$$

$$\frac{\partial v}{\partial t} + u \frac{\partial v}{\partial x} + v \frac{\partial v}{\partial y} = \frac{\lambda}{\rho_0} \left[\frac{\partial^2 u}{\partial x \partial y} + \frac{\partial^2 v}{\partial y^2} \right] + \nu \left[\frac{\partial^2 v}{\partial x^2} + \frac{\partial^2 v}{\partial y^2} \right] \quad (5.4)$$

In the following sections, the nonlocal model will be presented in its continuous and discretize form alongside a mathematical proof for its convergence to the local solution. This chapter will also present a comparison between the results of the simulations run using the proposed nonlocal model and other available solutions such as the aforementioned PDDO model.

5.2 Nonlocal Model

Let us start by presenting the nonlocal Navier-Stokes model for two-dimensional flow. As in the previous chapters, the notations and terminologies

employed here have been adapted from peridynamic mechanics. Namely, it is assumed that a point \mathbf{x} interacts with all points $\mathbf{x} + \boldsymbol{\xi}$ within a finite distance parameterized by ϵ called the *horizon*. The set of all points $\mathbf{x} + \boldsymbol{\xi}$ is called the *neighborhood* of \mathbf{x} , and is labeled $\mathcal{H}_\epsilon(\mathbf{x})$. The shape of the horizon is assumed to be spherical in three dimensions and circular in two-dimensions (therefore ϵ is a radius), but other choices are available. Equation 5.5 presents the proposed nonlocal model.

$$\begin{aligned} \frac{\partial u_i(\mathbf{x})}{\partial t} + u_j(\mathbf{x}) \int_{\mathcal{H}_\epsilon} \gamma\omega(\|\boldsymbol{\xi}\|) (u_i(\mathbf{x} + \boldsymbol{\xi}) - u_i(\mathbf{x})) \frac{\xi_j}{\|\boldsymbol{\xi}\|^2} d\boldsymbol{\xi} \\ - \int_{\mathcal{H}_\epsilon} \beta\omega(\|\boldsymbol{\xi}\|) \frac{\xi_i(\boldsymbol{\nu}(\mathbf{x}, \mathbf{x}') + \boldsymbol{\nu}(\mathbf{x}', \mathbf{x}))\xi_j}{\|\boldsymbol{\xi}\|^2} (u_j(\mathbf{x} + \boldsymbol{\xi}) - u_j(\mathbf{x})) d\boldsymbol{\xi} \quad (5.5) \\ - \frac{\lambda}{\rho_0} \int_{\mathcal{H}_\epsilon} \gamma\omega(\|\boldsymbol{\xi}\|) (u_i(\mathbf{x} + \boldsymbol{\xi}) - u_i(\mathbf{x})) \frac{\xi_i}{\|\boldsymbol{\xi}\|^2} d\boldsymbol{\xi} = 0 \end{aligned}$$

Here, i and j are vector components of $\boldsymbol{\xi}$ in two dimensions and as in equation 5.2, the incompressibility is enforced through the use of a penalty parameter such that

$$p = -\lambda \int_{\mathcal{H}_\epsilon} \gamma\omega(\|\boldsymbol{\xi}\|) (u_i(\mathbf{x} + \boldsymbol{\xi}) - u_i(\mathbf{x})) \frac{\xi_i}{\|\boldsymbol{\xi}\|^2} d\boldsymbol{\xi}. \quad (5.6)$$

Here, \mathbf{u} stand for velocity, t is time, $\boldsymbol{\nu}$ is kinematic viscosity, p is pressure and λ is the penalty parameter. ω is called the *influence function* and controls the strength of interactions among the points in the neighborhood. Finally, γ and β are scaling functions whose choice is discussed in the following sections. In 3.2.1, it was assumed that the pressure field is continuous such that the Taylor expansion about $\boldsymbol{\xi} = \mathbf{0}$ exists. This fact was used to demonstrate the

convergence of second term of 3.2 to the local gradient operator as ϵ shrinks to 0. Continuing with the idea of term-wise convergence, this section will present the convergence of every term of equation 5.5 to its local counterpart at the local limit. The Taylor expansion of velocity is given as

$$u_i(\mathbf{x} + \boldsymbol{\xi}) = u_i(\mathbf{x}) + \frac{\partial u_i}{\partial x_j}(\mathbf{x})\xi_j + \mathcal{O}(\|\boldsymbol{\xi}\|^2).$$

Using this expansion, we have

$$\begin{aligned} u_j(\mathbf{x}) \lim_{\epsilon \rightarrow 0} \int_{\mathcal{H}_\epsilon} \gamma \omega(\|\boldsymbol{\xi}\|) (u_i(\mathbf{x} + \boldsymbol{\xi}) - u_i(\mathbf{x})) \frac{\xi_j}{\|\boldsymbol{\xi}\|^2} d\boldsymbol{\xi} \\ = u_j(\mathbf{x}) \lim_{\epsilon \rightarrow 0} \gamma \int_{\mathcal{H}_\epsilon} \frac{\omega(\|\boldsymbol{\xi}\|)}{\|\boldsymbol{\xi}\|^2} (u_i(\mathbf{x})\xi_j + \frac{\partial u_i}{\partial x_k} \xi_k \xi_j - u_i(\mathbf{x})\xi_j) + \mathcal{O}(\|\boldsymbol{\xi}\|^2) d\boldsymbol{\xi}, \\ = u_j(\mathbf{x}) \lim_{\epsilon \rightarrow 0} \frac{\partial u}{\partial x_j}(\mathbf{x}) \gamma \int_{\mathcal{H}_\epsilon} \omega(\|\boldsymbol{\xi}\|) \frac{\xi_j \xi_i}{\|\boldsymbol{\xi}\|^2} + \mathcal{O}(\|\boldsymbol{\xi}\|^2) d\boldsymbol{\xi}, \\ = u_j(\mathbf{x}) \lim_{\epsilon \rightarrow 0} \frac{\partial u}{\partial x_j}(\mathbf{x}) \delta_{ji} + \mathcal{O}(\epsilon), \\ = u_j(\mathbf{x}) \lim_{\epsilon \rightarrow 0} \frac{\partial u}{\partial x_i}(\mathbf{x}) + \mathcal{O}(\epsilon), \\ = \mathbf{u} \cdot \nabla \mathbf{u}. \end{aligned} \tag{5.7}$$

Note, as shown below, there is an ϵ^2 term in the denominator of γ which explains the $\mathcal{O}(\epsilon)$ after integration. Here $\omega(\|\boldsymbol{\xi}\|) = \omega_s(\|\boldsymbol{\xi}\|)$ is assumed to be spherically symmetric which implies that

$$\begin{aligned} \int_{\mathcal{H}_\epsilon} \omega_s(\|\boldsymbol{\xi}\|) \frac{\xi_k \xi_j}{\|\boldsymbol{\xi}\|^2} d\boldsymbol{\xi} &= \delta_{kj} \int_{\mathcal{H}_\epsilon} \omega_s(\|\boldsymbol{\xi}\|) \frac{\xi_1^2}{\|\boldsymbol{\xi}\|^2} d\boldsymbol{\xi}, \\ &= \delta_{kj} \int_0^{2\pi} \int_0^\pi \int_0^\epsilon \omega_s(\|\boldsymbol{\xi}\|) \frac{\xi_1^2}{\|\boldsymbol{\xi}\|^2} \|\boldsymbol{\xi}\|^2 \sin \theta d\xi d\theta d\phi, \\ &= \delta_{kj} \frac{m_1}{3}, \end{aligned}$$

where

$$m_1 = \int_{\mathcal{H}_\epsilon} \omega_s(\|\boldsymbol{\xi}\|) d\boldsymbol{\xi},$$

and the spherical coordinates, $\xi_1 = |\boldsymbol{\xi}| \sin \theta \cos \phi$, $\xi_2 = |\boldsymbol{\xi}| \sin \theta \sin \phi$, and $\xi_3 = |\boldsymbol{\xi}| \cos \theta$ have been used to evaluate the integral. Therefore, in order for the first integral in 5.7 to converge to $\mathbf{u} \cdot \nabla \mathbf{u}$ in the limit of vanishing horizon, we require

$$\gamma = \frac{3}{m_1}.$$

The same technique can be used to show the convergence of the Laplacian term. Here, Taylor expansions about $\boldsymbol{\xi} = \mathbf{0}$ are given as:

$$u_i(\mathbf{x} + \boldsymbol{\xi}) = u_i(\mathbf{x}) + \frac{\partial u_i}{\partial x_j} \xi_j + \frac{1}{2} \frac{\partial^2 u_i}{\partial x_j \partial x_k} \xi_j \xi_k + \mathcal{O}(\|\boldsymbol{\xi}\|^3),$$

$$\underline{\nu}(\mathbf{x}, \boldsymbol{\xi}) = \underline{\nu}(\mathbf{x}, \mathbf{0}) + \frac{\partial \underline{\nu}(\mathbf{x}, \mathbf{0})}{\partial \xi_n} \xi_n + \mathcal{O}(\|\boldsymbol{\xi}\|^2),$$

$$\underline{\nu}(\mathbf{x} + \boldsymbol{\xi}, -\boldsymbol{\xi}) = \underline{\nu}(\mathbf{x}, \mathbf{0}) + \frac{\partial \underline{\nu}(\mathbf{x}, \mathbf{0})}{\partial x_n} \xi_n - \frac{\partial \underline{\nu}(\mathbf{x}, \mathbf{0})}{\partial \xi_n} \xi_n + \mathcal{O}(\|\boldsymbol{\xi}\|^2).$$

Substituting these back into the third term of 5.5 and simplifying, gives

$$\begin{aligned}
& \int_{\mathcal{H}} \beta \omega(\|\boldsymbol{\xi}\|) \frac{\xi_i (\underline{\nu}(\mathbf{x}, \mathbf{x}') + \underline{\nu}(\mathbf{x}', \mathbf{x})) \xi_j}{\|\boldsymbol{\xi}\|^2} (u_j(\mathbf{x}') - u_j(\mathbf{x})) d\boldsymbol{\xi} \\
&= \int_{\mathcal{H}} \beta \omega(\|\boldsymbol{\xi}\|) \frac{\xi_i \left(2\underline{\nu}(\mathbf{x}, \mathbf{0}) + \frac{\partial \underline{\nu}(\mathbf{x}, \mathbf{0})}{\partial x_n} + \mathcal{O}(\|\boldsymbol{\xi}\|^2) \right) \xi_j}{\|\boldsymbol{\xi}\|^2} \\
&\quad \times \left(\frac{\partial u_j}{\partial x_m} \xi_m + \frac{1}{2} \frac{\partial^2 u_j}{\partial x_m \partial x_n} \xi_m \xi_n + \mathcal{O}(\|\boldsymbol{\xi}\|^3) \right) d\boldsymbol{\xi}.
\end{aligned}$$

Using the symmetry of the integrand, any odd power of ξ_i can be set to zero.

Now, collecting the terms will give

$$\begin{aligned}
&= \beta \int_{\mathcal{H}} \frac{\omega(\|\boldsymbol{\xi}\|)}{\|\boldsymbol{\xi}\|^2} \left(\xi_n \xi_i \underline{\nu} \xi_j \xi_m \frac{\partial^2 u_j}{\partial x_m \partial x_n} + \frac{\partial u_j}{\partial x_m} \xi_n \xi_i \frac{\partial \underline{\nu}}{\partial x_n} \xi_j \xi_m \right) d\boldsymbol{\xi} + \mathcal{O}(\epsilon^2), \\
&= (\delta_{ij} \delta_{mn} \nu) \frac{\partial}{\partial x_n} \left(\frac{\partial u_j}{\partial x_m} \right) + \left(\frac{\partial u_j}{\partial x_m} \right) \frac{\partial (\delta_{ij} \delta_{mn} \nu)}{\partial x_n} + \mathcal{O}(\epsilon^2), \\
&= \frac{\partial}{\partial x_n} \left((\delta_{ij} \delta_{nm} \nu) \frac{\partial u_j}{\partial x_m} \right) + \mathcal{O}(\epsilon^2), \tag{5.8} \\
&= \nu \frac{\partial^2 u_i}{\partial x_n \partial x_n}, \\
&= \nu \nabla^2 \mathbf{u},
\end{aligned}$$

Where

$$\delta_{ij} \delta_{mn} \nu = \beta \nu \int_{\mathcal{H}} \omega(\|\boldsymbol{\xi}\|) \frac{\xi_n \xi_i \xi_j \xi_m}{\|\boldsymbol{\xi}\|^2} d\boldsymbol{\xi}. \tag{5.9}$$

Above, the symmetry of the integrand has once more been explored. Using polar coordinates, the integral can be evaluated as

$$\begin{aligned}
\int_{\mathcal{H}} \omega_s(\|\boldsymbol{\xi}\|) \frac{\xi_n \xi_i \xi_j \xi_m}{\|\boldsymbol{\xi}\|^2} d\boldsymbol{\xi} &= (\delta_{ni} \delta_{jm} (1 - \delta_{nm}) + \delta_{nj} \delta_{im} (1 - \delta_{ij}) \delta_{nm} \delta_{ij} (1 - \delta_{nj})) \\
&+ \int_{\mathcal{H}} \frac{\xi_1^2 \xi_2^2}{\|\boldsymbol{\xi}\|^2} d\boldsymbol{\xi} + \delta_{nm} \delta_{ij} \delta_{nj} \int_{\mathcal{H}} \frac{\xi_1^4}{\|\boldsymbol{\xi}\|^2} d\boldsymbol{\xi}, \\
&= (\delta_{ni} \delta_{jm} (1 - \delta_{nm}) + \delta_{nj} \delta_{im} (1 - \delta_{ij}) + \delta_{nm} \delta_{ij} (1 - \delta_{nj})) \frac{m_2}{15} + 3\delta_{nm} \delta_{ij} \delta_{nj} \frac{m_2}{15}, \\
&= (\delta_{ni} \delta_{jm} + \delta_{nj} \delta_{im} + \delta_{nm} \delta_{ij}) \frac{m_2}{15}.
\end{aligned}$$

Now, the result of the substitution is equated with the two-point and classical dynamic viscosity,

$$\delta_{nm} \delta_{ij} \nu = \underline{\nu} \beta (\delta_{ni} \delta_{jm} + \delta_{nj} \delta_{im} + \delta_{nm} \delta_{ij}) \frac{m_2}{15}$$

$$3\delta_{ij} \nu = \underline{\nu} \beta \delta_{ij} \frac{m_2}{3}$$

$$\nu = \underline{\nu} \beta \frac{m_2}{9}$$

which reveals that the nonlocal two-point dynamic viscosity is equivalent to its local counterpart, $\underline{\nu} = \nu$ if $\beta = \frac{9}{m_2}$ with

$$m_2 = \int_{\mathcal{H}_e} \omega_s(\|\boldsymbol{\xi}\|) \xi_i \xi_i d\boldsymbol{\xi}.$$

For a two-dimensional domain and with a choice of triangular influence function, $\omega = (1 - \frac{\xi}{\epsilon})$,

$$\begin{aligned}
m_2 &= \int_0^{2\pi} \int_0^\epsilon (1 - \frac{\xi}{\epsilon}) \xi_i \xi_i d\boldsymbol{\xi} \\
&= \int_0^{2\pi} \int_0^\epsilon (1 - \frac{\xi}{\epsilon}) \xi_i \xi_i d\boldsymbol{\xi} (|\boldsymbol{\xi}| d\theta) \\
&= \int_0^{2\pi} \int_0^\epsilon (1 - \frac{\xi}{\epsilon}) \xi^3 d\boldsymbol{\xi} d\theta \\
&= \int_0^{2\pi} \int_0^\epsilon (\xi^3 - \frac{\xi^4}{\epsilon}) d\boldsymbol{\xi} d\theta \\
&= [2\pi - 0] [\frac{\epsilon^4}{4} - \frac{\epsilon^5}{5\epsilon}] \\
&= \frac{\pi\epsilon^4}{10}
\end{aligned}$$

which gives

$$\beta = \frac{90}{\pi\epsilon^4}$$

Using the Taylor expansions once more, the convergence of the gradient term can be shown as below.

$$u(\mathbf{x} + \boldsymbol{\xi}) = u(\mathbf{x}) + \frac{\partial u}{\partial x_j}(\mathbf{x}) \xi_j + \mathcal{O}(|\boldsymbol{\xi}|^2). \quad (5.10)$$

Substituting (5.10) back into 5.6 gives:

$$\begin{aligned}
& \lim_{\epsilon \rightarrow 0} \int_{\mathcal{H}_\epsilon} \gamma \omega(\|\boldsymbol{\xi}\|) (u(\mathbf{x} + \boldsymbol{\xi}) - u(\mathbf{x})) \frac{\xi_i}{\|\boldsymbol{\xi}\|^2} d\boldsymbol{\xi} \\
&= \lim_{\epsilon \rightarrow 0} \gamma \int_{\mathcal{H}_\epsilon} \frac{\omega(\|\boldsymbol{\xi}\|)}{\|\boldsymbol{\xi}\|^2} (u(\mathbf{x})\xi_i + \frac{\partial u}{\partial x_j}(\mathbf{x})\xi_i\xi_j - u(\mathbf{x})\xi_i) + \mathcal{O}(\|\boldsymbol{\xi}\|^2) d\boldsymbol{\xi}, \\
&= \lim_{\epsilon \rightarrow 0} \frac{\partial u}{\partial x_j}(\mathbf{x}) \gamma \int_{\mathcal{H}_\epsilon} \omega(\|\boldsymbol{\xi}\|) \frac{\xi_j \xi_i}{\|\boldsymbol{\xi}\|^2} + \mathcal{O}(\|\boldsymbol{\xi}\|^2) d\boldsymbol{\xi}, \\
&= \lim_{\epsilon \rightarrow 0} \frac{\partial u}{\partial x_j}(\mathbf{x}) \delta_{ji} + \mathcal{O}(\epsilon), \\
&= \lim_{\epsilon \rightarrow 0} \frac{\partial u}{\partial x_i}(\mathbf{x}) + \mathcal{O}(\epsilon), \\
&= \nabla u.
\end{aligned}$$

5.3 Discretization

The nonlocal model has been solved in parallel using equally spaced nodes on a two-dimensional grid. In order to solve these equations using the finite number of nodes chosen here, it is required to first present the discretized version of the proposed model in which the integral equations are presented as finite sums. NOX [5], the nonlinear solver from Trilinos [1] was chosen as the nonlinear solver, AztecOO [83] was used as the linear solver and the Zoltan package was used to perform the load balancing. The discretized form

of equation 5.5 can be written as:

$$\begin{aligned}
& \frac{u_m^{N+1}(\mathbf{x}_I) - u_m^N(\mathbf{x}_I)}{\Delta t} + u_n^{N+1}(\mathbf{x}_I) \sum_J \gamma\omega(\|\boldsymbol{\xi}\|) (u_m^{N+1}(\mathbf{x}_J) - u_m^{N+1}(\mathbf{x}_I)) \frac{\xi_n}{\|\boldsymbol{\xi}\|^2} A_J \\
& - \sum_J \beta\omega(\|\boldsymbol{\xi}\|) \frac{\xi_m(\boldsymbol{\nu}(\mathbf{x}, \mathbf{x}') + \boldsymbol{\nu}(\mathbf{x}', \mathbf{x}))\xi_n}{\|\boldsymbol{\xi}\|^2} (u_n^{N+1}(\mathbf{x}_J) - u_n^{N+1}(\mathbf{x}_I)) A_J \\
& - \frac{\lambda}{\rho_0} \sum_J \gamma\omega(\|\boldsymbol{\xi}\|) (u_m^{N+1}(\mathbf{x}_J) - u_m^{N+1}(\mathbf{x}_I)) \frac{\xi_m}{\|\boldsymbol{\xi}\|^2} A_J = 0
\end{aligned} \tag{5.11}$$

Above, A_j can be thought of as Δx^2 for 2-D case and as Δx for the 1-D case for all grid cells that are completely interior to the horizon. Subscripts m and n represents components of $\boldsymbol{\xi}$ in the x and y directions and superscript N is used to represent the current time step. Here $\mathbf{x}_j := \mathbf{x}_i + \boldsymbol{\xi}$ where j stands for a neighboring node and x_i is the spatial position of the node of interest.

5.4 Results and Discussion

Above, the nonlocal Navier-Stokes model is formally introduced as the set of equations 5.5. The mathematical prove of the convergence of this model to the local penalty formulation of the Navier-Stokes equations was also provided. In what follows, the capabilities of the proposed model will be explored by simulating channel flows that have established numerical solutions. This section will begin by simulating flow inside a channel with a restriction. The incompressibility condition dictates an increase in the average velocity as the flow enters the restricted part of the channel. This problem will be used to

tune in the model and find the appropriate penalty parameter in order to enforce the divergence-free condition. This parameter will then be used in the following simulations to model more complex problems such the von Karman (VK) vortex street simulation.

5.4.1 Case 1: Flow with Restriction

In an incompressible flow, a reduction in area will result in an increase in the velocity. This balance will ensure a constant volumetric flow rate. However, the penalty formulation of the Navier-Stokes equations and the nonlocal formulation of this penalty formulation can only enforce incompressibility through the use of a large penalty parameter. This penalty parameter is a function of other flow and simulation parameters such as the average velocity, viscosity and the time step. Therefore, it is essential that λ is calculated prior to each simulation.

5.4.1.1 Parametrization

The height restriction flow has been simulated with domain length, $L = 6$ m, and domain height, $H = 2$ m. The plates are assumed to be infinitely large in the out of plane direction. Time step, $t = 0.003$ s, density, $\rho = 1.225$ kg/m^3 , viscosity, $\mu = 1.8e - 5$ Pa.s and the chosen grid spacing, $\Delta x = H/100$ m. Here, horizon size is chosen in a way that each node can only interact with its 4 closest neighbors.

5.4.1.2 Boundary Conditions

For this simulation, the no-slip boundary condition is chosen for the upper and lower walls and constant inflow and outflow velocity, $u_x = 0.025$ m/s for the left and right edges. For ease of simulation and without any loss of information, the no slip boundary condition is not enforced on the outer surfaces of the rectangular restriction.

5.4.1.3 Convergence Study

As the penalty parameter gets larger, increasingly smaller time steps are required to ensure the convergence of the non-linear solver. As a result, it's important to find out the smallest penalty parameter that is still large enough to enforce incompressibility. For the specified parameters, the simulation was run using an increasing penalty parameter until convergence to the analytical solution was observed. Figure 5.1 shows the result of this convergence study. Here, the nonlocal solution and the analytical solution are in good agreement for penalty parameters larger than 100.

5.4.1.4 Simulation Results

The flow profile calculated by the nonlocal model is presented by figure 5.2. Here $\lambda = 100$ and the simulation results presented are for $t = 2550$ s. In addition to correctly calculating the mean velocity increase over the object, the nonlocal model is also shown to be capable of capturing more complex features of this domain. The flow is shown to separate from the object at the

leading and trailing edges of the object due to the momentum effects. At the trailing edge and as the flow expands back to the full width of the channel, the viscous forces have caused the formation of a vortex.

5.4.2 Case 2: Laminar Flow Between Two Infinitely Large Plates

In addition to λ , it's important to understand the convergence rate of the results of the nonlocal model to the exact local solution as the number of nodes is increased. In the second case presented here, the formation and development of the boundary layer as a flow enters the gap between two parallel plates is explored. This is another bench mark problem for which an analytical solution exists. In this case, as the flow continues its path through the channel, the viscosity effects slow down fluid particles near the walls. As incompressibility would require, the particles towards the center of the flow have

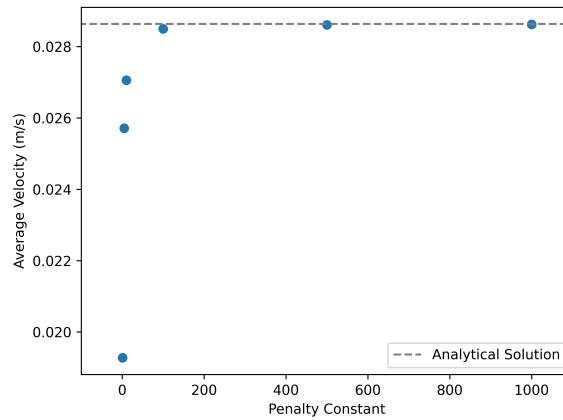


Figure 5.1: The convergence study done on the penalty parameter indicates that a λ larger than 100 would sufficiently enforce incompressibility.

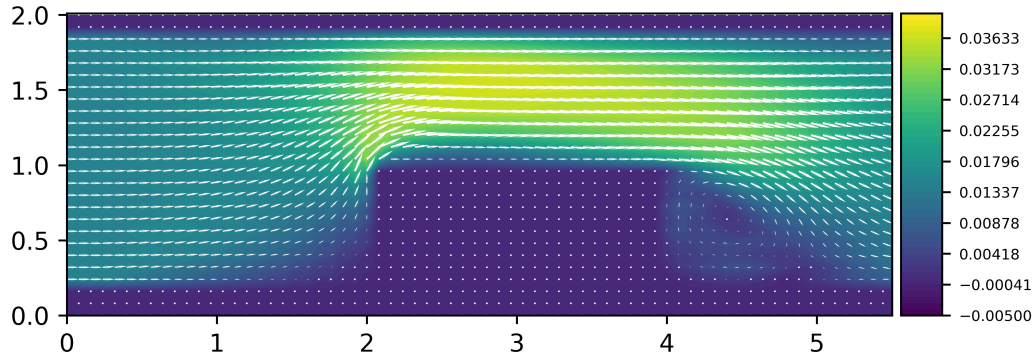


Figure 5.2: A reduction of available cross-sectional area has resulted in a increase in the mean flow velocity over the rectangular restriction. The nonlocal model is also shown to have captured more complex features of this flow such as the formation of a vortex at the trailing edge of the rectangular object

to speed up in order to maintain a constant flow rate. figure 5.4 demonstrates the formation and development of the boundary layer until a fully developed flow inside the channel is achieved. The profile stays constant after this point with maximum velocity at the central line of the channel reaching $3/2 u_{\text{mean}}$.

5.4.2.1 Parametrization

For this simulation, $L = 15$ m, $H = 3$ m, and horizon size is again set to closest neighbors only. Here, penalty parameter $\lambda = 100$ as this number is shown to be sufficiently large enough to enforce incompressibility. The plates are assumed to be infinitely large in the out of plane direction. Time step, $t = 0.0002$ s, density, $\rho = 1.225 \text{ kg/m}^3$ and viscosity, $\mu = 1.8e - 5$ Pa.s.

5.4.2.2 Boundary Conditions

In the channel flow simulation, no slip boundary condition is set at the inner surfaces of the upper and lower walls such that $u_x = 0$ and $u_y = 0$. The x-component of the velocity, $u_x = 0.015$ m/s has been specified on the left edge of the domain and “do nothing” boundary condition has been employed for the right edge of the domain.

5.4.2.3 Convergence Study

The mathematical proof presented at the beginning of this chapter requires an infinitely decreasing grid spacing Δx in order to achieve convergence to the local limit. More specifically, getting to the local solution is only possible through δ -convergence. This is when the discretization is refined at a higher rate as the rate at which m , the number of neighbors in the horizon, is increased [12, 14]. Figure 5.3 shows the result of this convergence study by plotting the calculated flow profile of a vertical cross-section in the channel where a fully developed flow is achieved. Here, the local limit of the nonlocal model is shown to be in close agreement to the analytical solution.

5.4.2.4 Simulation Results

The result of this simulation with $\Delta x = 0.05$ m and $t = 600$ s is presented in figure 5.4. Here, the boundary layer thickness is shown to increase for the first 7 meters of the channel and until the fully developed flow is achieved. As shown by fig. 5.3, the centerline velocity of the fully developed

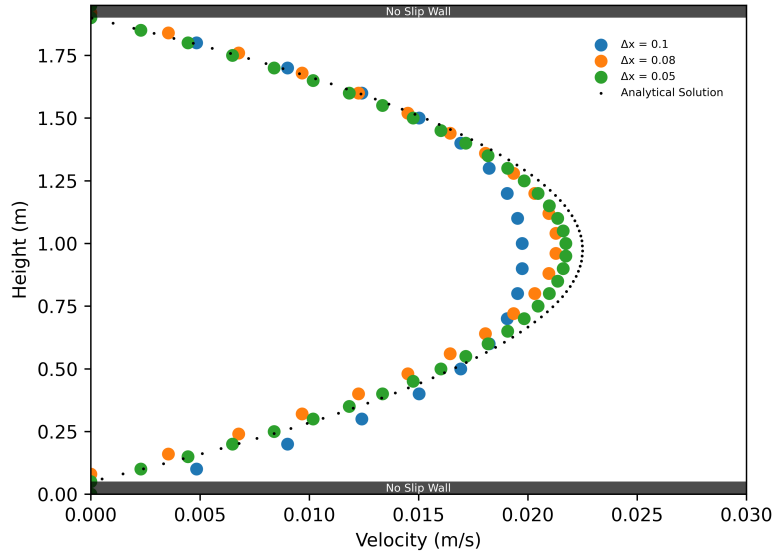


Figure 5.3: As the number of nodes are increased, the profile calculated by the nonlocal model is shown to converge to the analytical solution. The anti-symmetry of the lines are due to the automatic placement of the nodes for the cases where the domain height is not divisible by the number of nodes. The anti-symmetry fades away as the number of nodes is increased

region for this simulation is in close agreement with the analytical solution.

5.4.3 Case 3: Flow Over a Cylinder

The problem of flow past bluff bodies, also known as the von Karman vortex street problem, is one of the classical problems of fluid mechanics. This problem was first studied experimentally by Strouhal [96]. In 1911, von Karman [104] offered the first fundamental theoretical insights for this phenomena.

This surprisingly common event is the reason why flags continuously

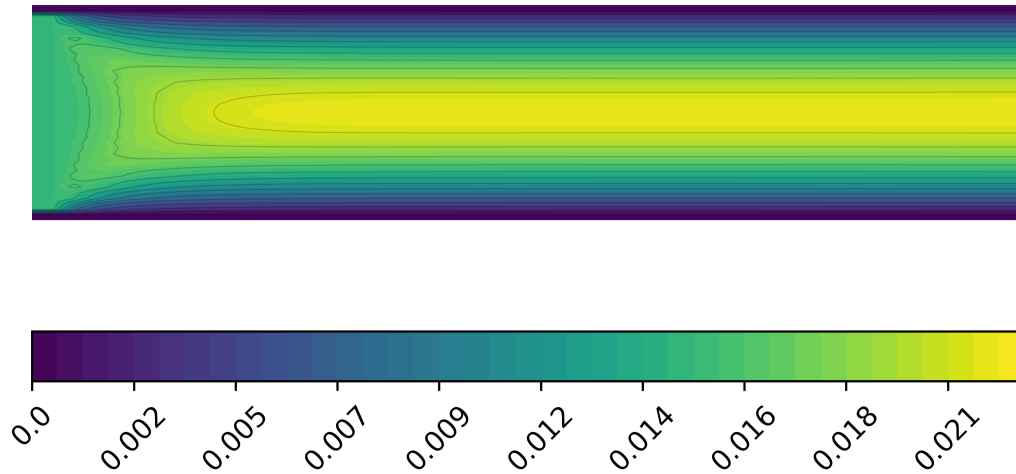


Figure 5.4: Formation and development of the boundary layer for flow between two parallel plates as simulated by the nonlocal model

flap and why electrical wires hum on a windy day. It also has applications in complex engineering problems such as in aircraft and missile design [34] and chemical mixing [74]. In the 2D flow past a cylindrical body and above a critical Reynolds number (typically 50), shedding of counter-rotating vortices is observed. These non-linear oscillations can be associated with undesirable effects such as increased drag [20].

The von Karman vortex street is a well understood phenomena with available numerical results. In this section, the proposed nonlocal model will be used to simulate the flow past a cylindrical object for varying flow velocities and the results will be compared to other available local and nonlocal simulations. A regular von Karman street is only expected in the wake of the cylindrical object for Reynolds numbers above the critical value of 50. At Reynolds

numbers below this critical value, the wake is expected to be laminar. In this section, the problem of flow past a cylinder with low Re number will be studied first. The calculated velocity profile from the nonlocal model will be compared to both local and nonlocal reference results [60]. In this work, the authors introduced a nonlocal model based on the PDDO method which is shown to accurately model the VK street pattern and the results are shown to be in good agreement with the local solution calculated by ANSYS Fluent [2].

5.4.3.1 Parametrization

For this simulation, $L = 15$ m and $H = 6$ m. Here, the penalty parameter, λ is set to 1000. The plates are assumed to be infinitely large in the out of plane direction. Time step, $t = 1e - 5$ s, density, $\rho = 1.0 \text{ kg/m}^3$ and viscosity, $\mu = 1$ Pa.s. The radius of the cylindrical object, r is chosen to be 1 m and the incoming velocity is set to 10 m/s . For these inputs, the Reynolds number will be equal to 10.

5.4.3.2 Boundary Conditions

No slip boundary condition is applied to the inner surfaces of the upper and lower walls as well as to the surface of the cylindrical object such that $u_x = 0$ and $u_y = 0$. The components of the velocity, $u_x = 10 \text{ m/s}$ and $u_y = 0 \text{ m/s}$ are only specified at the left edge of the domain and a “do nothing” boundary condition has been employed for the right edge of the domain.

5.4.3.3 Convergence Study

Figures 5.5 and 5.6 present the results of the δ -convergence study performed on the proposed nonlocal model. Here, the velocity fields are compared along the vertical and the horizontal line going through the center of the cylindrical object. The solution of the proposed nonlocal model is shown to be in good agreement with the reference local and nonlocal solutions. Furthermore, the result of the proposed nonlocal model is shown to converge to the reference solutions as the mesh is refined based on the δ -convergence rules. That is, the mesh is refined faster than the rate at which m , the number of neighbors, is increased. here, n is the number of nodes used in the x-direction.

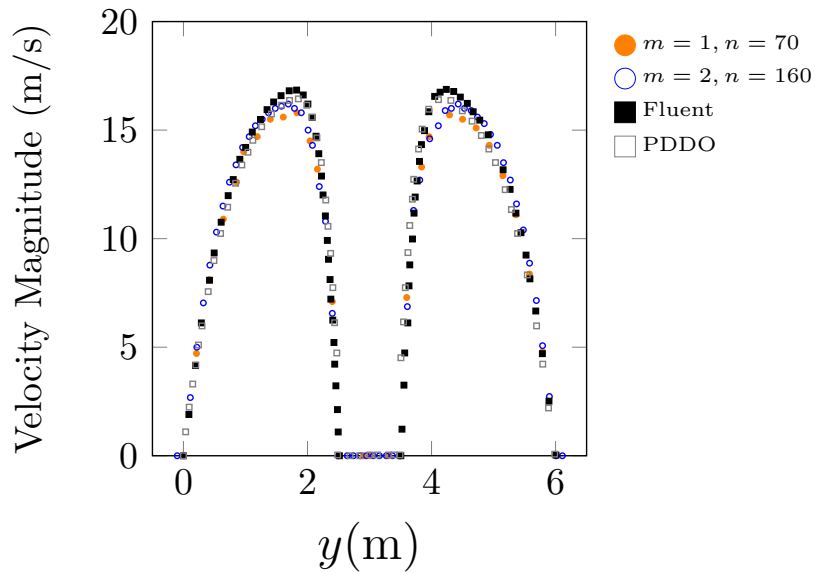


Figure 5.5: Illustration of the velocity variation along a vertical line passing through the center of the cylindrical object shows the convergence of the results of the proposed nonlocal model to the local solution calculated by ANSYS Fluent and local limit of the PDDO simulation presented by Nguyen et al. [60]

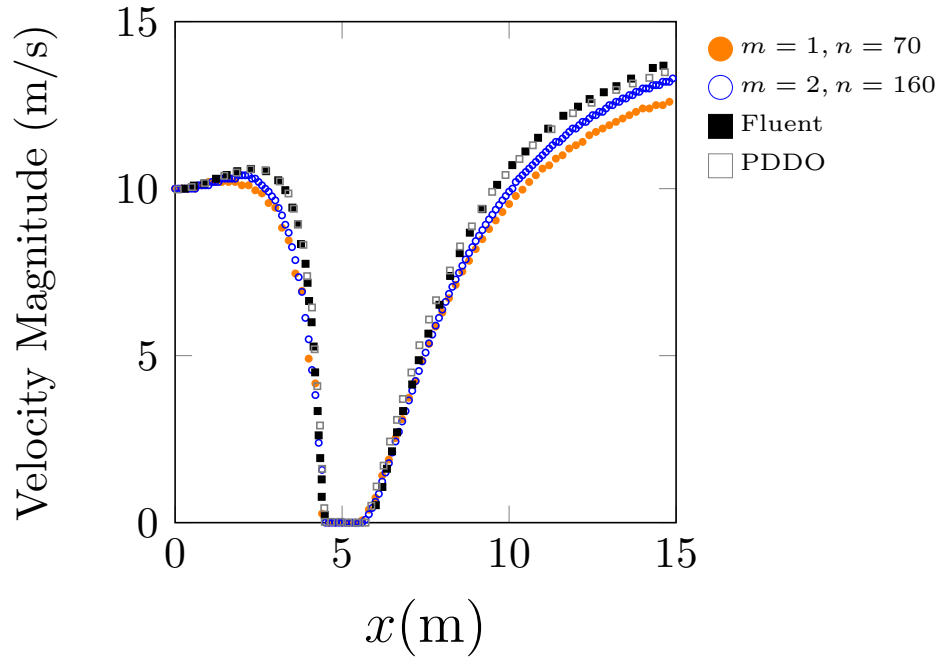


Figure 5.6: Illustration of the velocity variation along a horizontal line passing through the center of the cylindrical object shows the convergence of the results of the proposed nonlocal model to the local solution calculated by ANSYS Fluent and local limit of the PDDO simulation presented by Nguyen et al. [60]

5.4.3.4 Simulation Results

Figures 5.7 and 5.8 illustrate the variation of the x and y components of the velocity as simulated by the nonlocal model at $t = 2$ s. Here, $\Delta x = 0.1$ m and $m = 2$. As the flow reaches the cylindrical object, the pressure increase at the leading edge of the cylinder is shown to split the flow into two separate streams above and below the cylinder. This separation is more clearly seen on the fig.5.8 as the vertical component of the velocity is shown to change sign ahead of the cylinder and at the centerline of the channel. At this Re number,

the two streams are shown to smoothly re-attach behind the cylinder, forming a laminar wake.

Having shown that the proposed nonlocal model will recover the local classical solution at its local limit, the rest of this section will be used to study the capabilities of the proposed model in simulating the vortex shedding phenomena in the wake of the cylinder as the Re number is increased.

Next, let us explore the case where the inlet velocity is increased such that the Re number would rise above the critical value of 50. For this case, counter-rotating vortices are expected to form as the flow passes over the body. The interaction of these vortices would result in non-linear oscillations behind the body which over time form a regular von Karman street.

5.4.3.5 Parametrization

In this simulation, The domain length, $L = 15$ m, the height, $H = 6$ m, and horizon includes the closest neighbors only. Here, the penalty parameter $\lambda = 1000$. The plates are assumed to be infinitely large in the out of plane direction. Time step, $t = 1e - 5$ s, density, $\rho = 1.0 \text{ kg/m}^3$ and viscosity, $\mu = 1$ Pa.s. The radius of the cylindrical object, r is chosen to be 1 m and the incoming velocity is set to 100 m/s . For these inputs, the Reynolds number will be equal to 100.

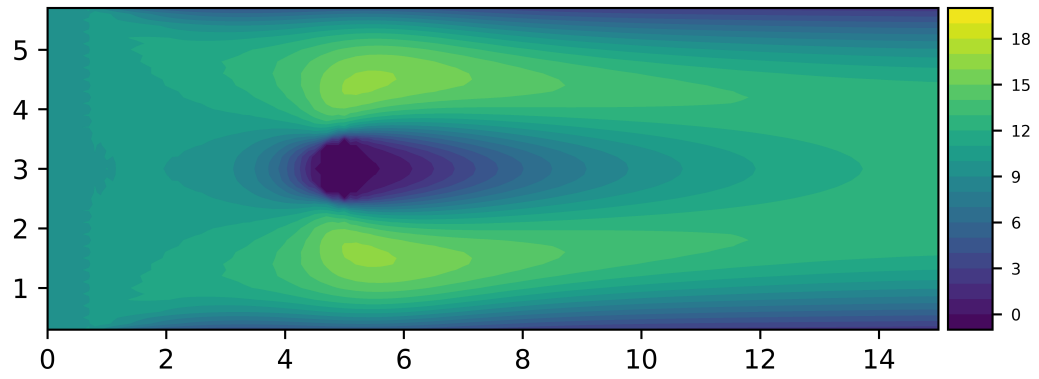


Figure 5.7: Variation of x-component of velocity, u (m/s) as simulation by the proposed nonlocal model

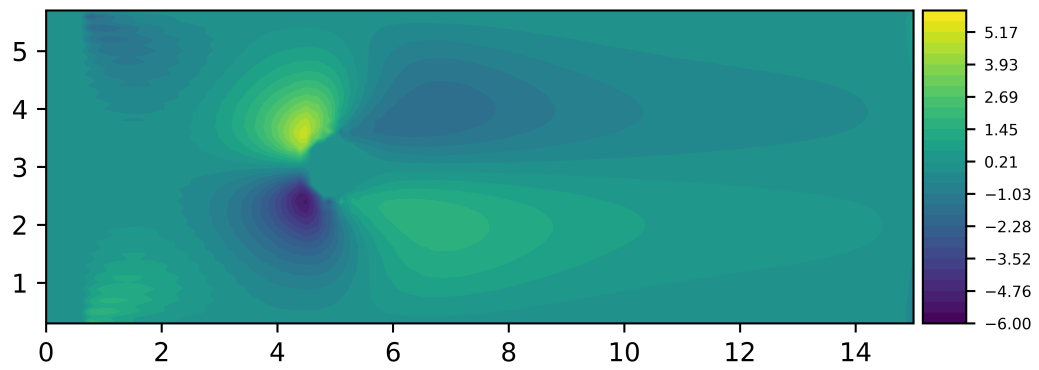


Figure 5.8: Variation of y-component of velocity, v (m/s) as simulation by the proposed nonlocal model

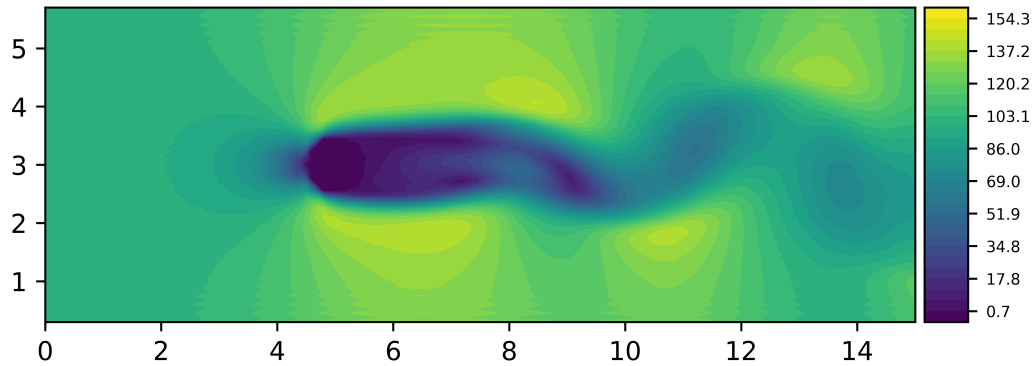


Figure 5.9: As the Re is increased, the combination of counter-rotating vortices behind the cylindrical object result in the formation of the nonlinear oscillations known as the von Karman street

5.4.3.6 Simulation Results

By increasing the inlet velocity, and without any further changes to the setup of the problem, the nonlocal model is shown to predict the formation of the VK vortices behind the cylindrical body. Figure 5.9 illustrates the variations of the velocity magnitude for the case of vortex tail down. vortices at $t = 2$ s. As shown by figure 5.10b, in the case of vortex tail down the the value of the velocity magnitude is expected to be slightly larger for the nodes with $0 < y < 3$. Figure 5.11 illustrates the development of the counter-rotating vortices as they detach from the trailing edge of the cylinder.

5.5 Conclusion

This chapter was built based on the other chapters of the project and presented a nonlocal model as an alternative for the penalty formulation of

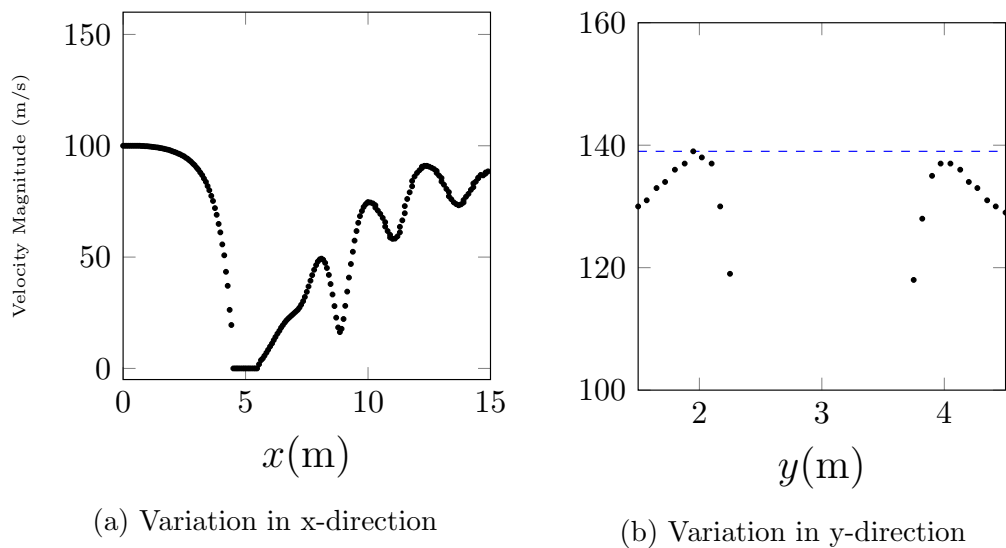


Figure 5.10: Variation of velocity magnitude on a vertical and a horizontal line passing through the center of the cylinder

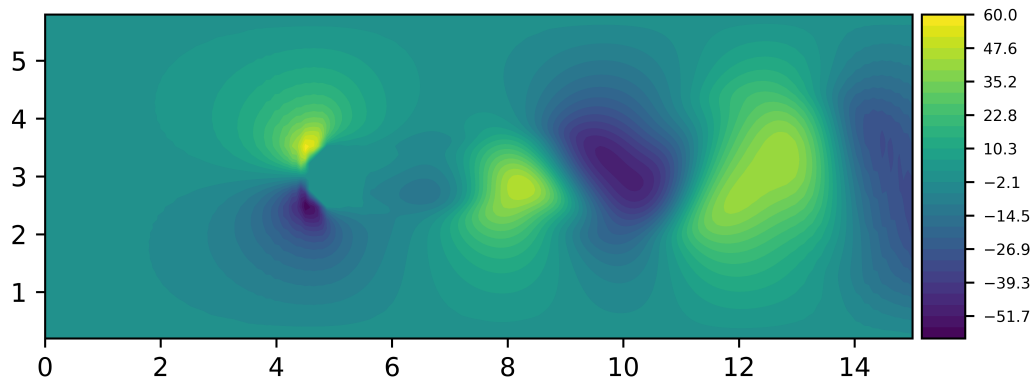


Figure 5.11: Variation of the y component of the velocity clearly showing the separation of the counter-rotating vortices

the Navier-Stokes equations for a two-dimensional incompressible flow. The model was used to simulate benchmark problems in fluid dynamics and the convergence of the simulations to the available local and nonlocal solutions

were presented. The predictions of the proposed model at its local limit were shown to be in great agreement with the analytical solutions. Fluid mechanics is an under-explored section of peridynamic theory. The proposed model in this chapter was shown to be a strong peridynamic-based approach for multi-scale modeling in fluid mechanics.

Chapter 6

Summary

Over the past 20 years, *peridynamic* theory has become a well-established nonlocal method for simulation of solid bodies. The concepts introduced by the peridynamic theory are proven to be especially helpful for problems in solid mechanics, which include spatial discontinuities. The capabilities of PD as a multi-scale modeling tool also make it an ideal candidate for modeling problems of heat and mass transport in fluid mechanics. However, fluid mechanics has so far been an under-explored section of peridynamic theory. The goal of this dissertation is to lay the foundation for the use of peridynamic theory in fluid mechanics by presenting viable numerical techniques for modeling heat and mass transport problems using peridynamic-based nonlocal models.

This investigation starts with proposing a nonlocal advection-diffusion model for two-phase flow in porous media. The proposed nonlocal formulation is shown to be naturally capable of handling the sharp changes in the concentration at the interphase of the fluids. As a result, the proposed model captures the formation and development of instabilities at the fluid interface. These instabilities were shown to develop into channels of the less viscous fluid that penetrated deep into the second phase. This is a phenomenon commonly

known as viscous fingers. The proposed nonlocal model was shown to capture the effects of dispersion on fluid mixing. As far as we know, this nonlocal advection-diffusion model is the first numerical attempt to include the direct effect of dispersion in a viscous fingering simulation.

Chapter 4 of this dissertation focused on the derivation of the peridynamic kernel. As discussed in length, deriving the correct peridynamic kernel is a prerequisite to the calculation of the nonlocal limit. This dissertation provides a systematic method for the calculation of the nonlocal kernel for small domains, where running an MD simulation of the domain is possible. More specifically, this chapter focuses on the transfer of heat in nanofluids. This is a scenario in which macro-scale changes in the conductivity of the fluid can only be understood through the accurate modeling of the interactions at the atomic layer. An MD model is used to introduce a systematic approach for the calculation of the nonlocal kernel and the kernel is used to estimate the thermal conductivity of a wide range of Ar-Cu nanofluids with different copper loading. The estimates are shown to be in great agreement with the MD results.

Finally, Chapter 5 was builds on the other chapters of this project and presents a nonlocal model as an alternative to the penalty formulation of the Navier-Stokes equations for a two-dimensional incompressible flow. This model is used to solve some of the most common benchmark problems of fluid dynamics. In each case, the convergence of the nonlocal model to the analytical solution is shown. The nonlocal model is also used to model more

complex flow problems such as the von Karman Street problem. This chapter demonstrates the capabilities of the proposed nonlocal model for modeling multi-scale phenomena such as vortex shedding.

Bibliography

- [1] <https://trilinos.github.io>, 2020 (accessed May 22, 2020).
- [2] ANSYS. Ansys fluent - cfd software — ansys, 2016.
- [3] Udo Gaetan Araktingi, FM Orr Jr, et al. Viscous fingering in heterogeneous porous media. *SPE Advanced Technology Series*, 1(01):71–80, 1993.
- [4] E Askari, F Bobaru, RB Lehoucq, ML Parks, SA Silling, and O Weckner. Peridynamics for multiscale materials modeling. In *Journal of Physics: Conference Series*, volume 125, page 012078. IOP Publishing, 2008.
- [5] Brett Bader, Russ Hooper, and Tammy Kolda. *NOX Project Webpage*, 2022 (accessed Jan 15, 2022).
- [6] Daniel S Banks and Cécile Fradin. Anomalous diffusion of proteins due to molecular crowding. *Biophysical journal*, 89(5):2960–2971, 2005.
- [7] Daniel S. Banks and Cécile Fradin. Anomalous diffusion of proteins due to molecular crowding. *Biophysical Journal*, 89(5):2960–2971, 2005.
- [8] Grigory Isaakovich Barenblatt. The mathematical theory of equilibrium cracks in brittle fracture. In *Advances in applied mechanics*, volume 7, pages 55–129. Elsevier, 1962.

- [9] PSSK Bhattacharya, SK Saha, A Yadav, PE Phelan, and RS Prasher. Brownian dynamics simulation to determine the effective thermal conductivity of nanofluids. *Journal of Applied Physics*, 95(11):6492–6494, 2004.
- [10] Irmgard Bischofberger, Radha Ramachandran, and Sidney R Nagel. An island of stability in a sea of fingers: emergent global features of the viscous-flow instability. *Soft matter*, 11(37):7428–7432, 2015.
- [11] Florin Bobaru and Monchai Duangpanya. The peridynamic formulation for transient heat conduction. *International Journal of Heat and Mass Transfer*, 53(19):4047–4059, 2010.
- [12] Florin Bobaru and Monchai Duangpanya. A peridynamic formulation for transient heat conduction in bodies with evolving discontinuities. *Journal of Computational Physics*, 231(7):2764–2785, 2012.
- [13] Florin Bobaru and Youn Doh Ha. Adaptive refinement and multi-scale modeling in 2d peridynamics. *International Journal for Multiscale Computational Engineering*, 9(6), 2011.
- [14] Florin Bobaru, Mijia Yang, Leonardo Frota Alves, Stewart A Silling, Ebrahim Askari, and Jifeng Xu. Convergence, adaptive refinement, and scaling in 1d peridynamics. *International Journal for Numerical Methods in Engineering*, 77(6):852–877, 2009.

- [15] M Chandrasekar and S Suresh. A review on the mechanisms of heat transport in nanofluids. *Heat Transfer Engineering*, 30(14):1136–1150, 2009.
- [16] Cédric Chevalier, Robert Heaphy, and Bruce Hendrickson. *Zoltan Project Webpage*, 2022 (accessed Jan 15, 2022).
- [17] Stephen US Choi and Jeffrey A Eastman. Enhancing thermal conductivity of fluids with nanoparticles. Technical report, Argonne National Lab., IL (United States), 1995.
- [18] Chan Hee Chon, Kenneth D Kihm, Shin Pyo Lee, and Stephen US Choi. Empirical correlation finding the role of temperature and particle size for nanofluid (al 2 o 3) thermal conductivity enhancement. *Applied Physics Letters*, 87(15):153107, 2005.
- [19] MA Christie, AH Muggeridge, JJ Barley, et al. 3d simulation of viscous fingering and wag schemes. *SPE reservoir engineering*, 8(01):19–26, 1993.
- [20] Kelly Cohen, Stefan Siegel, Dave Wetlesen, Jeff Cameron, and Aaron Sick. Effective sensor placements for the estimation of proper orthogonal decomposition mode coefficients in von kármán vortex street. *Journal of Vibration and Control*, 10(12):1857–1880, 2004.
- [21] Brian N Cox, Huajian Gao, Dietmar Gross, and Daniel Rittel. Modern topics and challenges in dynamic fracture. *Journal of the Mechanics*

- and Physics of Solids*, 53(3):565–596, 2005.
- [22] Wenzheng Cui, Minli Bai, Jizu Lv, Guojie Li, and Xiaojie Li. On the influencing factors and strengthening mechanism for thermal conductivity of nanofluids by molecular dynamics simulation. *Industrial & engineering chemistry research*, 50(23):13568–13575, 2011.
- [23] Dibakar Datta. Introduction to extended finite element (xfem) method. *arXiv preprint arXiv:1308.5208*, 2013.
- [24] Amir H Delgoshaie, Daniel W Meyer, Patrick Jenny, and Hamdi A Tchelepi. Non-local formulation for multiscale flow in porous media. *Journal of Hydrology*, 531:649–654, 2015.
- [25] Qiang Du, Max Gunzburger, Richard B Lehoucq, and Kun Zhou. Analysis and approximation of nonlocal diffusion problems with volume constraints. *SIAM review*, 54(4):667–696, 2012.
- [26] Qiang Du, Max Gunzburger, Richard B Lehoucq, and Kun Zhou. A non-local vector calculus, nonlocal volume-constrained problems, and nonlocal balance laws. *Mathematical Models and Methods in Applied Sciences*, 23(03):493–540, 2013.
- [27] Marta D’Elia and Max Gunzburger. Identification of the diffusion parameter in nonlocal steady diffusion problems. *Applied Mathematics & Optimization*, 73(2):227–249, 2016.

- [28] Jeffery A Eastman, US Choi, Shaoping Li, LJ Thompson, and Shinyo Lee. Enhanced thermal conductivity through the development of nanofluids. *MRS online proceedings library archive*, 457, 1996.
- [29] Jeffrey A Eastman, SUS Choi, Sheng Li, W Yu, and LJ Thompson. Anomalously increased effective thermal conductivities of ethylene glycol-based nanofluids containing copper nanoparticles. *Applied physics letters*, 78(6):718–720, 2001.
- [30] Jeffrey A Eastman, SR Phillpot, SUS Choi, and P Keblinski. Thermal transport in nanofluids. *Annu. Rev. Mater. Res.*, 34:219–246, 2004.
- [31] Albert Einstein. *Investigations on the Theory of the Brownian Movement*. Courier Corporation, 1956.
- [32] Brenden P Epps and Benoit Cushman-Roisin. Turbulence modeling via the fractional laplacian. *arXiv preprint arXiv:1803.05286*, 2018.
- [33] Yan Gao and Selda Oterkus. Multi-phase fluid flow simulation by using peridynamic differential operator. *Ocean Engineering*, 216:108081, 2020.
- [34] EA1650161 Gillies. Low-dimensional control of the circular cylinder wake. *Journal of Fluid Mechanics*, 371:157–178, 1998.
- [35] R Granek. From semi-flexible polymers to membranes: anomalous diffusion and reptation. *Journal de Physique II*, 7(12):1761–1788, 1997.

- [36] Ehsan Haghghat, Ali Can Bekar, Erdogan Madenci, and Ruben Juanes. A nonlocal physics-informed deep learning framework using the peridynamic differential operator. *Computer Methods in Applied Mechanics and Engineering*, 385:114012, 2021.
- [37] R.L. Crosser Hamilton. Thermal conductivity of heterogeneous two-component systems. 1(3):187–191, 1962.
- [38] George M Homsy. Viscous fingering in porous media. *Annual review of fluid mechanics*, 19(1):271–311, 1987.
- [39] Rami Jabakhanji and Rabi H Mohtar. A peridynamic model of flow in porous media. *Advances in Water Resources*, 78:22–35, 2015.
- [40] Fatemeh Jabbari, Ali Rajabpour, and Seifollah Saedodin. Thermal conductivity and viscosity of nanofluids: a review of recent molecular dynamics studies. *Chemical Engineering Science*, 174:67–81, 2017.
- [41] Lars Jacobsson, Christer Persson, and Solveig Melin. In-situ esem study of thermo-mechanical fatigue crack propagation. *Materials Science and Engineering: A*, 496(1-2):200–208, 2008.
- [42] Birendra Jha, Luis Cueto-Felgueroso, and Ruben Juanes. Fluid mixing from viscous fingering. *Physical review letters*, 106(19):194502, 2011.
- [43] Hongbo Kang, Yuwen Zhang, Mo Yang, and Ling Li. Molecular dynamics simulation on effect of nanoparticle aggregation on transport

- properties of a nanofluid. *Journal of Nanotechnology in Engineering and Medicine*, 3(2), 2012.
- [44] Hyun Uk Kang, Sung Hyun Kim, and Je Myung Oh. Estimation of thermal conductivity of nanofluid using experimental effective particle volume. *Experimental Heat Transfer*, 19(3):181–191, 2006.
- [45] Amit Katiyar, John T Foster, Hisanao Ouchi, and Mukul M Sharma. A peridynamic formulation of pressure driven convective fluid transport in porous media. *Journal of Computational Physics*, 261:209–229, 2014.
- [46] Phillbot Keblinski, SR Phillpot, SUS Choi, and JA Eastman. Mechanisms of heat flow in suspensions of nano-sized particles (nanofluids). *International journal of heat and mass transfer*, 45(4):855–863, 2002.
- [47] Joseph Klafter and Igor M Sokolov. Anomalous diffusion spreads its wings. *Physics world*, 18(8):29, 2005.
- [48] S Krishnamurthy, Phelan Bhattacharya, PE Phelan, and RS Prasher. Enhanced mass transport in nanofluids. *Nano letters*, 6(3):419–423, 2006.
- [49] Larry W Lake and Paul B Venuto. A niche for enhanced oil recovery in the 1990s. *Oil & Gas Journal*, 88(17):62–67, 1990.
- [50] Ling Li, Yuwen Zhang, Hongbin Ma, and Mo Yang. An investigation of molecular layering at the liquid-solid interface in nanofluids by molecular dynamics simulation. *Physics Letters A*, 372(25):4541–4544, 2008.

- [51] Ling Li, Yuwen Zhang, Hongbin Ma, and Mo Yang. Molecular dynamics simulation of effect of liquid layering around the nanoparticle on the enhanced thermal conductivity of nanofluids. *Journal of nanoparticle research*, 12(3):811–821, 2010.
- [52] Jizu Lv, Wenzheng Cui, Minli Bai, and Xiaojie Li. Molecular dynamics simulation on flow behavior of nanofluids between flat plates under shear flow condition. *Microfluidics and nanofluidics*, 10(2):475–480, 2011.
- [53] Erdogan Madenci, Atila Barut, and Michael Futch. Peridynamic differential operator and its applications. *Computer Methods in Applied Mechanics and Engineering*, 304:408–451, 2016.
- [54] Erdogan Madenci and Selda Oterkus. Ordinary state-based peridynamics for plastic deformation according to von mises yield criteria with isotropic hardening. *Journal of the Mechanics and Physics of Solids*, 86:192–219, 2016.
- [55] Hidetoshi Masuda, Akira Ebata, Kazumari Teramae, Nobuo Hishinuma, and Y Ebata. Alteration of thermal conductivity and viscosity of liquid by dispersing ultra-fine particles (dispersion of γ -al₂o₃, sio₂ and tio₂ ultra-fine particles). 1993.
- [56] James Clerk Maxwell. *A treatise on electricity and magnetism*, volume 1. Clarendon press, 1881.

- [57] Ralf Metzler and Joseph Klafter. The random walk’s guide to anomalous diffusion: a fractional dynamics approach. *Physics reports*, 339(1):1–77, 2000.
- [58] Nicolas Moës, John Dolbow, and Ted Belytschko. A finite element method for crack growth without remeshing. *International journal for numerical methods in engineering*, 46(1):131–150, 1999.
- [59] SMS Murshed, KC Leong, and C Yang. Enhanced thermal conductivity of tio2—water based nanofluids. *International Journal of thermal sciences*, 44(4):367–373, 2005.
- [60] Cong Tien Nguyen, Selda Oterkus, Erkan Oterkus, Islam Amin, Murat Ozdemir, Abdel-Hameed El-Aassar, and Hosam Shawky. Modelling of eulerian incompressible fluid flows by using peridynamic differential operator. *Ocean Engineering*, 239:109815, 2021.
- [61] Selda Oterkus, Erdogan Madenci, and Erkan Oterkus. Fully coupled poroelastic peridynamic formulation for fluid-filled fractures. *Engineering geology*, 225:19–28, 2017.
- [62] A Ott, JP Bouchaud, D Langevin, and W Urbach. Anomalous diffusion in “living polymers”: A genuine levy flight? *Physical review letters*, 65(17):2201, 1990.
- [63] Hisanao Ouchi, Amit Katiyar, Jason York, John T Foster, and Mukul M Sharma. A fully coupled porous flow and geomechanics model for fluid

- driven cracks: a peridynamics approach. *Computational Mechanics*, 55(3):561–576, 2015.
- [64] James O’Grady and John Foster. A meshfree method for bending and failure in non-ordinary peridynamic shells. *Computational Mechanics*, 57(6):921–929, 2016.
- [65] C-W Park and GM Homsy. Two-phase displacement in hele shaw cells: theory. *Journal of Fluid Mechanics*, 139:291–308, 1984.
- [66] Lincoln Paterson. Radial fingering in a hele shaw cell. *Journal of Fluid Mechanics*, 113:513–529, 1981.
- [67] Gary A Pope et al. The application of fractional flow theory to enhanced oil recovery. *Society of Petroleum Engineers Journal*, 20(03):191–205, 1980.
- [68] Ludwig Prandtl. 7. bericht über untersuchungen zur ausgebildeten turbulenz. *ZAMM-Journal of Applied Mathematics and Mechanics/Zeitschrift für Angewandte Mathematik und Mechanik*, 5(2):136–139, 1925.
- [69] Rezwanur Rahman, John T Foster, and Anwarul Haque. A multiscale modeling scheme based on peridynamic theory. *International Journal for Multiscale Computational Engineering*, 12(3), 2014.
- [70] DA Reinelt. Interface conditions for two-phase displacement in hele-shaw cells. *Journal of Fluid Mechanics*, 183:219–234, 1987.

- [71] Clara Mabel Rice et al. Dictionary of geological terms. 1940.
- [72] Lewis Fry Richardson. Atmospheric diffusion shown on a distance-neighbour graph. *Proceedings of the Royal Society of London. Series A, Containing Papers of a Mathematical and Physical Character*, 110(756):709–737, 1926.
- [73] D Rittel. Experimental investigation of transient thermoelastic effects in dynamic fracture. *International Journal of Solids and Structures*, 35(22):2959–2973, 1998.
- [74] Nickolai M Rubtsov, Victor I Chernysh, Georgii I Tsvetkov, and Kirill Ya Troshin. Interaction of the combustion front of methane-air mixture at low pressures with obstacles of cylindrical shape. *FirePhysChem*, 1(3):174–178, 2021.
- [75] Philip Geoffrey Saffman and Geoffrey Taylor. The penetration of a fluid into a porous medium or hele-shaw cell containing a more viscous liquid. In *Proceedings of the Royal Society of London A: Mathematical, Physical and Engineering Sciences*, volume 245, pages 312–329. The Royal Society, 1958.
- [76] Suranjan Sarkar and R Panneer Selvam. Molecular dynamics simulation of effective thermal conductivity and study of enhanced thermal transport mechanism in nanofluids. *Journal of applied physics*, 102(7):074302, 2007.

- [77] Guglielmo Scovazzi, Hao Huang, S Scott Collis, and Jichao Yin. A fully-coupled upwind discontinuous galerkin method for incompressible porous media flows: High-order computations of viscous fingering instabilities in complex geometry. *Journal of Computational Physics*, 252:86–108, 2013.
- [78] Pablo Seleson. Improved one-point quadrature algorithms for two-dimensional peridynamic models based on analytical calculations. *Computer Methods in Applied Mechanics and Engineering*, 282:184–217, 2014.
- [79] Pablo Seleson and David J Littlewood. Convergence studies in meshfree peridynamic simulations. *Computers & Mathematics with Applications*, 71(11):2432–2448, 2016.
- [80] Pablo Seleson and Michael Parks. On the role of the influence function in the peridynamic theory. *International Journal of Multiscale Computational Engineering*, 9(6):689–706, 2011.
- [81] Pablo Seleson, Michael L Parks, Max Gunzburger, and Richard B Lehoucq. Peridynamics as an upscaling of molecular dynamics. *Multiscale Modeling & Simulation*, 8(1):204–227, 2009.
- [82] Mihir Sen and Eduardo Ramos. A spatially non-local model for flow in porous media. *Transport in porous media*, 92(1):29–39, 2012.
- [83] John Shadid, Scott Hutchinson, and Ray Tuminaro. *AztecOO Project Webpage*, 2022 (accessed Jan 15, 2022).

- [84] SA Silling and RB Lehoucq. Peridynamic theory of solid mechanics. *Advances in Applied Mechanics*, 44(1):73–166, 2010.
- [85] S.A. Silling, M. Zimmermann, and R. Abeyaratne. Deformation of a peridynamic bar. *Journal of Elasticity*, 73(1):173–190, 2003.
- [86] Stewart A Silling. Reformulation of elasticity theory for discontinuities and long-range forces. *Journal of the Mechanics and Physics of Solids*, 48(1):175–209, 2000.
- [87] Stewart A Silling. Origin and effect of nonlocality in a composite. *Journal of Mechanics of Materials and Structures*, 9(2):245–258, 2014.
- [88] Stewart A Silling and Ebrahim Askari. A meshfree method based on the peridynamic model of solid mechanics. *Computers & structures*, 83(17-18):1526–1535, 2005.
- [89] Stewart A Silling, M Epton, O Weckner, Ji Xu, and E23481501120 Askari. Peridynamic states and constitutive modeling. *Journal of Elasticity*, 88(2):151–184, 2007.
- [90] Stewart A Silling, Markus Zimmermann, and Rohan Abeyaratne. Deformation of a peridynamic bar. *Journal of Elasticity*, 73(1-3):173–190, 2003.
- [91] Brajeesh K Singh and Jalel Azaiez. Numerical simulation of viscous fingering of shear-thinning fluids. *The Canadian Journal of Chemical Engineering*, 79(6):961–967, 2001.

- [92] Joseph Smagorinsky, Syukuro Manabe, and J Leith Holloway Jr. Numerical results from a nine-level general circulation model of the atmosphere. *Monthly weather review*, 93(12):727–768, 1965.
- [93] KH Solangi, SN Kazi, MR Luhur, A Badarudin, A Amiri, Rad Sadri, MNM Zubir, Samira Gharehkhani, and KH Teng. A comprehensive review of thermo-physical properties and convective heat transfer to nanofluids. *Energy*, 89:1065–1086, 2015.
- [94] Fangying Song and George Em Karniadakis. A universal fractional model of wall-turbulence. *arXiv preprint arXiv:1808.10276*, 2018.
- [95] Jeong-Hoon Song and Ted Belytschko. Cracking node method for dynamic fracture with finite elements. *International Journal for Numerical Methods in Engineering*, 77(3):360–385, 2009.
- [96] Vincenz Strouhal. *Über eine besondere Art der Tonerregung*. Stahel, 1878.
- [97] Kuo-Liang Teng, Pai-Yi Hsiao, Shih-Wei Hung, Ching-Chang Chieng, Ming-Shen Liu, and Ming-Chang Lu. Enhanced thermal conductivity of nanofluids diagnosis by molecular dynamics simulations. *Journal of nanoscience and nanotechnology*, 8(7):3710–3718, 2008.
- [98] A. P. Thompson, H. M. Aktulga, R. Berger, D. S. Bolintineanu, W. M. Brown, P. S. Crozier, P. J. in 't Veld, A. Kohlmeyer, S. G. Moore, T. D. Nguyen, R. Shan, M. J. Stevens, J. Tranchida, C. Trott, and

- S. J. Plimpton. LAMMPS - a flexible simulation tool for particle-based materials modeling at the atomic, meso, and continuum scales. *Comp. Phys. Comm.*, 271:108171, 2022.
- [99] Hao Tian, Lili Ju, and Qiang Du. Nonlocal convection–diffusion problems and finite element approximations. *Computer Methods in Applied Mechanics and Engineering*, 289:60–78, 2015.
- [100] Elena V Timofeeva, Alexei N Gavrilov, James M McCloskey, Yuriy V Tolmachev, Samuel Sprunt, Lena M Lopatina, and Jonathan V Selinger. Thermal conductivity and particle agglomeration in alumina nanofluids: experiment and theory. *Physical Review E*, 76(6):061203, 2007.
- [101] Qi Tong and Shaofan Li. Multiscale coupling of molecular dynamics and peridynamics. *Journal of the Mechanics and Physics of Solids*, 95:169–187, 2016.
- [102] Albert Turon, Carlos G Davila, Pedro Ponces Camanho, and Josep Costa. An engineering solution for mesh size effects in the simulation of delamination using cohesive zone models. *Engineering fracture mechanics*, 74(10):1665–1682, 2007.
- [103] GM Viswanathan, EP Raposo, and MGE Da Luz. Lévy flights and superdiffusion in the context of biological encounters and random searches. *Physics of Life Reviews*, 5(3):133–150, 2008.

- [104] Th Von Karman. Über den mechanismus des widerstandes, den ein bewegter körper in einer flüssigkeit erfährt. *Nachrichten von der Gesellschaft der Wissenschaften zu Göttingen, Mathematisch-Physikalische Klasse*, 1911:509–517, 1911.
- [105] J Wang and M Dong. Optimum effective viscosity of polymer solution for improving heavy oil recovery. *Journal of Petroleum Science and Engineering*, 67(3):155–158, 2009.
- [106] Xiang-Qi Wang and Arun S Mujumdar. Heat transfer characteristics of nanofluids: a review. *International journal of thermal sciences*, 46(1):1–19, 2007.
- [107] Xinwei Wang, Xianfan Xu, and Stephen US Choi. Thermal conductivity of nanoparticle-fluid mixture. *Journal of thermophysics and heat transfer*, 13(4):474–480, 1999.
- [108] Xipeng Wang, Simón Ramírez-Hinestrosa, Jure Dobnikar, and Daan Frenkel. The lennard-jones potential: when (not) to use it. *Physical Chemistry Chemical Physics*, 22(19):10624–10633, 2020.
- [109] O. Weckner and S.A. Silling. Determination of nonlocal constitutive equations phonon dispersion relations. *International Journal of Multi-scale Computational Engineering*, 9(6):623–634, 2011.
- [110] Matthias Weiss, Hitoshi Hashimoto, and Tommy Nilsson. Anomalous

- protein diffusion in living cells as seen by fluorescence correlation spectroscopy. *Biophysical journal*, 84(6):4043–4052, 2003.
- [111] SDR Wilson. A note on the measurement of dynamic contact angles. *Journal of Colloid and Interface Science*, 51(3):532–534, 1975.
- [112] Xiao Xu, Marta D’Elia, and John T Foster. A machine-learning framework for peridynamic material models with physical constraints. *Computer Methods in Applied Mechanics and Engineering*, 386:114062, 2021.
- [113] Xiao Xu and John T Foster. Deriving peridynamic influence functions for one-dimensional elastic materials with periodic microstructure. *arXiv preprint arXiv:2003.05520*, 2020.
- [114] Huaiqian You, Yue Yu, Nathaniel Trask, Mamikon Gulian, and Marta D’Elia. Data-driven learning of robust nonlocal physics from high-fidelity synthetic data. *arXiv preprint arXiv:2005.10076*, 2020.
- [115] W Yu and SUS Choi. The role of interfacial layers in the enhanced thermal conductivity of nanofluids: a renovated maxwell model. *Journal of nanoparticle research*, 5(1-2):167–171, 2003.